Title
Thermodynamic measurements of applied magnetic materials

Permalink
https://escholarship.org/uc/item/2t48262z

Author
Cooke, David William

Publication Date
2010

Peer reviewed|Thesis/dissertation

Thermodynamic Measurements of Applied Magnetic Materials

by

David William Cooke

A dissertation submitted in partial satisfaction of the

requirements for the degree of

Doctor of Philosophy

in

Physics

in the

Graduate Division

of the

University of California, Berkeley

Committee in charge:

Professor Frances Hellman, Chair
Professor Ramamoorthy Ramesh
Professor Yuri Suzuki

Fall 2010

Thermodynamic Measurements of Applied Magnetic Materials

Copyright 2010

by

David William Cooke

Abstract

Thermodynamic Measurements of Applied Magnetic Materials

by

David William Cooke

Doctor of Philosophy in Physics

University of California, Berkeley

Professor Frances Hellman, Chair

The specific heat of a material offers a host of information about the energetics of the system, from the phonons and electrons to phase changes in the material and two-state systems. In order to measure the specific heat of small samples such as quenched high pressure materials or thin films, one must turn to microcalorimetry. This thesis discusses the application of microcalorimetry to small magnetic samples and the underlying physics illuminated by the technique.

The thesis first describes the measurement of the spinel and olivine phases of Fe_2SiO_4 and the technical development necessary to measure a metastable small (10-100μg) sample, obtaining the first direct measurement of the entropy difference between the two phases.

Focusing next on the canonical giant magneto-resistive system of Fe/Cr multi-layers, first is discussed the contributions of disorder to the electrons and phonons in the system where it is determined that disorder and strain plays a dominant role in the electronic density of states for thin films of chromium and not the antiferromagnetic state of the film. Next it is determined that while sputtered Fe/Cr multilayers do exhibit an interfacial enhancement in the density of states due to interfacial alloying, the spin-dependent scattering is more dependent upon a well-defined quantum well structure.

Finally, described herein is the development of a new calorimeter based on the ion beam-assisted deposition (IBAD) of MgO in order to measure the specific heat of epitaxial thin films. After measuring the lattice parameters of the IBAD MgO through synchrotron X-ray diffraction (XRD) and proving through XRD that thin films could successfully be grown epitaxially on the device, it was used to measure the specific heat of Fe-Rh alloys with ferromagnetic and antiferromagnetic ground states. Fe-Rh alloys have been suggested for application to thermally assisted magnetic recording, but there is much debate in the literature about the theoretical origin of the AF>FM transition. By taking the difference in specific heat of the two alloys, a predicted Schottky anomaly is observed and discussed in the context of two thermal fluctuation models. Our photoemission and specific heat data show that the origin of the transition is not adequately explained by the difference in electronic densities of states.

To my dad, who taught me to set goals,
My mom, who gave me the strength to meet them,
And my friends, who supported me when I didn't.

You don't use science to show that you're right -
you use science to become right.
– xkcd

Contents

List of Figures

List of Tables

Acknowledgments

This work is the sum total of many years of my life, but without the teachings, patience, and support of the many people helping me through that it all, this book'd be empty.

I'd first like to thank my advisor, Frances Hellman, for providing me with the opportunity to do scientific research at a high level and the freedom to find my way at my own pace.

Many people in the Hellman Lab have helped me along the way, but I'd like to thank a few in particular. Daniel Queen taught me everything I know (and some that I've forgotten) about microfabrication and was always at the ready to act as a sounding board for my many half-baked ideas. Erik Helgren showed me the virtues of running an experiment by the seat of your pants and was always ready for a "teaching moment," no matter how full his own plate was. Zoe Boekelheide taught me everything anyone could possibly want to know about chromium. Julie Karel gave me a daily tutorial in materials science. Chloe Baldasseroni taught me patience in teaching. Cathy Bordel was always on hand to be my unofficial co-advisor. And Mark Wong was the best roommate, football fan, political junkie, and all-around distraction I needed to get me through the lab experience.

And last, but not least, I'd like to thank everyone who helped me outside the scientific realm. My family propelled me in the end with gentle nudging, but without their loving support for many, many years prior, this endeavor would have never been possible. My UCSD friends made for an amazing graduate school experience outside the classroom, but David, Maggie, and Novi in particular taught me you can survive on music, beer, and Mexican food if you've got great company. And my Harvey Mudd friends get the distinct pleasure of not hearing me say "soon" anymore - thanks for not letting that go.

Chapter 2 is largely a reprint of "Thermodynamic measurement of submilligram bulk samples using a membrane-based 'calorimeter on a chip'," Cooke, David W., Michel, K.J., and Hellman, F. *Rev. Sci.Instr.* **79**, 053902 (2008).

Chapter 3 is largely a reprint of "The role of the spin-density wave and disorder in the density of states of sputtered Cr films," Cooke, David W., Boekelheide, Z., Queen, D.R., and Hellman, F. *J. Appl. Phys.* **105**, 07C314 (2009).

Chapter 4 is a preprint of "Interfacial contribution to the electronic and phononic density of states in Fe/Cr multilayer films," Cooke, David W., Queen, D.R., and Hellman, F. *J. Mag. Mag. Mater.* (submitted, December 2010).

Chapter 5 is a preprint of "Calorimetry of epitaxial thin films," Cooke, David W., Groves, J.R., Clemens, B.M., Hellman, F., Moyerman, S., and Fullerton, E.E. *Rev. Sci. Instr.* (submitted, December 2010).

Vita

August 9, 1980	Born, Grand Rapids, Michigan
2002	B.S. in Physics, Harvey Mudd College, Claremont, CA
2002-2003	Teaching Assistant, University of California, San Diego
2003-2004	Research Assistant, University of California, San Diego
2004	M.S. in Physics, University of California, San Diego
2004-2010	Research Assistant, University of California, Berkeley
2010	Ph.D. in Physics, University of California, Berkeley

Publications

"Calorimetry of epitaxial thin films," **Cooke, David W.**, Groves, J.R., Clemens, B.M., Hellman, F., Moyerman, S., and Fullerton, E.E. *Review of Scientific Instruments* (submitted).

"Interfacial contribution to the electronic and phononic density of states in Fe/Cr multilayer films," **Cooke, David W.**, Queen, D.R., and Hellman, F. *Journal of Magnetism and Magnetic Materials* (submitted).

"Electron-mediated ferromagnetism in CoO/ZnO multilayer," Lee, H.-J., Karel, J., **Cooke, David W.**, and Hellman, F. *Nanoletters* (submitted).

"Resonant impurity scattering and electron-phonon scattering in the electrical resistivity of Cr thin films," Boekelheide, Z., **Cooke, David W.**, Helgren, E., and Hellman, F. *Physical Review B* **80**, 134426 (2009).

"The role of the spin-density wave and disorder in the density of states of sputtered Cr films," **Cooke, David W.**, Boekelheide, Z., Queen, D.R., and Hellman, F. *Journal of Applied Physics* **105**, 07C314 (2009).

"Thermodynamic measurement of submilligram bulk samples using a membrane-based 'calorimeter on a chip'," **Cooke, David W.**, Michel, K.J., and Hellman, F. *Review of Scientific Instruments* **79**, 053902 (2008).

"Application of calorimetry on a chip to high-pressure materials," Navrotsky, A., Dorogova, M., Hellman, F., **Cooke, David W.**, Zink, B.L., Lesher, C.E., Boerio-Goates, J., Woodfield., B.F., and Lang, B. *Proceedings of the National Academy of Sciences* **104**, 9187-9191 (2007).

Chapter 1

Introduction

The discovery of giant magnetoresistance (GMR) in the late 1980s by Fert and Grunberg set off an explosion of magnetic research. Their Nobel Prize-winning work helped to increase hard drive storage capacity by an order of magnitude virtually overnight. As we've become more and more reliant upon gigabytes of data, our information infrastructure has not been concerned just with where to store the information but also how to access it readily, whether that means solid state hard drives in your cellular phone or the development of new technologies such as spintronics in order to drive power consumption down and scale computing beyond Moore's Law. With this flurry of activity and the push to the micro- and nano-scale, fundamental questions in magnetism are still at the forefront of research activity today. Thermodynamic measurements such as heat capacity can be used to address many of the fundamental material properties at work in these novel applied magnetic materials.

The specific heat of a material offers a wealth of information - from the specific heat of a transition, one can examine the energetic and entropic differences in the two phases, shedding light on the underlying driving mechanism, and from the low-temperature heat capacity one can obtain information about both the vibrational modes of the material (phonons) and the density of states of the electrons, both of which factor into phenomena such as GMR, multiferroism, and spintronics. In metals, which is the focus of this thesis, the low temperature specific heat $C = \gamma T$ (electrons)$+\beta T^3$ (phonons). Here, γ is the Sommerfeld coefficient which is derived from the free electron gas; $\gamma = \frac{1}{3}\pi^2 k_B^2 N(\epsilon_F)(1+\lambda)$, where N is the density of states of the electron and λ accounts for any change in the effective mass of the electrons, be it from electron-phonon coupling or electron-electron interactions. The β term represents the low-temperature approximation to the Debye model of the phonon specific heat, $C_{Debye} = 9nR(\frac{T}{\theta_D})^3 \int_0^{\theta_D/T} dx \frac{x^4 e^x}{(e^x-1)^2}$. The Debye model itself is an approximation where we assume a frequency-independent sound velocity. In magnetic materials, there is an additional contribution to the heat capacity at low temperatures from magnons - in the case of ferromagnets (antiferromagnets), it is $\alpha T^{3/2}$ (αT^3). One may also observe Schottky anomalies from closely spaced energy levels, most common in paramagnetic salts or hyperfine splitting in rare earth ferromagnets.

In order to study the specific heat of the micro- and nano-structured materials of technological import, one must push beyond traditional bulk calorimetric techniques because the contribution of the background addenda in these experimental apparati far

exceeds the heat capacity of the samples themselves. In 1994, our group published the first work on a microcalorimeter centered around an amorphous silicon nitride membrane and fabricated using standard MEMS processing[30]. It has since been used to study a range of materials from cuprate superconductors and half-metallic manganites to fullerene thin films and rare-earth-doped silicon. This thesis will be focused on using these microcalorimeters to study novel magnetic materials and the technical development of the calorimetric technique necessary to do so.

In Chapter 2, we examine a method of using our microcalorimeters to measure the heat capacity of small crystalline samples ($\approx 10 - 100\mu$g). We use a new technique of attaching the samples with silver conductive paint and prove its reproducibility. Previous 2-D heat flow simulation of our devices was used to characterize the systematic error of our technique on thin films[98], and in Chapter 2 we build on this work by examining the systematic errors in measuring the specific heat of small samples attached to the thin film calorimeters. We also characterize the regimes where our small-ΔT relaxation technique is applicable and use our devices to measure the specific heat of three antiferromagnets - CoO, α-Fe$_2$SiO$_4$, and γ-Fe$_2$SiO$_4$. The spinel (γ) phase of Fe$_2$SiO$_4$ is of particular interest to the geophysics community and can only be generated in small quantities due to its metastability. We calculate the enthalpic and entropic differences between the olivine (α) and spinel phases and find good agreement with indirect analysis in the literature based on $P - T$ phase equilibria.

After examining new limits of our technique, we will discuss in the remaining chapters applications of our technique to applied magnetic materials. Chapters 3 and 4 focus on the Fe/Cr multilayer system mentioned earlier. Models of giant magnetoresistance rely on scattering at the interface of the multilayer through quantum well interference. Here, the densities of states of the electrons are purported in some theories to play a key role. Chromium, in contrast to copper in the Co/Cu GMR system, is an antiferromagnet where the antiferromagnetism results of a nesting of two portions of the Fermi surface with a spanning vector $Q = (1 \pm \delta \; 0 \; 0)$. This nesting and the resulting spin density wave changes the density of states in the multilayer structure. In well-ordered Fe/Cr layers, this spanning vector is believed to result in short-range oscillations in addition to the long-range oscillations primarily responsible for the GMR behavior. However, it has already been shown how chromium's antiferromagnetism is affected by the multilayer structure, resulting in commensurate antiferromagnetism instead of the incommensurate behavior seen in bulk[40, 92]. In Chapter 3, we therefore focus on chromium itself to understand the effects of the thin film structure on its density of states. By sputtering a series of films under different growth conditions, we are able to observe a range of antiferromagnetic behavior. However, these growth conditions also result in additional disorder in the film. We will discuss these two contributions and how they affect the electronic density of states in the material, showing that disorder broadening plays a much stronger role in the density of states than details of the antiferromagnetic state. Armed with this knowledge, in Chapter 4 we examine the electronic density of states of the Fe/Cr multilayer system itself. As mentioned above, the electronic DOS is believed to have a relationship to the GMR behavior of the system. Earlier work showed an enhanced Sommerfeld coefficient γ for the multilayer film with maximum GMR[97]. In Chapter 4, we show measurements for a series of Fe/Cr

multilayers with varying Cr thickness (and therefore varying GMR behaviors) to assess the relationship of GMR in this system to the electronic DOS. We show that we do have an enhanced interfacial contribution to the DOS; however, it does not correlate to the GMR behavior of the system. In fact, we find that the film with the lowest DOS (enhanced above the average Fe and Cr values by $\sim 18\%$)actually shows the highest GMR behavior, 105% MR at 4K.

In Chapters 5 and 6, we focus on the measurement of the specific heat of epitaxial thin films. As mentioned earlier, our devices are fabricated around an amorphous silicon nitride membrane to reduce the thermal link of our thin film samples to the silicon frame. However, our samples must either be bulk samples attached to the membrane as in Chapter 2 or deposited directly on the amorphous membrane substrate as in Chapters 3 and 4, resulting in polycrystalline or amorphous samples. One of the key advantages of thin film growth is the ability to use a substrate template to stabilize a non-equilibrium phase, and in certain systems of technological import such as FeRh/FePt, a highly ordered material is crucial. Therefore, in Chapter 5, we focus on the use of ion beam-assisted deposition (IBAD) to create a biaxially-oriented MgO template onto our devices. We present synchrotron x-ray diffraction data characterizing the lattice parameters of the template itself and x-ray reflectivity measurements showing epitaxial growth onto this template. We then measure the specific heat of a device with this IBAD MgO layer and compare it to bulk MgO, also showing that it has an incredibly small contribution to the total device addenda ($\sim 6.5\%$), thus having no effect on the accuracy of our measurement technique. Finally, we measure the specific heat of an $Fe_{.49}Rh_{.51}$ alloy film and show that it compares similarly to measurements of bulk samples measured at low ($< 4.2K$) and moderate (100-500K) temperatures.

Iron-rhodium alloys of nearly equiatomic composition undergo an antiferromagnetic to ferromagnetic (AF>FM) transition. Because this transition takes place at just above room temperature, this material has technological applications relevant to magnetic recording. For example, in the FePt/FeRh bilayer system proposed for thermal (heat)-assisted magnetic recording (TAMR or HAMR), the AF FeRh phase can be used to stabilize the magnetically hard FePt layer. By heating the system above $T_{AF>FM}$, the additional FM FeRh moment will couple to the high-anistropy FePt material, helping in magnetic writing. Upon cooling, the FeRh layer returns to the AFM state so the bit is less easily reversed. Tuning the Rh composition can be used to alter the $T_{AF>FM}$ of the transition, and Fe-rich alloys can suppress the transition entirely, leading to a ferromagnetic ground state. There are many theories as to the driving interaction that causes the AF>FM transition. It was proposed that a difference in electronic entropy between the AFM and FM states accounts for the transition, and low temperature heat capacity data initially agreed with this claim[112]. The problems with this model are twofold - first, it suggests a temperature-independent DOS, which contradicts work on traditional antiferromagnets like chromium; second, additional data on FeRh alloys doped with Ir showed inconsistencies in the DOS values for FM and AFM alloys[38]. Gruner, et al. suggest as an alternative theory that it is temperature-dependent magnetic fluctuations that drive the system[50]. The results of their DFT and Monte Carlo simulations are that the FM FeRh alloy should exhibit a Schottky-like two-state anomaly at moderate temperatures (≈ 200 K) due to the competing free energies of a magnetic and non-magnetic Rh atom. Because the J_{Fe-Rh} interaction

cancels out at the Rh site in the AFM state, it does not exhibit such an anomaly. Another fluctuation model by Gu and Antropov[51] suggests that the Fe and Rh are more strongly coupled and that the transition is driven predominantly by the free energy gain of magnon excitations in the FM phase; this model suggests a different contribution to the specific heat difference between the FM and AFM phases with a peak difference at approximately 300K. By measuring alloys with nearly equiatomic compositions but differing ground states $(T_{AF>FM}(\text{Fe}_{.49}\text{Rh}_{.51}) = 350\text{K}$, while $\text{Fe}_{.52}\text{Rh}_{.48}$ is FM up to high temperatures), we can observe the heat capacity difference between the two phases. Our data shows a Schottky-like anomaly in the ferromagnetic phase, as predicted; however, the magnitude of the difference in the two Rh states ($1.5\pm0.2\text{mRyd}$) leads to a peak at a much lower temperature than predicted in either model ($\sim 100\text{K}$ compared to 200K or 300K in the Gruner et al. and Gu and Antropov models, respectively), though the error bars of our dataset are of the order of 50% of the measured anomaly, so it is difficult to say anything conclusive regarding the two fluctuation models. However, this data and complementary photoemission measurements above and below the transition do show that the transition is *not* driven by the simple ground state electronic entropy difference suggested by Tu et al.

Overall, we find that calorimetry offers insight into the fundamental physics behind novel magnetic systems. As magnetic thin films continue to produce a wealth of opportunities in technological applications, microcalorimetry will continue to provide a platform for understanding the basic principles driving these new phenomena, whether it is through entropy and/or phase changes or electronic or phononic densities of state. Furthermore, the development of the IBAD MgO microcalorimeter allows a host of new metastable materials to be studied.

Chapter 2

Small Sample Calorimetry

2.1 Introduction

Thermodynamic measurements are an important tool in understanding the fundamental properties of novel systems, providing direct and quantifiable insight into densities of states and phase transitions. In many cases, these new materials may only be synthesized in thin film or small bulk form, scales at which traditional bulk calorimetric techniques are not applicable[71, 107, 87]. Of primary focus in this article is the measurement of the specific heat of small samples (sub-mg). These novel systems are numerous, including but not limited to metastable minerals of geological interest[88], nanocrystalline semiconductors[113], and granular[61] and molecular[39] ferromagnets. Despite the increasing interest in these materials, the last major review of small-sample calorimetry was tackled by Stewart almost 25 years ago[107]. Traditional bulk sample calorimeters are limited either to rather large samples ($\gtrsim$1mg) or to low temperatures ($\lesssim$50K)[31]. Modern differential-scanning and AC calorimetry work has yielded results on .1-100 μg-sized samples[57, 69, 76, 82, 101]. Because these are relative measurements, phase transitions can be resolved quite well using these methods; however, the absolute accuracy of the resultant specific heat diminishes significantly ($\sim$ 15% at best) for these techniques due to limitations of the noise floor and the size of the addenda. In the present work, we take advantage of the low background heat capacity of membrane-based calorimeters and investigate the feasibility and accuracy limits of using the relaxation method to measure the heat capacity of small bulk samples from $\lesssim 2 - 300$K. This chapter describes the capabilities of this technique, starting first with a brief explanation of the method, a look at some heat flow simulation work, and finally a presentation of experimental results. From this analysis, we will quantify the region of validity of this calorimetric technique and identify potential systematic errors in the measurement.

Thermal relaxation calorimetry is a widely used technique for measuring heat capacity of small samples. In Bachmann's pioneering design, the sample is thermally and physically bound to a silicon bolometer consisting of heater, thermometer, and sample platform. Thin gold wires form a weak thermal link between this bolometer and a frame which is strongly coupled to a sample block held at temperature T_0[9]. This is considered a semi-adiabatic calorimeter because it is impossible to completely thermally isolate the sample due to the need for electrical leads and bolometer support structure (the gold wires).

This causes the thermal conductance between the bolometer and the environment to be less but not infinitely less than that between the sample and the bolometer.

This basic design has been modified and used by groups all over the world. A similar design is currently available in commercial form for Quantum Design's PPMS system. However, there are limitations to this design given the macroscopic size of the bolometer and leads. The background contribution (commonly called the addenda) of the leads, heater, and sample platform, or stage, is quite large; Quantum Design's PPMS system quotes a lower limit on sample size of 10mg due to this large background signal. Additionally, a common material used to mount samples to these stages is thermal grease such as Apiezon® N. However, the glass transition in Apiezon® N grease leads to a large and irreproducible temperature dependency in the background, or addenda, heat capacity[1, 67, 70, 104]. The limited thermal conductance through the grease also causes the time constant of the sample to the stage to become important, resulting in an internal time constant problem; this variant of the τ_2 problem is known as a "lumped τ_2" model. A different variation on the τ_2 problem occurs with highly insulating samples. As the time constant internal to the sample itself becomes comparable to that between the sample and the frame, this results in what is known as the "distributed τ_2" effect[9]. Both of these lower boundaries are set by the thermal conductance between the sample stage and the frame, so decreasing this results in the ability to measure more thermally insulating samples.

Silicon-based microfabrication techniques have allowed the production of a much smaller calorimeter centered around a low-stress silicon nitride (Si-N) membrane[30]. To create these microcalorimeters, we start from a (100)-oriented double-polished Si wafer. On this, we deposit via chemical vapor deposition (CVD) a high-temperature "wet" oxide (steam + O_2), yielding a smooth buffer layer of 3000 Å; this oxide layer reduces capacitive links between thermometers and heaters. A low-stress (off-stoichiometry) silicon nitride layer of appropriate thickness is then deposited via low-pressure CVD (LPCVD) to provide the sample platform and act as our weakly thermally conductive link. For larger samples ($\gtrsim$ 100 μg) we deposit a 1.5 μm thick Si-N layer which increases the addenda but yields stronger structural integrity for the large samples[61], while for thin films and small bulk samples we use an 1800 Å thick Si-N layer. We then thermally evaporate and pattern Pt for electrical leads as well as thermometers and the stage heater. Furthermore, on calorimeters to be used for large bulk sample measurements we deposit conductive Pt "wings" to reduce the otherwise long time constants due to the high heat capacity of these large samples. The Si is then etched away in the central area, leaving a Si frame around the outside and a thin Si-N membrane with heaters and thermometers in the center. The membrane provides a low thermal conductivity but relatively strong structural support for samples. The next step in processing of our devices is the sputtering of amorphous NbSi alloy thermometers (a-Nb$_x$Si$_{1-x}$, $x \approx 0.1$) for use as sensitive low-temperature thermometers. We then thermally evaporate a Cu conduction layer on the backside of the membrane in the central sample area . A more detailed description of most of this processing technique may be found in earlier work[30].

The resulting calorimeter is pictured below (Figure 2.1) and consists of a silicon frame supporting the Si-N membrane where, in the center, reside a heater, thermometers, a thermal conduction layer, and the sample itself. Pictured as well are platinum "wings",
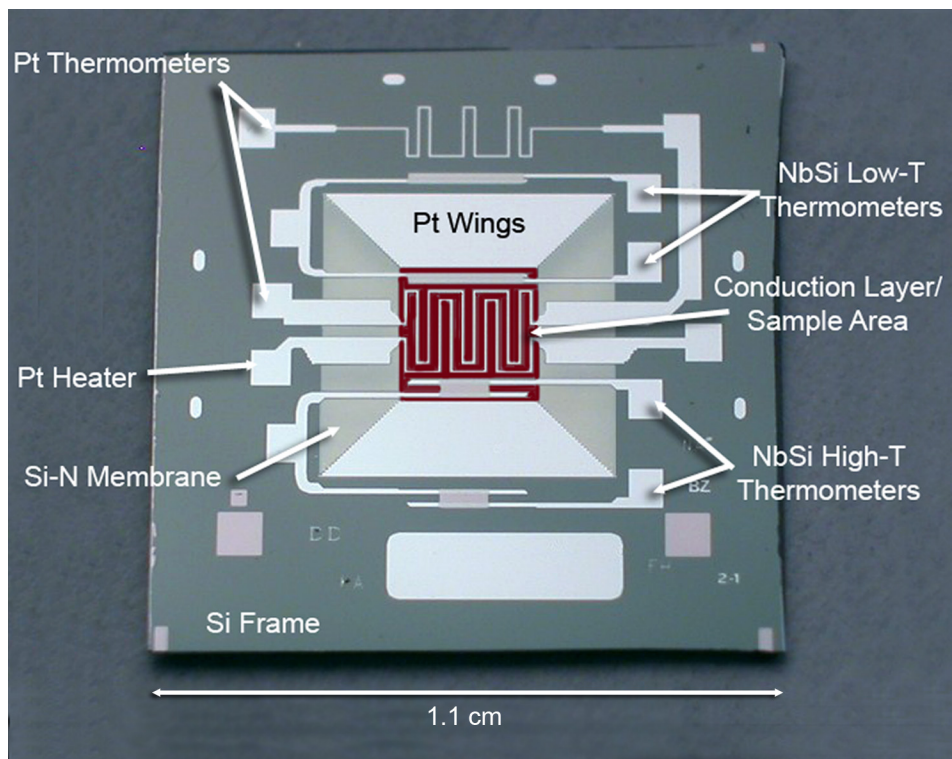
Figure 2.1: Photograph of the microcalorimeter. Arrows point to the contact pads for the heater and each pair of thermometers (one each on the frame and sample area).

whose function will be described in further detail later in this chapter (Section 2.2.1). The thermal conduction layer provides a uniform, isothermal region to ensure precise measurement of the sample's temperature and clearly set the boundaries of the sample space and external sink. The Si-N membrane provides a weak thermal link to the Si frame, which in turn is tightly coupled to a copper block at T_0. This thin film construction reduces the addenda contribution of the conduction layer, membrane, and thermometers to ∼1 nJ/K at 2K and ∼8 μJ/K at RT for our standard "thin" membrane devices or roughly 7 times that for our "thick" membrane devices, many orders of magnitude below that of other bulk heat capacity measurement techniques. This is crucial to measuring small (sub-mg) quantities of material.

Because our sample space is weakly linked to the frame, we employ the semi-adiabatic relaxation method of calorimetry. For this method to work, $\tau_{int} \ll \tau$, where τ_{int} refers to internal thermal time constants within the sample and between the sample and the thermometers/heaters, and τ refers to the thermal relaxation time between the sample and the frame, often called an "external" time constant. If τ_{int} is comparable to τ, this results in what is commonly referred to as a τ_2 problem, complicating and often invalidating the measurement technique.

The relaxation technique consists first of applying a constant power P to the

sample via a heater (Pt for our devices), allowing it to reach a steady state. The equilibrium temperature difference ΔT, measured by one of three thermometers in the central sample area (depending on temperature range), yields the value of the thermal conductance, $\kappa = P/\Delta T$, of our device. Once obtaining κ, we turn off the power to the system and monitor the temperature decay. In the limit $\Delta T \ll T_0$, this decay is exponential with a single time constant, τ, assuming a good thermal link between the sample and the thermometers. The total heat capacity is then defined as $C = \kappa \times \tau$. This heat capacity C includes that of the sample and addenda (membrane, thermometers, and heater). The addenda is separately measured (without sample) and subtracted to obtain the heat capacity of the sample. Further description of our methodology is available elsewhere[30].

Previous work on heat flow simulations of these membrane-based devices has established accuracy limits related to thermal conductivity of thin film samples and the conduction layer, film thickness, overall heat capacity, etc.[98] This previous work, however, focused solely on thin film samples with geometry matching that of the conduction layer. Bulk samples lack this matching symmetry and could thus lead to significantly different heat flow for four reasons — 1) their mass is concentrated at a small point on the sample area; 2) their large heat capacity (even for a sub-mg sample) leads to an excessively long τ; 3) their macroscopic out-of-plane dimension relative to the membrane necessitates the consideration of out-of-plane heat flow; and 4) an attachment method becomes necessary, unlike the thin films deposited directly onto the membrane surface. This last issue leads to a very well-defined τ_2 problem, but the first three issues and how they influence systematic errors in a membrane-based calorimeter are not known. The third issue is particularly important for samples with low thermal conductivity and leads to what is commonly called a τ_N or "distributed τ_2" problem.

In this work, we employ a numerical simulation to address the heat flow questions presented in measuring a small bulk sample with a membrane-based calorimeter. Because computing power has improved significantly since the original simulation study[98], we are able to solve this problem in the exact 2-D geometry of the microcalorimeters instead of a more idealized geometry used previously. These results show clearly defined constraints on our technique related to sample size and sample thermal conductivity. We examine, in particular, the expression of a τ_{int} effect and the consequent intrinsic systematic error in the small bulk sample measurement. Furthermore, our desire to measure over a wide temperature range (at least 2-500K) makes the commonly used grease not an option for sample attachment, and the metastable nature of some of our samples eliminates the previous use of indium[61]. We therefore examine the use of silver paint as a thermally conductive mount instead. Finally, we present experimental results of the heat capacity of a known small bulk sample measured with our membrane-based calorimeters to sum up our results.

2.2   Heat Flow Simulations

The time constant associated with vertical heat flow from one side of the membrane to the other is negligible compared to that in the lateral direction due to the 3-4 orders of magnitude difference in path length, so a two-dimensional model is generally sufficient. Using the Mathworks PDETool for MATLAB to solve the 2-D heat diffusion equation,
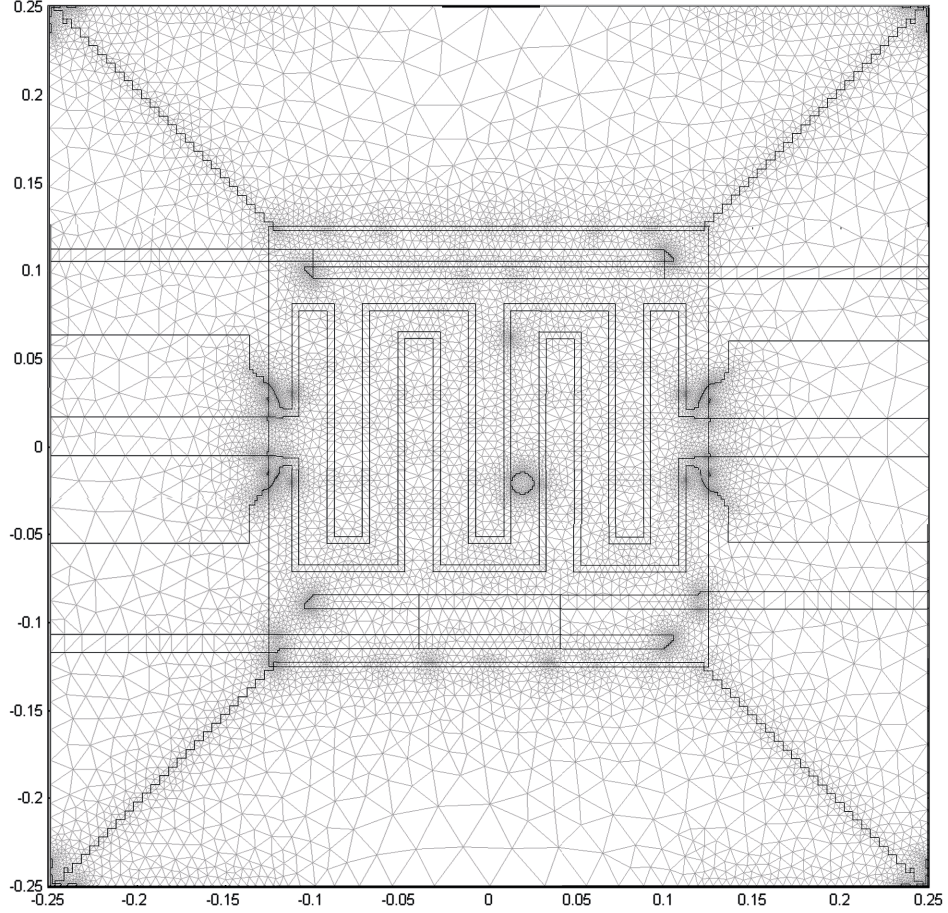
Figure 2.2: The two-dimensional finite-element mesh used in MATLAB simulation via the PDETool.

$$c_{2D}(x,y)\frac{\partial T(x,y,t)}{\partial t} - \frac{\partial}{\partial x}\left(k_{2D}(x,y)\frac{\partial T(x,y,t)}{\partial x}\right)$$

$$-\frac{\partial}{\partial y}\left(k_{2D}(x,y)\frac{\partial T(x,y,t)}{\partial y}\right) = P(x,y,t), \tag{2.1}$$

we are able to define the realms of parameter space where our devices operate most effectively and determine systematic error limits. Here $c_{2D}(x,y)$ is the heat capacity in units of J/cm^2·K at point (x,y). For example, if we examine a point in the central area of our membrane where the copper conduction layer lies, $c_{2D} = c_{Si-N} \times h_{Si-N} \times \rho_{Si-N} + c_{Cu} \times h_{Cu} \times \rho_{Si-N}$, where h is the height, or thickness, of the material layer. Similarly, $k_{2D} = k \times h$. We define T relative to the block temperature T_0.

To numerically solve the two-dimensional heat-flow equation, a triangular mesh

is generated based on the exact geometry of the device[98]. This allows for finite-element analysis, solving the heat transfer equation at each of the ∼3000 nodes. The boundary conditions define the solution at the perimeter of the membrane (the Si frame), and the solution is iteratively generated inward for each node. Based on this initial solution, the mesh can be further refined to allow for more accurate solutions throughout the surface. The mesh for the standard device with wings and sample added is shown in Figure 2.2.

Similar to the actual experimental application of our microcalorimeters, two solutions are generated during the simulation, a steady-state solution ($\partial T/\partial t = 0$) and a time-dependent solution ($P = 0$). The steady-state solution is used to determine κ, the thermal conductance of the device, and corresponds to the situation where the heater is generating a constant power but there is no net heat flow at any point on the surface. In the time-dependent solution, the power to the heater is turned off at $t = 0$, and the solution is calculated at each node as a function of time in intervals of set time. The resulting $T(t)$ is fit to a single exponential, and from this the time constant, τ, is determined. Both solutions assume the boundary condition that the temperature is fixed at the membrane edges. It is also assumed that no heat is lost to the surrounding environment (i.e. the device is in a vacuum with no radiative heat loss). These two solutions are used to calculate the simulated heat capacities and compared to the initial values for c_s and k_s input into the program.

Using the PDETool outlined above, we studied individually the effects of adding the metallic "wings" and the measurement of a small, bulk sample placed at various positions within the sample area. Of primary interest is what happens to the thermal conductance κ of our devices and/or the ΔT measured by the thermometer(s) compared to the ΔT of the sample in each of these cases, as any changes may impede our ability to accurately obtain C_P and/or take us out of the range of applicability of our semi-adiabatic technique. As the thermal conductance changes and the samples measured become larger, understanding possible deviations such as a τ_2 effect become crucial to recognizing the feasibility and limitations of our technique. Moreover, it is important to quantify these limits in the regimes proposed as well as any systematic error for this new application.

In the discussion below, as in our earlier simulation paper for thin films[98], we have used 20.3K as a nominal block temperature T_0. While all results obtained are in some sense independent of this choice of T_0, the large number of parameters in the problem (thermal conductivity and heat capacity for all the materials in our devices: Si-N, Pt, Cu) make it impossible to completely generalize. However, we have simulated over a much wider range of block temperatures (corresponding to different ratios of the relevant physical properties) without any qualitative changes.

2.2.1   Metallic "Wings"

One of the major concerns of using the semi-adiabatic relaxation technique for measuring these small bulk crystals is that though these samples are tiny by traditional "bulk" standards, they are 10-100 times larger in mass than our standard thin film samples. Because the thermal conductance is determined by the device geometry, this 10-100 times larger mass (and, therefore, heat capacity) results in a 10-100 times increase in τ, the relaxation time. That places us in the regime where an individual decay could take tens of seconds and, given the number of decays for a standard measurement, extends the time
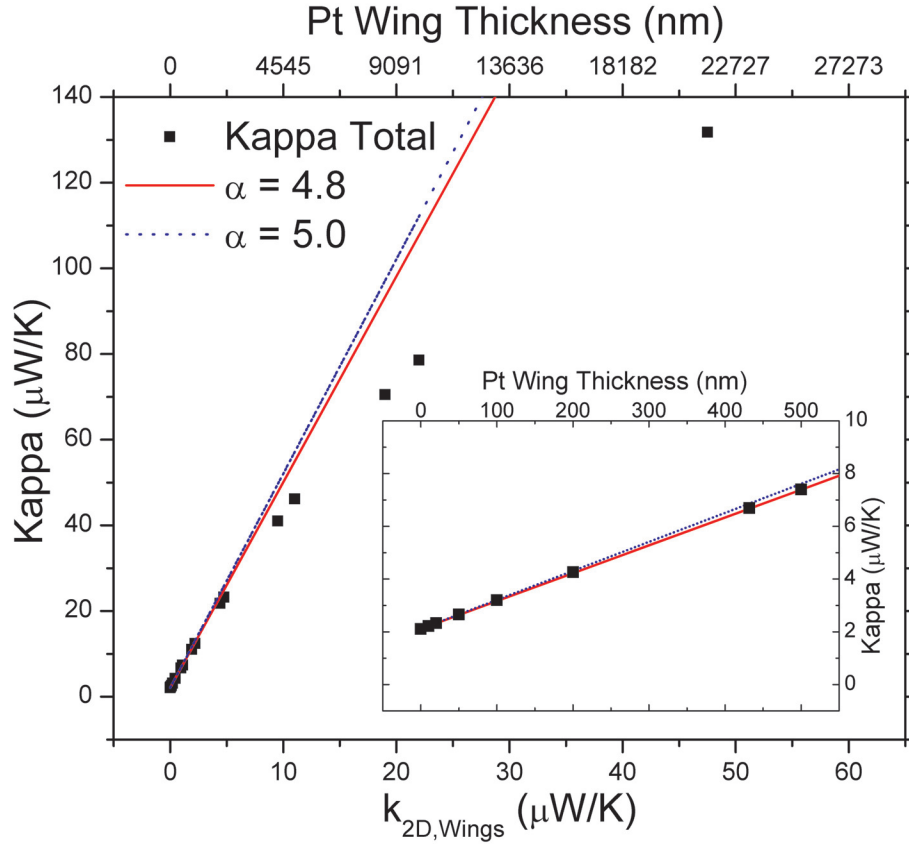
Figure 2.3: Thermal conductance (defined by $\kappa = P/\Delta T$) of the "wings" as a function of k_{2D}/thickness. Lines show a simple additive model for $P/\Delta T = \kappa_{NoWings} + \alpha k_{Pt} h_{Wings}$. Note how close the geometric factor α is to our naïve "square" model approximation of 5. Deviation from the linear model is due to an improperly defined ΔT (the sample area is no longer isothermal to $\sim 2\%$).

for an individual point to an hour or more. To counteract this effect, we need to increase κ, the thermal conductance of the device. While increasing the thickness of the low-stress nitride membrane would accomplish this, that increases the addenda by the same factor. A preferable technique is increasing the thermal link between the central sample region and the silicon frame using metallic "wings". The shape of the wings (Figure 2.1) stems from the need to isolate the wings electrically from the thermometers/heaters while being limited to the top side of the device due to our processing technique. However, this added asymmetric link can affect our technique by potentially disturbing the temperature contour lines, obfuscating the connection between the measured temperature difference ΔT at the center of the device and the conductance κ. The simulated data shown for the winged devices is for typical parameters of thick-membrane devices, but because this is simply a geometric scalar, the trends will hold for thin-membrane devices as well.
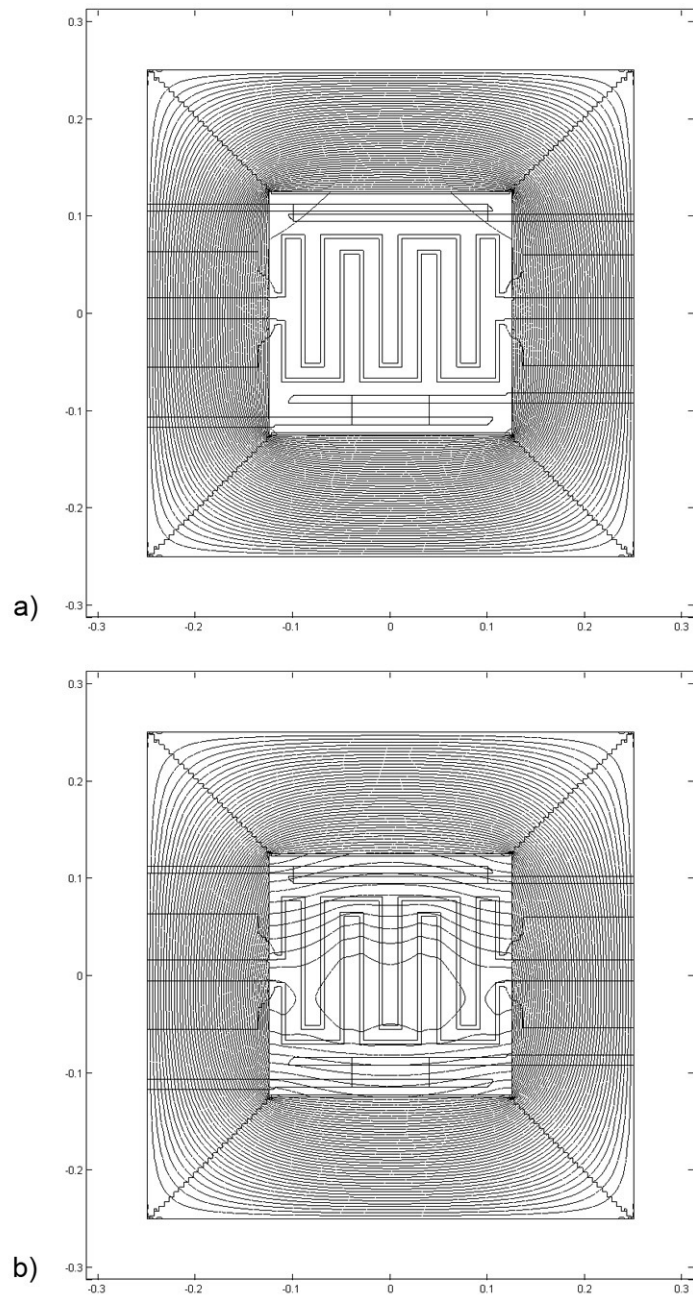
Figure 2.4: a) A temperature contour plot for a device with Pt "wings" 50nm thick, as in our bulk devices (Figure 2.1). b) A temperature contour plot for a device with Pt "wings" ~1μm thick. Two-percent contour lines are shown. Note the lack of uniformity in the central, sample region despite the presence of 1.5μm Cu conduction layer on top of the 1.5μm LSN membrane.

Figure 2.3 shows how the thermal link between membrane and frame changes with the added Pt "wings". Kappa here is again defined as $P/\Delta T$ where ΔT is measured at the center of the device. With a moderate thickness of platinum, we see a considerable increase in the high temperature thermal conductance (e.g. $\sim$50% increase with 1000Å of Pt). In the low $k_{2D,wings}$ limit, the contribution of the wings to κ is linearly additive ($\kappa_{tot} = \kappa_{wings} + \kappa_{mem}$), and we can extract the effective geometric factor for the wings ($\kappa_{wings} = k_{Pt} \cdot \alpha \cdot h$, where α is the geometric factor representing the effective width:length ratio of the conduction path). In a very naïve idea of what the geometric factor should be, we would estimate $\alpha \approx 5$[98]. Indeed, in the low Pt thickness linear regime shown in Figure 2.3, the slope $\alpha \approx 4.8 \pm 0.1$, very close to our simple approximation.

As the conductance through the wings becomes a larger fraction of the thermal link between sample area and frame, the heat flow contours become distorted (Figure 2.4). This distortion is what causes the apparent non-linear behavior at wing thicknesses above $\sim 1\mu m$ in Figure 2.3. It is due not to a non-linear relationship in the real thermal conductance but to the fact that as the heat flow contours change in this way, ΔT is no longer well-defined, thus yielding an errant result for $\kappa = P/\Delta T$. Clearly, remaining in the linear regime is crucial to the accurate measurement of specific heat with our devices.

2.2.2   The Sample

Because these bulk samples are so much larger than our traditionally-measured thin film samples and hence have much larger $c_{2D,s}$ and $k_{2D,s}$, it is important to quantify the potential effects this may have on our devices and the relaxation method of determining c_s, both in the steady-state and time-dependent aspects of the technique. The sample's size brings into question the potential hazard of a weakly thermally conductive sample; understanding under what conditions this introduces a distributed τ_2 effect and how to recognize it are extremely relevant to the experimental application of this technique. Also of concern is the thermal link between the sample and the device, as that can lead to a lumped τ_2 problem. Finally, quantifying any systematic errors is crucial to understanding the absolute precision of this methodology.

Because the path length for heat flow in the lateral direction is 3 to 4 orders of magnitude larger than that in the vertical direction, we have treated our devices with a two-dimensional model to this point. However, the geometry of a small bulk sample is inherently three-dimensional. To add such a sample to our model, we make the continued assumption that there is no radiative heat loss to the environment. If $k_s \approx k_{Cu}$, the internal time constants remain fast compared to τ for an average sized sample (we refer from here on to a disc $50\mu m$ high and $140\mu m$ in diameter, but we have simulated for various diameter samples with no qualitative changes), and we may continue to use our traditional 2-D model (which yields results of $< 2\%$ error in heat capacity for all c_s[98]). However, as k_s decreases, the internal time constants become longer and our simple model starts to break down. This is also the case if our sample is weakly coupled through the thermal link (referred to here as silver paint since that it what is used experimentally, as discussed in Section 2.3). In either situation, the heat equations in the in-plane, or horizontal, and out-of-plane, or vertical, directions are controlled by diffusion constants

$$D_h = \frac{k_{2D,Cu} + k_{2D,s} + k_{2D,Si-N} + k_{2D,Ag}}{c_{2D,s} + c_{2D,Ag}}$$

$$D_v = \frac{k_{2D,s}k_{2D,Ag}\left(h_s + h_{Ag}\right)^2}{\left(k_{2D,s}h_{Ag}^2 + k_{2D,Ag}h_s^2\right)\left(c_{2D,s} + c_{2D,Ag}\right)}, \quad (2.2)$$

respectively[30][a]. Combining this with the diffusion equations that set the respective time constants, $l^2 = 2D_h\tau_h$ and $(h_s + h_{Ag})^2 = 2D_v\tau_v$ (where l refers to the radius of the sample and h_s and h_{Ag} refer to the heights of the sample and thermal link, respectively), leaves us with a limit on the crucial time dependence of our system. Here τ_v is limited by the thermal diffusivity and geometry of the sample and thermal link, while τ_h is the combined result of all device and sample layers (though often dominated by conduction through the conduction layer).

In the case of $\tau_h \geq \tau_v$, we are left in the two-dimensional model already well characterized in previous work on thin films[98]. However, in the limit that $\tau_h \ll \tau_v$, we treat the tiny sample region as though the only link to the copper layer is through the thermal link. In this case, the 2-D mesh in the sample area represents the path for heat flow in the vertical direction, into (and through) the sample. Thus, in the sample area of our simulated device, k_{2D} is simply equal to $k_{2D,s}$.

As the thermal conductivity of the sample drops, this limit of $\tau_h \ll \tau_v$ occurs when $[(l^2/h_s h_{Cu})k_s] \ll k_{Cu} + k_{Ag}(h_{Ag}/h_{Cu})$[b], which is true for many relevant small samples mounted on our "thick" devices. For example, in the case of the CoO sample measured at low temperature (here values are quoted at 10K), $l = 50\mu m$, $h_s = 20\mu m$, $h_s = 10\mu m$, $h_{Cu} = 2\mu m$, $k_{Ag} \approx .4W/cm/K$, $k_s \approx .1$ W/cm/K, and $k_{Cu} = 35$ W/cm/K, yielding $\tau_h = \tau_v/5.9$. However, a glassy sample of similar dimensions would have $\tau_h \approx \tau_v/1000$ at low temperature due to the orders of magnitude lower thermal conductivity, while a metal may resut in $\tau_h \approx \tau_v$.

Steady State; $\frac{\partial T}{\partial t} = 0$

A crucial step of this simulation is confirming that the added bulk sample is at the same temperature as the thermometers and does not perturb the temperature contours. Figure 2.5 shows contour lines for a sample of moderate thermal conductivity ($k_{2D,s} = k_{2D,Si-N}$) placed near the heater. We see that the sample area remains isothermal to 2.5% for a wide range of total heat capacities ($1 \times 10^{-5} < c_s/c_{Cu} < 1 \times 10^3$). Changing the location of the sample did not affect the temperature contours. We note that the change in temperature ΔT measured by the thermometers remains the same, thus our measured κ is unchanged upon the addition of a sample, as expected.

---

[a]Here we have modeled the lateral direction as a multi-layer, or parallel, system, while the vertical direction can be thought of as a series conductive path. The additional heat capacities of the membrane and copper layers are negligible ($\approx .1\%$) given the small region of the device we are examining and so do not appear in the equations.

[b]This holds true assuming the limiting factor is the sample thermal conductivity (i.e. good thermal link). We also use the fact that $h_s < l$ for a typical sample.
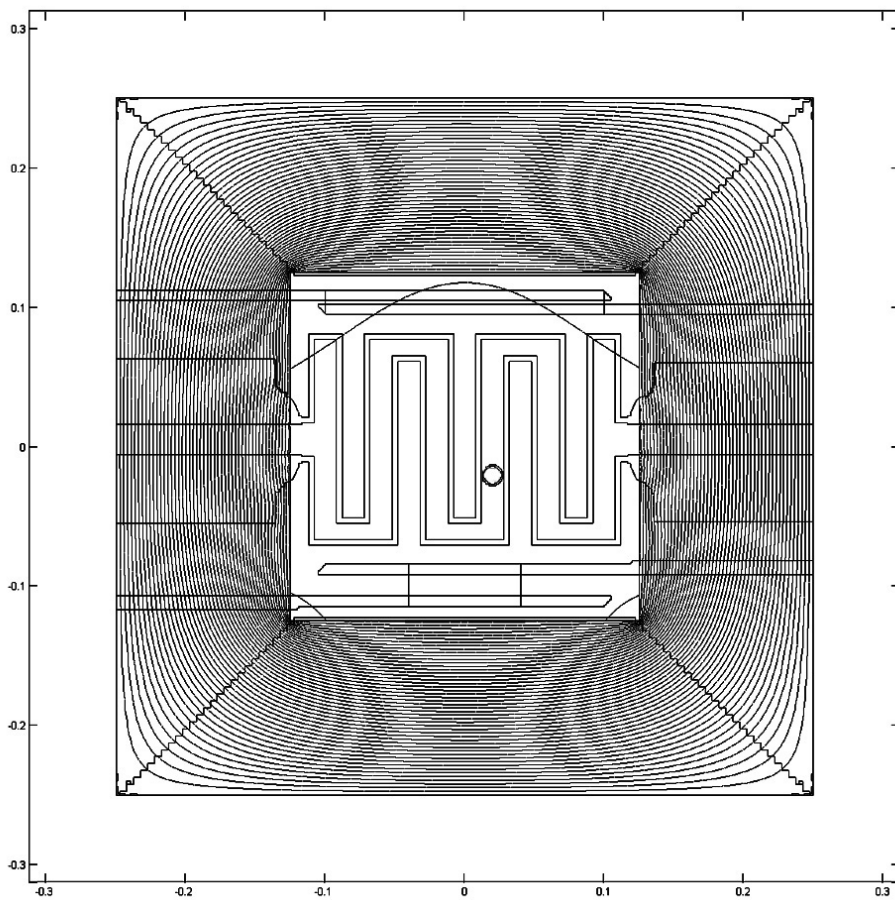
Figure 2.5: Temperature contour plot at constant power for a sample (circle near center of the membrane; the thick border represents the thermal link, silver paint) of comparable total heat capacity to the copper conduction layer (62.5 nJ/K) and thermal conductivity $k_s = 0.1 \times k_{Si-N}$. 2% contour lines are shown. For this set of conditions, the central region is isothermal to 2.5% and thermometers are within 0.6% of sample.
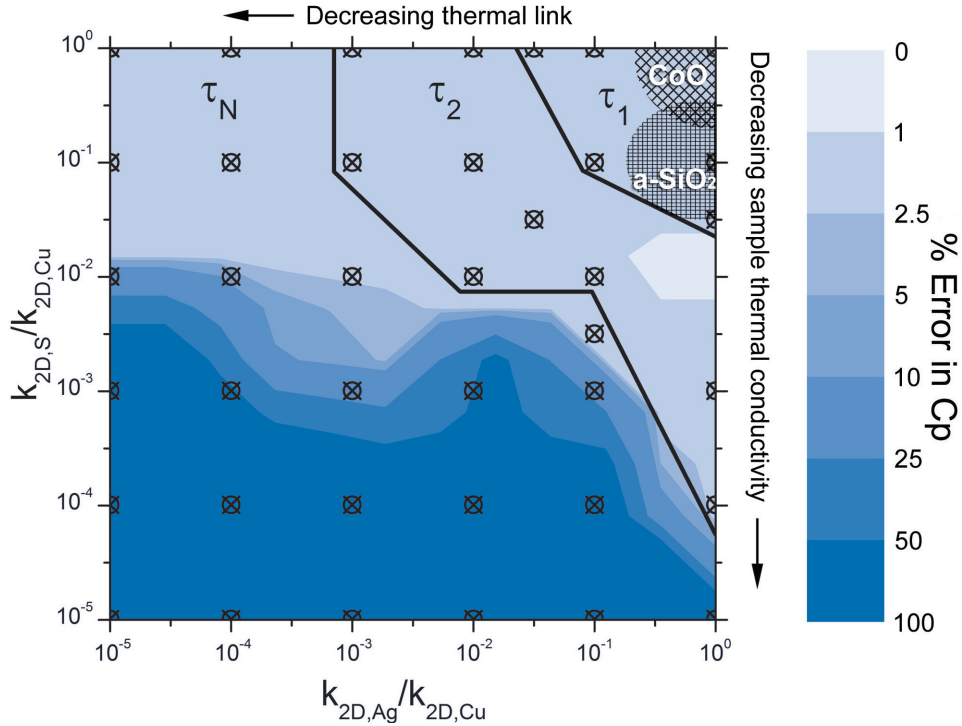
Figure 2.6: The % error in $c_{s,sim}$ as a function of $k_{2D,s}$ and $k_{2D,Ag}$; c_s was held constant at $c_s = c_{Cu}$. $c_{s,sim}$ was calculated from the τ_1 model in the region labeled "τ_1" and from the lumped τ_2 model everywhere else. The borders between the different tau regimes correspond to the horizontal lines in Table 2.1. Note that the error in the τ_1 and τ_2 regimes remains within 2.5%, comparable to our earlier work on thin films[98]. The cross-hatched region labeled CoO represents the approximate parameter space of our CoO experimental results (Section 2.3). The hatched region labeled SiO$_2$ is representative of where a $\approx 1\mu$g size disc of SiO$_2$ would approximately lie on this graph.

Time Dependence; $P = 0$

In order to quantify the error in this technique, we treat the simulation as we would an experimental measurement. We simulate an addenda measurement without the sample, first obtaining the steady-state ΔT to find $\kappa = P/\Delta T$ and then the time-dependent data, $T(t)$. We then take this time-dependent data and fit it to an exponential to obtain the time constant τ. Multiplying κ by τ yields a measure of the addenda heat capacity.

After obtaining the "addenda", we "add" the sample and repeat these simulations to obtain a measurement of the total heat capacity and take the difference to be the heat capacity of the sample itself. The difference between this simulated value and the value input for c_s is what we define as the absolute error in our technique.

Because there is now a macroscopic thermal link between our sample and the device, we must consider how this effects the time constant(s) of the system. If the thermal
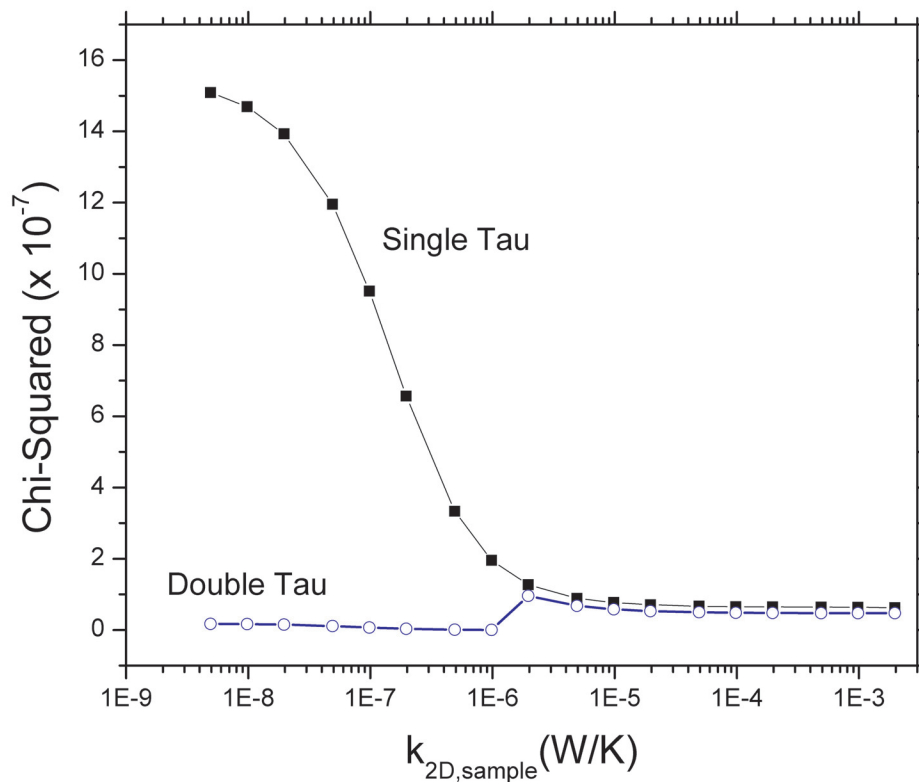
Figure 2.7: Chi-squared error of the single and double exponential fits to the temperature decay as a function of $k_{2D,sample}$ ($k_{2D,Agpaint} = k_{2D,Cu}$); c_s was held constant at $c_s = c_{Cu}$, but we have simulated over a variety of values for c_s with no qualitative change in behavior. Note the extremely large increase in χ^2 as the thermal conductivity of the sample becomes small (region where $\tau_{int} \approx \tau$).

link is weak, we expect to see a lumped τ_2 effect[105].

In the region where the single tau model breaks down, we analyze the data using the standard "lumped τ_2" model[105]:

$$T(t) = A_1 e^{-t/\tau_1} + A_2 e^{-t/\tau_2} \tag{2.3}$$

$$c_s + c_{addenda} = \frac{\kappa(A_1\tau_1 + A_2\tau_2)}{A_1 + A_2}. \tag{2.4}$$

Our simulation reproduces the "lumped τ_2" behavior in the traditionally appropriate region (high k_s, decreasing k_{Ag}, as shown in Figure 2.6).

Figure 2.7 shows the χ^2 error between $c_{s,sim}$ and $c_{s,actual}$ as a function of $k_{2D,s}$ for fixed $k_{2D,Ag} = k_{2D,Cu}$ (i.e. for a strong thermal link). For these simulations we have chosen $c_s = c_{Cu}$. We have also simulated for other sample heat capacities (which then affects τ_{int} and thus the region of deviation from a single τ model), but it did not affect the absolute error of the technique. Fitting to the classic single exponential model discussed, there is an abrupt increase in error at $k_{2D,s} \approx 2 \times 10^{-6}$ W/K. This corresponds precisely to the region where $\tau_{int} \sim \tau$, as expected.

The effect associated with this breakdown is considered the distributed τ_2 problem, though it is better characterized as a τ_N problem[34]. As higher order time constants exhibit themselves, the analysis becomes exceedingly complicated. However, in the condition that the thermal link between the sample and device is extremely strong, the heat flow is typically dominated by the τ_1 term, and the lumped τ_2 model provides an adequate approximation to the solution.

Figure 2.7 shows that χ^2 drops by an order of magnitude using this two-tau technique when in the regime where $\tau_{int} \gtrsim \tau$. This drastic decrease in error (order of magnitude smaller chi-squared error in fit) allows us to determine from the raw data whether or not we are observing any τ_2 effects — namely, a single exponential model is appropriate if $\chi^2(1\tau)/\chi^2(2\tau) < 2$. Similarly, we define the τ_N (or "distributed") regime when $\chi^2(2\tau)/\chi^2(3\tau) > 2$. Table 2.1 lists the χ^2 results for the various exponential fits, delineating the regime where each model is appropriate. This ability to monitor deviations from the single exponential model is crucial for our experimental analysis of the semi-adiabatic relaxation method with real samples, as parameters such as sample thermal conductivity remain unknown in our technique.

In Figure 2.6, we show the percent error in the obtained c_s as measured relative to $c_{s,input}$. Included in Figure 2.6 is information about the parameter space for an cobalt oxide sample measured on one of our thick devices (Section 2.3) as well as a small ($\approx 1\mu$g, a disc roughly 200 μm in diameter and 10μm tall) representative low conductivity sample, SiO$_2$, if it were to be measured on one of our thin devices. As a reminder, one must take into account the heights of the sample and copper layer as well as the temperature-dependent thermal conductivities when determining where on this plot a particular sample of interest may lie.

When fit to the appropriate experimental model (determined by the χ^2 ratio as in Table 2.1), the error in this new technique remains <2.5% under conditions representative of our actual experimental setup ($k_{Cu}/k_{mem} \sim 100$, c_{Cu} and c_{mem} given by experimental values[111, 119]), similar to our previous results[98]. The "lumped" τ_2 model thus adequately fits in many cases what is inherently a τ_N problem. In regimes where a single

Table 2.1: Table of Simulation Results. The results of the time-dependent data fit to various models are shown below. Horizontal lines delineate the three tau regimes. We list the χ^2 error for single, double, and triple exponential fits along with the % error for $c_{s,sim} - c_{s,actual}$. A single tau model fits appropriately when $\chi^2(1\tau)/\chi^2(2\tau) < 2$. Similarly a double exponential model is deemed appropriate when $\chi^2(2\tau)/\chi^2(3\tau) < 2$. If neither the single tau or two-tau models fit well, we consider this the "distributed" τ_2, or τ_N, regime as labeled in Figure 2.6. Note that datapoints in the single and double exponential regimes yield errors $< 2.5\%$ when fit to the appropriate model.

$\dfrac{k_{2D,Ag}}{k_{2D,Cu}}$	$\dfrac{k_{2D,s}}{k_{2D,Cu}}$	$\chi^2(1\tau)$	$\chi^2(2\tau)$	$\chi^2(3\tau)$	$\dfrac{\chi^2(1\tau)}{\chi^2(2\tau)}$	$\dfrac{\chi^2(2\tau)}{\chi^2(3\tau)}$	% Error in c_s	
							1τ	2τ
1×10^0	1×10^0	8.18×10^{-10}	6.18×10^{-10}	6.30×10^{-10}	1.324	—	1.34	—
1×10^0	1×10^{-1}	1.27×10^{-7}	9.58×10^{-8}	4.46×10^{-8}	1.328	—	1.98	—
1×10^0	3×10^{-2}	8.25×10^{-9}	5.71×10^{-9}	6.54×10^{-9}	1.446	—	1.56	—
1×10^{-1}	1×10^0	7.42×10^{-10}	5.77×10^{-10}	5.87×10^{-10}	1.285	—	-1.32	—
1×10^{-1}	1×10^{-1}	1.73×10^{-9}	1.43×10^{-9}	1.46×10^{-9}	1.211	—	-1.36	—
3×10^{-2}	1×10^0	1.65×10^{-9}	1.37×10^{-9}	1.40×10^{-9}	1.204	—	-1.38	—
1×10^0	1×10^{-2}	6.57×10^{-7}	3.13×10^{-9}	2.29×10^{-9}	210.0	1.368	0.41	-0.56
1×10^0	1×10^{-3}	1.39×10^{-6}	1.49×10^{-8}	8.57×10^{-9}	93.61	1.737	-6.52	-1.59
1×10^0	1×10^{-4}	1.51×10^{-6}	1.73×10^{-8}	9.56×10^{-9}	87.45	1.806	-7.88	-1.84
1×10^{-1}	1×10^{-2}	1.79×10^{-7}	3.68×10^{-10}	2.81×10^{-10}	485.8	1.308	-3.60	-1.31
3×10^{-2}	3×10^{-2}	2.94×10^{-8}	1.49×10^{-11}	1.15×10^{-11}	1966	1.299	-1.92	-1.23
1×10^{-2}	1×10^0	2.44×10^{-8}	8.03×10^{-12}	7.92×10^{-12}	3036	1.013	-1.82	-1.20
1×10^{-2}	1×10^{-1}	4.52×10^{-8}	3.04×10^{-11}	2.32×10^{-11}	1484	1.313	-2.11	-1.23
1×10^{-2}	1×10^{-2}	5.43×10^{-7}	9.43×10^{-10}	7.27×10^{-10}	576.2	1.297	-5.91	-1.35
1×10^{-3}	1×10^0	2.57×10^{-6}	1.83×10^{-9}	1.43×10^{-9}	1404	1.280	-14.79	-1.25
1×10^{-3}	1×10^{-1}	2.99×10^{-6}	1.98×10^{-9}	1.49×10^{-9}	1510	1.326	-16.64	-1.29
1×10^0	1×10^{-5}	6.41×10^{-8}	1.61×10^{-8}	2.42×10^{-9}	4.238	7.022	-87.80	-64.17
1×10^{-1}	3×10^{-3}	1.52×10^{-6}	3.73×10^{-9}	6.66×10^{-12}	407.8	559.8	-13.21	-1.53
1×10^{-1}	1×10^{-3}	4.00×10^{-6}	2.40×10^{-8}	6.81×10^{-10}	167.0	35.19	-38.89	-2.97
1×10^{-1}	1×10^{-4}	8.79×10^{-7}	3.51×10^{-8}	3.58×10^{-9}	25.01	9.814	-82.98	-58.19
1×10^{-1}	1×10^{-5}	7.33×10^{-8}	1.84×10^{-8}	2.77×10^{-9}	4.846	8.028	-87.78	-65.72
1×10^{-2}	1×10^{-3}	9.36×10^{-7}	3.76×10^{-8}	4.01×10^{-9}	24.86	9.373	-82.03	-56.34
1×10^{-2}	1×10^{-4}	9.36×10^{-7}	3.76×10^{-8}	4.01×10^{-9}	24.86	9.373	-82.03	-56.34
1×10^{-2}	1×10^{-5}	7.80×10^{-8}	1.95×10^{-8}	2.95×10^{-9}	5.153	8.538	-87.89	-67.36
1×10^{-3}	1×10^{-2}	5.12×10^{-6}	2.94×10^{-9}	1.28×10^{-12}	1742	2289	-27.37	-1.44
1×10^{-3}	1×10^{-3}	6.50×10^{-6}	3.17×10^{-8}	1.40×10^{-9}	205.5	22.61	-62.86	-4.41
1×10^{-3}	1×10^{-4}	1.03×10^{-6}	4.38×10^{-8}	4.70×10^{-9}	23.47	9.313	-87.14	-60.91
1×10^{-3}	1×10^{-5}	6.05×10^{-8}	1.51×10^{-8}	2.29×10^{-9}	3.997	6.622	-88.87	-76.17
1×10^{-4}	1×10^0	7.72×10^{-6}	3.15×10^{-9}	2.06×10^{-13}	2453	15306	-42.15	-1.09
1×10^{-4}	1×10^{-1}	8.42×10^{-6}	3.33×10^{-9}	1.59×10^{-9}	2533	2.097	-48.99	-1.13
1×10^{-4}	1×10^{-2}	7.50×10^{-6}	5.39×10^{-9}	1.07×10^{-9}	1391	5.015	-77.46	-1.76
1×10^{-4}	1×10^{-3}	2.32×10^{-6}	9.31×10^{-9}	1.80×10^{-9}	249.7	5.181	-96.32	-11.49
1×10^{-4}	1×10^{-4}	4.27×10^{-7}	1.25×10^{-8}	2.74×10^{-9}	34.08	4.574	-95.00	-75.38
1×10^{-4}	1×10^{-5}	7.47×10^{-8}	1.87×10^{-8}	2.82×10^{-9}	4.936	8.178	-94.60	-75.70
1×10^{-5}	1×10^0	8.43×10^{-6}	3.34×10^{-9}	2.14×10^{-13}	2527	15575	-48.76	-1.06
1×10^{-5}	1×10^{-1}	8.92×10^{-6}	3.52×10^{-9}	2.26×10^{-13}	2533	15587	-56.88	-1.11
1×10^{-5}	1×10^{-2}	5.12×10^{-6}	6.03×10^{-9}	1.94×10^{-9}	849.7	3.102	-88.55	-2.35
1×10^{-5}	1×10^{-3}	7.60×10^{-8}	1.90×10^{-8}	2.87×10^{-9}	5.024	8.324	-97.24	-75.32
1×10^{-5}	1×10^{-4}	9.52×10^{-8}	2.38×10^{-8}	3.60×10^{-9}	6.287	10.416	-98.09	-78.48
1×10^{-5}	1×10^{-5}	6.68×10^{-8}	1.67×10^{-8}	2.52×10^{-9}	4.412	7.309	-98.06	-78.56

exponential model is appropriate we can expect systematic errors in the C_P of small samples similar to that of thin films.

2.3 Experiment

2.3.1 Silver paint thermal link

After obtaining the limits in our technique from numerical simulation, we can apply this knowledge toward the experimental measurement of small bulk samples on our membrane-based calorimeters. We have previously measured powder samples suspended in a liquid and dropped onto devices[2, 3] and have also successfully measured small single crystals or other bulk samples (200-500 μg) thermally anchored to thick membrane devices by using indium to attach the samples[61]. The indium, however, requires physical pressure, which is incompatible with the thinner membranes needed for small single crystal ($<$100 μg) samples, and the heat necessary for the In attachment procedure is not suitable for metastable samples such as quenched high-pressure phases. Our first attempt to use gallium (which has a lower melting point) to replace the indium was unsuccessful due to poor wetting characteristics of Ga on the desired oxide samples (in contrast to good wetting on metals). The wide temperature range desired makes conducting grease (commonly used in the literature for low temperature measurements) a poor option, since Apiezon$^{\circledR}$ N grease has a glass transition at 210-237K and a history-dependent crystallization transition at 270-289K (Figure 2.8a), leading to a widely-varying and very large heat capacity unsuitable for our technique[67, 104]. We therefore turned to and have developed the use of silver paint[c] which is commonly used to attach electrical leads to samples. This can be diluted with butyl acetate to a useful consistency to attach samples and accurately weighed upon the evaporation of the solvent.

After placing the sample (one or more small crystals of known mass) on the center of the thermal conduction layer, the diluted silver paint is dropped onto the sample and allowed to dry overnight in a vacuum desiccator. We have measured the mass of the resulting system over a period of days after this process, and find an initial rapid decrease as the solvent evaporates which is further reduced less than 1% per day after 24 hours.

Once the butyl acetate solvent has evaporated, the resulting thin layer of paint holds the sample securely. Silver paint is designed and experimentally found to give good electrical contact, and its thermal conductivity is also quite high[28]. The relaxation method used for measurement directly shows whether this thermal contact is good or not, as good thermal contact yields a single exponential decay, while poor thermal contact would show the classic double exponential τ_2 effect. We have verified that the resulting thermal decays of the relaxation method for a bulk sample are that of a single time constant, justifying our assumption of the paint providing good thermal contact between sample and calorimeter. We have been able to achieve robust physical and thermal contact with silver paint mass below 10μg. This new approach to mounting samples thus provides an avenue for measuring bulk samples with smaller mass than can be measured by traditional techniques.

We find that silver paint has a moderate heat capacity over the entire temperature

---

[c]S.P.I. Supplies High Purity Silver Paint, #05002-AB
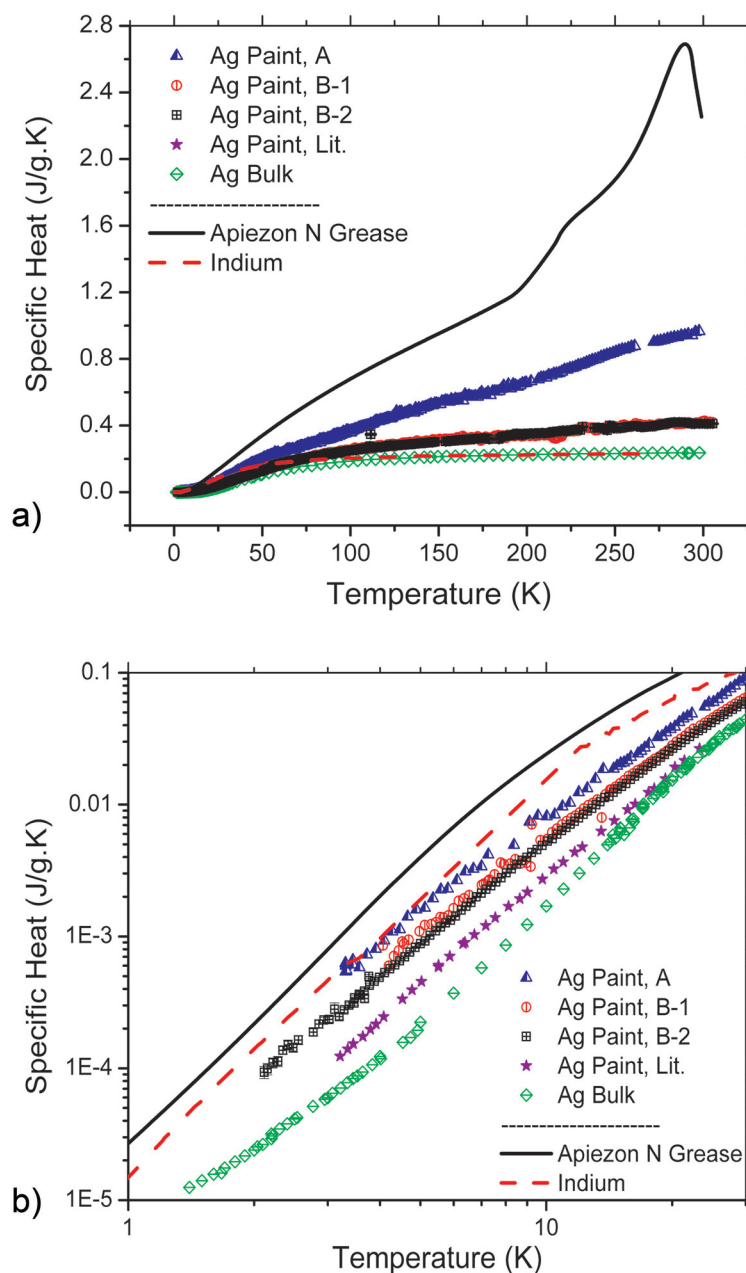
Figure 2.8: Measured specific heats of various sample mounting materials. The silver paint measurements labeled A, B-1, and B-2 were taken in our lab from two different bottles, the latter which was measured again (different sample from the same bottle). Also shown are literature values of silver paint[28], bulk silver[111], bulk indium[111], and Apiezon$^{\circledR}$ N grease[104]. Figure 2.8b is a logarithmic plot of the same data to emphasize the low temperature differences.

range (Figure 2.8), more than that of bulk silver, presumably because the bonding agent gives a significant contribution, but significantly less than (and more reproducible than) that of grease. This addenda contribution is consistent per bottle of silver paint (shown here as measurement B-1 and B-2), but we did see deviations between bottles A and B. At low temperatures(< 23K), we see that our measurement of silver paint is larger than that in the literature[28] (there is no high temperature data to compare to). This difference is likely due to a different solvent and/or bonding agent due to different manufacturers. Also of note, the magnitude of the specific heat of the silver paint is actually lower than that of indium at low temperature, making this method experimentally preferable even in cases where heating the device would not damage or alter the sample in any way. Unlike Apiezon® N grease, which clearly shows the strong temperature dependence characteristic of a glass transition, there are no apparent transitions in the silver paint. The total contribution of the silver paint to the aggregate heat capacity of a measurement is determined from its measured mass. The uncertainty in this mass (measured to ± 1 microgram) is often the largest contributor to the error in this new technique (outside of the 2% systematic error already discussed in Section 2.2.2).

2.3.2   CoO reference sample

As an experimental test of absolute accuracy, we obtained a single crystal of cobalt oxide whose heat capacity had been measured recently by conventional cryogenic calorimetry by Woodfield and Boerio-Goates. A 638 μg sample was attached to a thick nitride membrane device (used for measuring large heat capacities) with 183 μg of silver paint from bottle B. We then measured the heat capacity of this device using the semi-adiabatic relaxation method[30]. The antiferromagnetic transition is quite well defined (Figure 2.9) and its temperature agrees with the adiabatic measurement. The heat capacities are also in good agreement.

For the data shown here, the error bars shown are calculated by adding in quadrature the following: 2% of the total C_P (due to systematic error in technique), 1 μg/[sample mass]$\times C_P$ (error due to $\pm 1\mu$g uncertainty of sample mass), 1 μg$\times c_{Ag}$ (error due to uncertainty in Ag paint mass), κ times the error in τ (error due to τ fit), and τ times the error in κ (calculated via 98% confidence bands in various polynomial fits). The error in κ fit is small (0.1-0.3%). The error in τ fit is on the order of 0.2-1%. There is also a 1% uncertainty in temperature due to thermometer calibration. Propagating all these errors suggests that an absolute accuracy on the order of 3% in heat capacity, dominated by the systematic errors discussed above, is attainable, as evidenced by the good agreement with the previously measured CoO.

2.3.3   Fe$_2$SiO$_4$ polymorphs

Having shown the viability of this technique on microgram quantities of material, we turned to measuring the heat capacity of the olivine polymorph of Fe$_2$SiO$_4$, fayalite. We see a slight depression and broadening of the transition relative to that seen in a study of a larger single crystal[102]. X-ray diffraction measurements proved that there was a significant amount of magnetite (Fe$_3$O$_4$) contaminant, thus leading to the broader transition observed
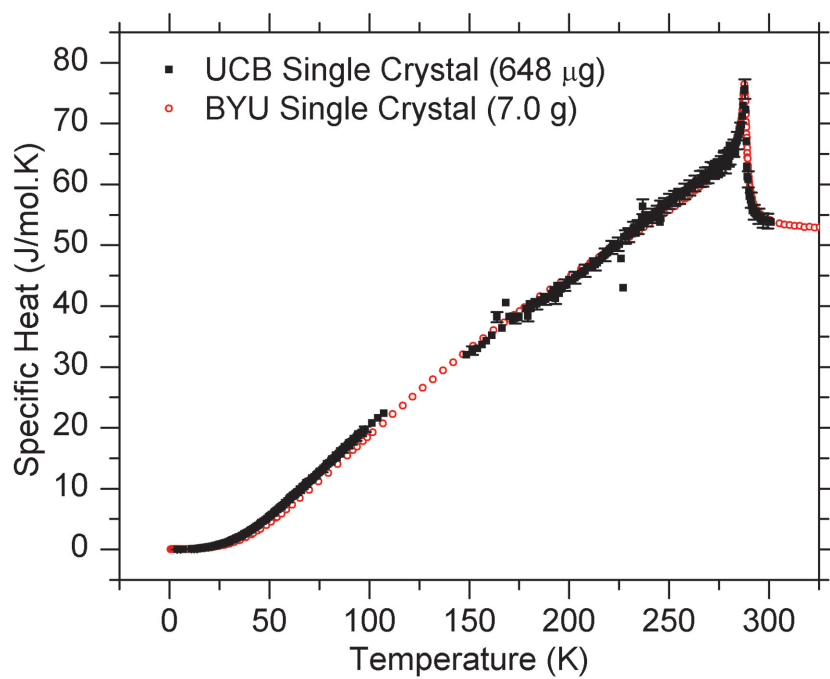
Figure 2.9: Specific heat of a $648\mu g$ single crystal of CoO measured by our microcalorimeter compared to the bulk measurement of a 7g sample of the same origin by our collaborators at BYU. Error bars are shown for every fifth data point, but below 100K they are as small as the points themselves.
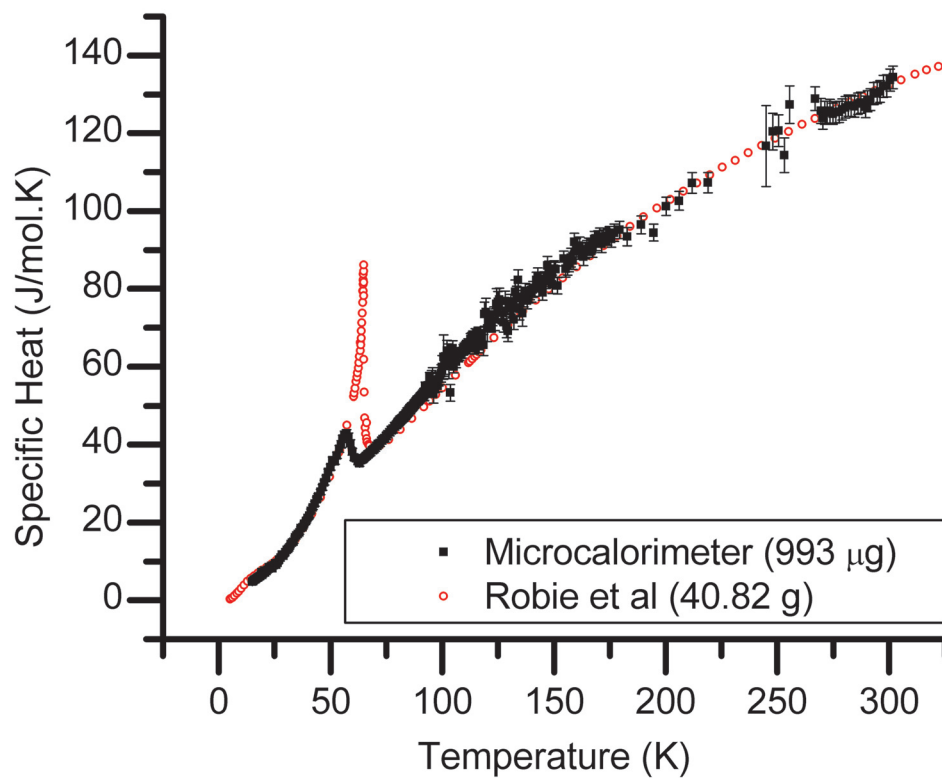
Figure 2.10: Comparison of the specific heat of fayalite measured with our microcalorimeters to that measured by Robie et al. using cryogenic calorimetry[102]. Error bars are shown at all temperatures for the present data.
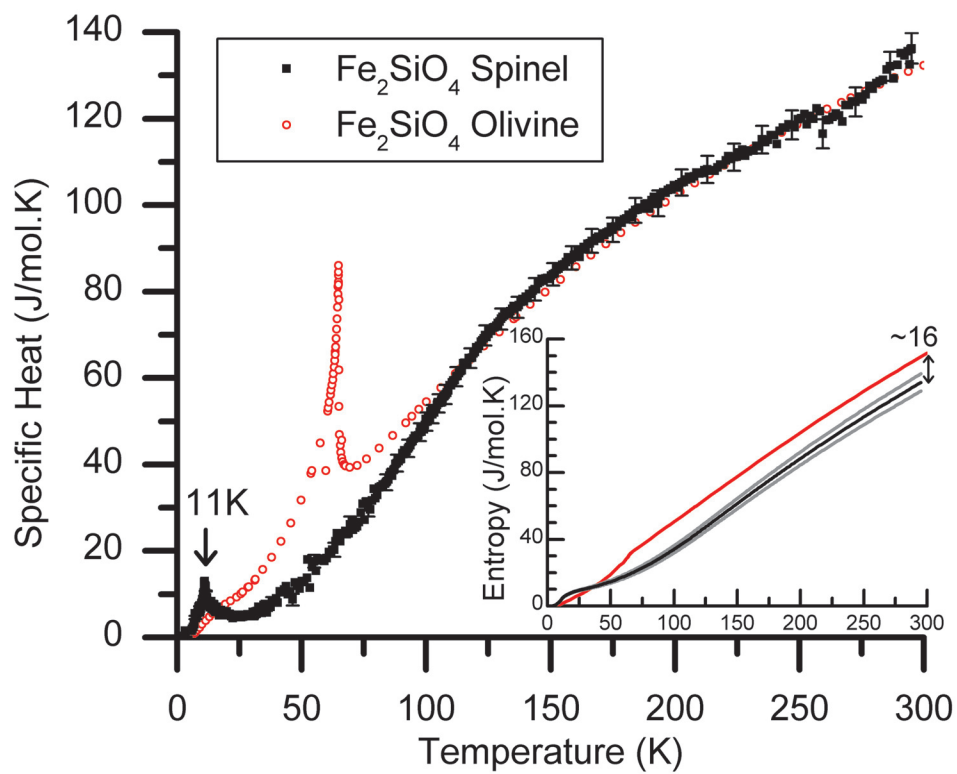
Figure 2.11: Comparison of the specific heat of the spinel phase of Fe_2SiO_4 as measured by our microcalorimeters to that of olivine[102]. Entropy for the two samples are shown in the inset. Error bars are shown for representative data points for the spinel.

in Figure 2.10.

Of primary interest, however, is the spinel phase of Fe_2SiO_4. This is a metastable phase that is found naturally in the earth's mantle, and measuring the enthalpy and entropy of this material would play a key role in informing simulations of the dynamics of the upper mantle. Important for this technique is the fact that though it is metastable, it can be quench-condensed in a lab environment by applying a large hydrostatic pressure with a diamond- or multi-anvil cell. Inherently these signs are designed with sub-milligram quantities of sample in mind, making our technique perfect for this application.

Before synthesizing the spinel phase, we obtained a second olivine powder, confirmed via X-ray diffraction to be devoid of any contaminant phases. Our collaborators then synthesized the spinel phase of the material in a multi-anvil apparatus. Further description of the characterization and methodology can be found elsewhere[88].

As we see in Figure 2.11, we see a lambda-type transtion at $\approx$ 11K, presumably the Neél transition observed at the same temperature by Mossbauer spectroscopy[109]. It appears that at high temperatures the specific heat contributions of the two phases collapse onto each other. In the inset, we show the entropy of the two phases. This is calculated by integrating the measured C_P/T upwards of 2.3K (the lowest measured temperature), with $\Delta S = 0$ below 2.3K. The precise contributions from 0 to 2.3K are negligible. By comparing the room temperature entropies of the olivine and spinel phases of Fe_2SiO_4, we see a constant difference at high temperatures of -16 ± 5 J/mol/K. This value is in good agreement with the value of -14 ± 3 J/mol/K obtained from an analysis combining phase equilibria and calorimetrically measured enthalpies of transformation[86]. The smaller entropy of the spinel is consistent with the positive P-T slope for the olivine-spinel transition. A further step would be to examine what happens to this transition upon alloying with Mg and whether we see the expected reduction in the magnitude of the difference in entropy between the two phases[86].

2.4   Conclusions

Heat flow analysis of our microcalorimeters with attached simulated bulk samples shows the feasibility of obtaining the heat capacity of small (1-1000 μg) samples. We have quantified the regime in which our devices are applicable and how to recognize when we are outside this regime. The heat capacity of silver paint has been measured, showing that it can reliably be used to affix samples to our "calorimeters on a chip" for samples with thermal conductivity as low as 2×10^{-5} W/cm/K at 20K for a typically sized sample. Experimental results show that this method works to similar accuracy (2.5%) as our traditional thin film calorimetric technique, expanding the realm of applicability to include such novel systems as quenched high-pressure materials, molecular magnets, and more. To that end, we measured the specific heat of the mineral and high-pressure polymorphs of Fe_2SiO_4 (olivine and spinel, respectively), showing a clear antiferromagnetic phase transition for both materials and yielding a resulting entropy difference between the two phases, -16 ± 5 J/mol/K, that agrees well with values resulting from a less direct analysis, -14 ± 3 J/mol/K.

Chapter 3

The role of the spin-density wave and disorder in the density of states of sputtered Cr films

3.1 Introduction

Though chromium's role in the giant-magnetoresistive Fe/Cr multi-layer system is often glossed over as merely a non-magnetic spacer layer, many recent studies have shown that understanding its magnetic behavior is crucial to understanding the complexities of the GMR structure (for a review, see Pierce, et al. [92]). Chromium's antiferromagnetic spin-density wave (SDW) can be manipulated not just through the confinement of the Fe/Cr structure[40, 91, 103], but also through strain and alloying in both the bulk (for a review, see Fawcett[36]) and in thin films[103, 68, 13]. The sensitive nature of the SDW has an impact on the total density of states (DOS) available at the Fermi surface due to the nesting responsible for the SDW and therefore is expected to play a role in GMR in the coupling mechanisms of the Fe/Cr multi-layer system[92, 108, 116].

The coupling of the Fe/Cr GMR system has been proven to be quite dependent upon disorder in the film[92, 114, 115]. The impact of disorder on chromium's magnetic characteristics has been well-established also, particularly in sputter-deposited films where disorder was controlled by sputter gas pressure and substrate temperature[13, 46]. This sensitivity allows one to affect the nature of the SDW through sputter deposition at various pressures[13]. With the well-established qualitative links between disorder and Cr's SDW and the coupling in the Fe/Cr GMR structure and Cr's density of states, the question remains as to whether these effects are linked and/or the relative significance of these effects in the oft-studied sputtered Fe/Cr GMR heterostructures.

3.2 Experimental Details

In order to examine the links between SDW, disorder, and density of states, we have sputtered Cr films at various pressures onto our micromachined calorimeters[30]. We
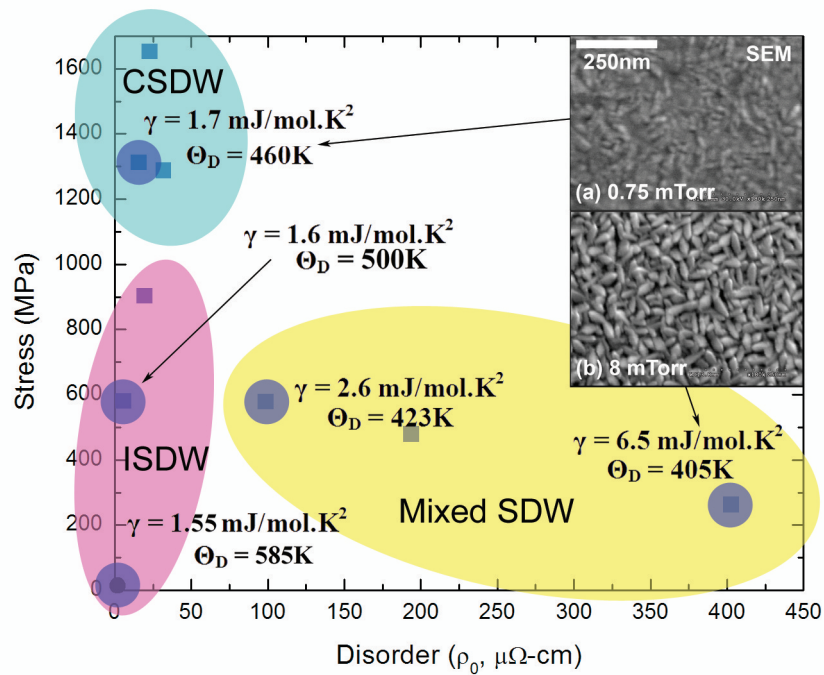
Figure 3.1: Magnetic phase digram for sputtered Cr as a function of disorder and stress[13]. Overlayed onto the phase diagram are the Sommerfeld coefficient γ and the Debye temperature Θ_D obtained from specific heat measurements. The inset shows SEM data for samples grown at low (a) and high (b) pressure. Note that though (a) and (b) have roughly equivalent grain size, the high pressure sample has significantly larger grain boundaries.
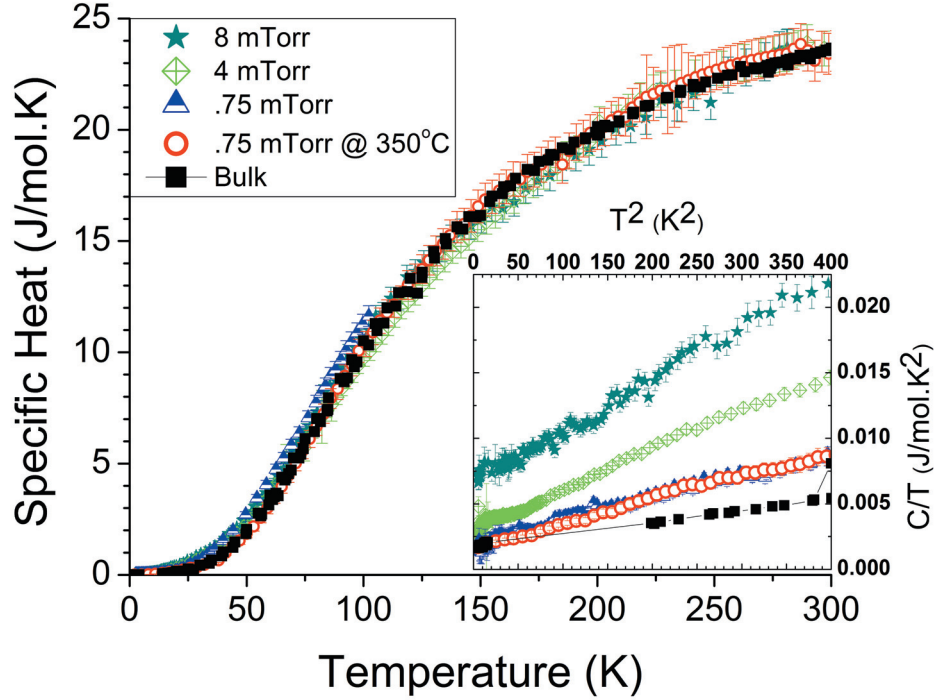
Figure 3.2: Specific heats of different sputtered Cr films compared to bulk data. Inset shows the C/T v. T^2 plot used to obtain the Θ_D and γ.

deposited a copper capping layer in-situ to eliminate the effect of surface oxidation (especially important on the more disordered films[13]). Relaxation calorimetry was used to measure the specific heat of the Cr films from 2-300K with the contributions of the copper layer and device calculated from a separate addenda measurement. We then fit this data below ~ 20K to C/T v. T^2 to obtain the Sommerfeld coefficient γ, proportional to $N(\varepsilon_F)$, and the Debye temperature, Θ_D (Figure 3.2 inset).

3.3   Results

Figure 3.1 shows a phase diagram for Cr in the stress-disorder plane with the different types of SDW shown schematically[13]. We overlay the heat capacity results onto this phase diagram. Stress was determined through use of a Tencor FLX-2320 to measure the wafer curvature before and after film deposition. SEM results in the inset of Figure 3.1 illuminate the contrasting structure of the low-pressure (a) and high-pressure (b) films. These differing grain structures lead to a change in density from the bulk of as much as 23% in the most disordered films (Table 3.1). This was taken into account when calculating the molar specific heat. Specific heat parameters γ and Θ_D are shown in Figure 3.3 as a function of disorder, where disorder is characterized by the low temperature resistivity value
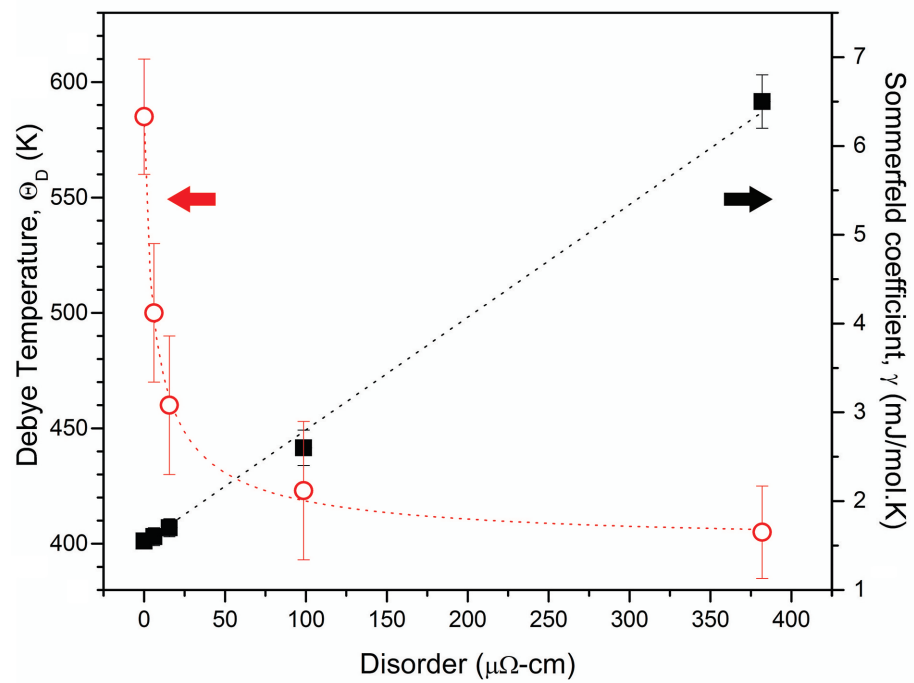
Figure 3.3: Measured γ (black squares) and Θ_D (red open circles) values as a function of disorder, where disorder is defined as the low temperature resistivity value, ρ_0. Dotted lines are simply guides to the eye.
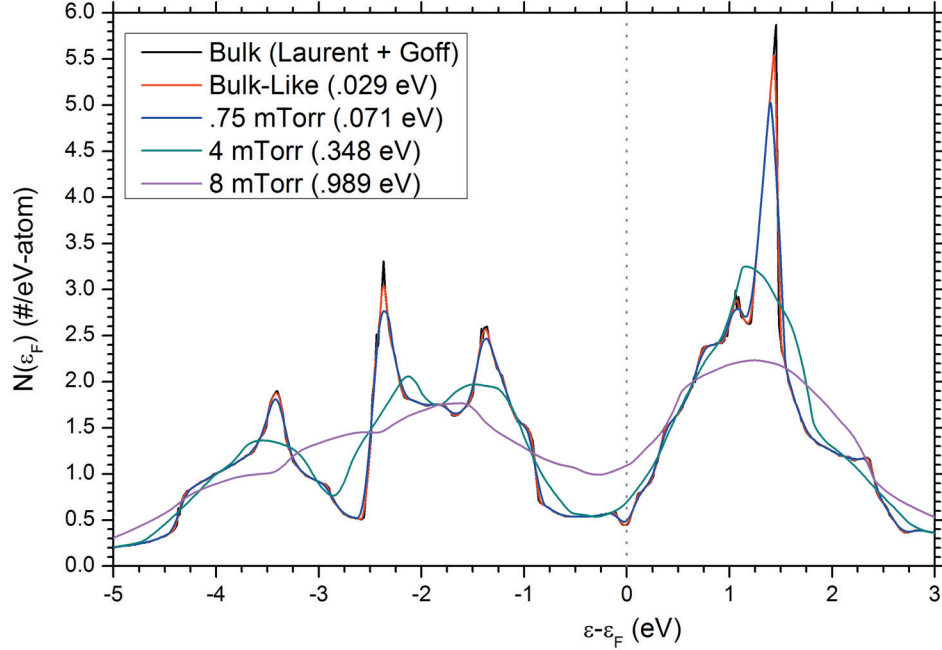
Figure 3.4: Calculated density of states for Cr modeled on Laurent et al.[72] with an explicit inclusion of the SDW gap in accordance with Goff[45]. Disorder broadening was calculated as a windowed average where the window width is determined by $\Delta E \Delta \tau \approx \hbar$, where τ is determined from the low-temperature conductivity (see Table 3.1).

ρ_0. Table 3.1 summarizes these results along with the calculated band structure density of states and electron-phonon coupling.

3.4   Discussion

Though there is no noticeable change in the Sommerfeld coefficient between the CSDW and ISDW samples, there is a distinct correlation between γ and disorder, where increasing disorder shows a strong increase in γ (Figure 3.3). With increasing disorder in these films, there is a corresponding increase in the size of the grain boundaries. TEM measurements show that these wide grain boundaries are often amorphous and, in general, the high-pressure films are exceptionally inhomogeneous[13]. As one would expect, this increasing disorder results in phonon softening, as evidenced in the decrease in Θ_D with increasing disorder (Figure 3.3). Despite the differing C_P parameters for the various samples, they all approach the same high temperature limit (Figure 3.2), which confirms that we are counting the modes for these disordered systems appropriately[37].

Though the grains are on the order of nanometers (≈ 25 nm), this leads to a surface to volume atomic fraction of $\lesssim 2\%$ for even the film with the smallest grains, far less than the 30% seen in the 8.4 nm Pd nanocrystalline system exhibiting an enhanced
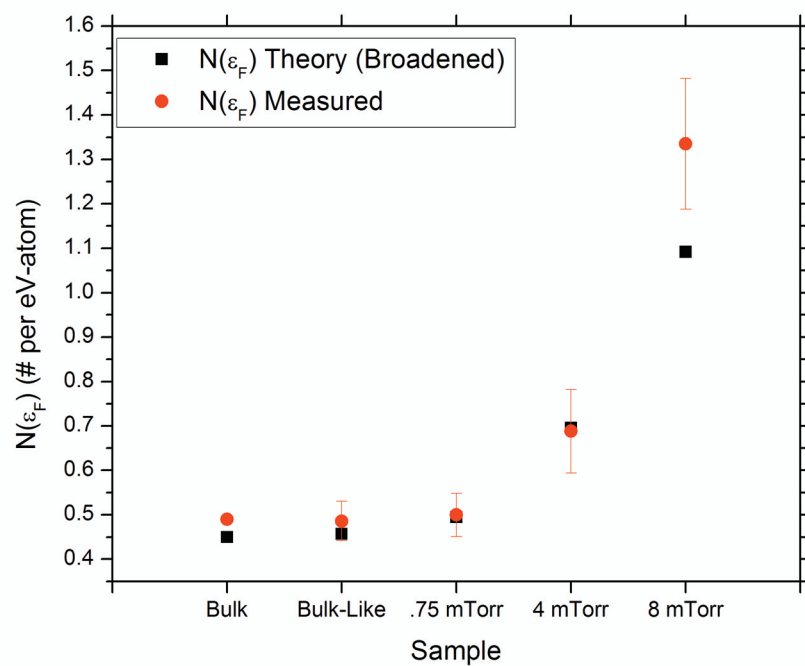
Figure 3.5: Calculated density of states for Cr modeled on Laurent et al.[72] with an explicit inclusion of the SDW gap in accordance with Goff[45]. Disorder broadening was calculated as a windowed average where the window width is determined by $\Delta E \Delta \tau \approx \hbar$, where τ is determined from the low-temperature conductivity (see Table 3.1).

Table 3.1: Table of experimental results on disordered sputtered chromium films compared to bulk Cr. Reference data is taken from Heiniger, et al.[52] Disorder is characterized by the low temperature resistivity, ρ_0[12].

Growth Conditions	Density (g/cm^3)	ρ_0 ($\mu\Omega$cm)	SDW State	γ ($\frac{mJ}{mol \cdot K}$)	Θ_D (K)	λ_γ	$N(\varepsilon_F)$ (/eV-atom)
Bulk	7.14	—	ISDW	1.55	585	.34[a]	.49[b]
.75 mTorr @ 350°C	7.14	$6.1 \pm .4$	ISDW	$1.6 \pm .1$	500 ± 30	$.35 \pm .05$	$.50 \pm .04$
.75 mTorr	7.14	$15.6 \pm .6$	CSDW	$1.7 \pm .1$	460 ± 30	$.37 \pm .06$	$.52 \pm .04$
4 mTorr	6.15	$98.6 \pm .6$	Mixed	$2.6 \pm .2$	423 ± 30	$.51 \pm .10$	$.73 \pm .10$
8 mTorr	5.53	382 ± 1	Mixed	$6.5 \pm .3$	405 ± 20	$.97 \pm .15$	$1.4 \pm .2$

[a] This value is obtained from heat capacity results[52], but there is a wide range of λ in the literature[5, 15, 80].
[b] See Laurent, et al.[72]

heat capacity[19]. Therefore, confinement and surface effects are not a significant effect in these Cr films. Furthermore, extrinsic enhancements such as oxidation or water as seen in TiO$_2$[14] are not relevant because we have capped the sputtered Cr films in situ.

The strong dependence of γ on disorder suggests disorder broadening of the density of states. From a simple comparison of the electronic lifetime in a disordered transition metal to that of the bulk, $\Delta E \Delta t = \hbar$ yields a broadening of 0.5-1 eV[26, 55]. The Fermi energy of the bulk lies at a minimum[72], so small changes due to disorder have large effects on the DOS (Figure 3.4). This is also further compounded by the SDW gap[45].

In order to model the effect of the broadening of the density of states, we took Laurent's calculations and explicitly added to them to Goff's model of the SDW gap. This represents the "bulk" state of the Cr DOS. Through Ohm's law and the low-temperature conductivity measurements[12], we obtained an estimate for the scattering time of an electronic state, using this to calculate the ΔE value as mentioned above. We then applied a windowed average to the "bulk" state using this value to define the window. The results are shown in Figure 3.4, where you can see the minimum "disappear" in the most disordered films. Figure 3.5 compares the values calculated for $N(\epsilon_F)$ from this broadened theoretical calculation to the experimental results given in Table 3.1.

The measured Sommerfeld coefficient $\gamma \propto N(\varepsilon_F)(1 + \lambda)$ where $N(\varepsilon_F)$ is the band structure density of states and λ is the electron-phonon coupling constant. An increase in the band DOS also has an effect on screening and, thus, electron-phonon coupling. According to McMillan's theory on transition metal superconductivity in the weakly-coupled case,

$$\lambda = \frac{N(\varepsilon_F) \langle \Im \rangle^2}{M \langle \omega \rangle^2} \tag{3.1}$$

where $\Im$ represents the electron-phonon matrix element[80]. It has been shown that the $\langle \Im \rangle^2 / (M \langle \omega \rangle^2)$ is roughly constant for transition metals[32], meaning any change in the phonon spectrum results in a compensating change in the coupling element. Thus, changes in λ are related strictly to changes in $N(\varepsilon_F)$, and from this relationship we can calculate $N(\varepsilon_F)$ and λ given γ and Θ_D (Table 3.1).

One sees that for the ISDW and CSDW states, the band-structure DOS does not change (to within error). Any difference due to the AFM is expected to be small[35] given that only a subset of the Fermi surface participates in the AFM interaction. Because ε_F

lies near a minima in the DOS[72], small shifts and/or broadening are not going to change $N(\varepsilon_F)$ much. However, in the mixed SDW films where disorder is much greater, we see a large increase in $N(\varepsilon_F)$. This difference is approximately equivalent to the change in $N(\varepsilon_F)$ for crystalline and amorphous Mo[56], which is isoelectronic to Cr. It should also be noted that there is an observed monotonic increase in electron-phonon coupling with decreasing Θ_D. This agrees with resistivity data on these samples[12], where we see an increase in the Bloch-Gruneisen pre-factor and thus λ_{tr} (the transport-derived electron-phonon coupling term[47]).

3.5 Conclusions

We have used our thin film calorimeters to measure the specific heat of magnetron sputtered Cr films. From the low temperature data, we were able to obtain information about the phonon and electronic density of states as well as the electron-phonon coupling. We see no observable difference in the density of states between ISDW and CSDW Cr films. However, disorder plays a strong role in the films, not only increasing the density of states through broadening but also increasing the electron-phonon coupling through phonon softening and additional screening from the increased $N(\varepsilon_F)$. This increase in the DOS is important to consider when discussing the mechanism by which disorder may increase the GMR of an Fe/Cr MML.

Chapter 4

Enhanced density of states in Fe/Cr multi-layers

4.1 Introduction

Over the course of the past twenty-plus years, magnetic multilayer (MML) structures have led to a diverse group of phenomena relating magnetic coupling to novel electronic behavior such as giant magnetoresistance (GMR), tunneling magnetoresistance (TMR), and spintronics. The Fe/Cr MMLs first observed by Grunberg, et al.[49] are perhaps the most well-studied of these systems due to the range of behavior influenced by chromium's complex antiferromagnetic behavior. The standard quantum interference model used to explain MMLs with a host of different types of spacer layers depends strongly on the electronic DOS at the interface and spanning vectors within the Fermi surface of the material[16, 108]; however, the spin-density wave (SDW) responsible for Cr's antiferromagnetic behavior is itself a result of a spanning vector nesting portions of the electron-like and hole-like portions of the Fermi surface.

In addition to effects of the Fermi surface, the interfaces themselves play a crucial role in determining the coupling strength. Microscopic models have shown how an enhanced density of states at the interface can increase the spin-dependent scattering in GMR structures[117]. Furthermore, disorder at the interface in sputtered films has been shown to increase the spin-dependent scattering in Fe/Cr MMLs and suggested to increase GMR[27, 29], born out by theoretical calculations as well[77]. However, there are conflicting results on the role of alloying at the interface in these disordered multi-layer films[17, 77, 92].

Angle resolved photoemission spectroscopy (ARPES) results on a trilayer wedge MML showed experimentally the quantum well state and correlated this to the periodic fluctuations seen in surface magneto-optic Kerr effect (SMOKE) measurements[60]; however, these are inherently surface-sensitive techniques that require near-perfect interfaces and do not explain enhancements in the coupling or changes in the DOS as a result of interfacial disordering or alloying. Low temperature heat capacity offers a complementary look at the electronic DOS in these MMLs since it probes the DOS at the Fermi energy of the ensemble average, which means it takes into accounts contributions of the interface and the bulk layers themselves, both of which are important to GMR.
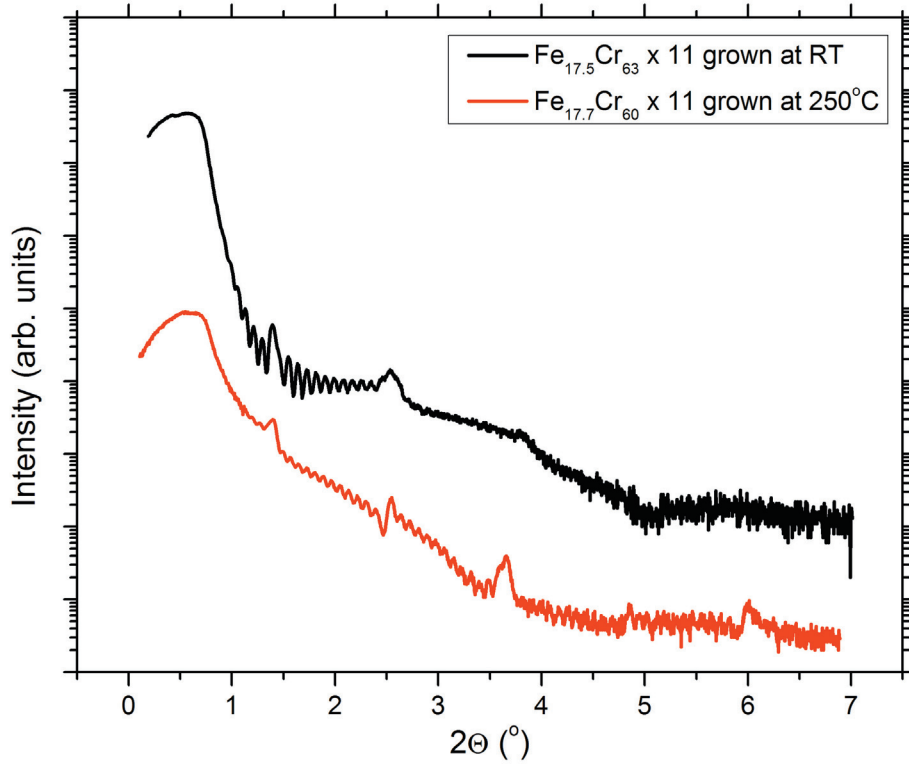
Figure 4.1: A comparison of low-angle X-ray diffraction data for a film grown at (a) room temperature to one grown at (b) 250°C. Note how the film grown at elevated temperature preserves the superlattice peaks out to higher order, indicating less disorder at the interface.

Previous calorimetry data has shown a significant enhancement in the electronic DOS of an Fe/Cr MML showing large GMR[97]. However, it was also established that this increase in DOS at the Fermi energy did not change with applied magnetic field. This work also exhibited a large softening of phonons relative to the bulk (indicated by a decrease in the Debye temperature, Θ_D), often an indication of disorder. Further work on Cr films showed how disorder can have a strong effect on both the AFM state [13] and DOS of sputtered Cr films[22]. The latter also examined the effect of Θ_D on γ through electron-phonon coupling-induced enhancements of the DOS ($\gamma \propto N(\epsilon_F)(1 + \lambda)$). With all of these outstanding questions as to the precise origin of the observed enhancement and its possible relationship to the GMR of the films, a more careful study was warranted. Due to the small mass of the thin film structure, traditional calorimetry techniques have too large an addenda to be applicable. Instead, we use a micromachined, silicon-nitride-based calorimeter with a small addenda to probe the thermodynamic properties of this thin film system[30].

4.2 Experimental Details

The original study of the enhancement in γ was on a single multilayer sputtered at the optimal conditions for maximum GMR according to Cyrille et al[27]. In order to examine the correlation of the DOS with GMR behavior, we deposited a series of multilayer films with varying Cr thicknesses with a fixed Fe layer thickness at $\sim$18Å. In addition, one sample was sputtered with roughly half the thicknesses of Fe and Cr layers in order to double the number of interfaces without changing the ratio of Fe to Cr. These multilayers were all grown onto a 40Å Cr seed layer and capped with 40Å Cr. The microcalorimeters are optimized for 2000Å films[98], so the total thickness of each multilayer sample was held constant. All Fe/Cr MML samples were sputtered via DC magnetron sputtering in a chamber with a base pressure less than 1×10^{-7} mTorr. All but one of these samples was sputtered at 1.5mTorr and at room temperature. The final sample was sputtered at a lower pressure (1mTorr) and elevated temperature (250°C) in order to reduce the amount of interfacial alloying, confirmed through low-angle x-ray diffraction (XRD) (Figure 4.1). This sample was also sputtered on a unique microcalorimeter where an ion beam-assisted MgO film was first deposited to provide a biaxially-oriented substrate for the Fe/Cr multilayer, maximizing film crystallinity[23] and resulting in (001)-textured growth (but not epitaxy). All other films were found to be polycrystalline via XRD. In addition to the MMLs, two "bulk" films of Fe and Cr were also grown as reference samples, again with Cr seed and capping layers.

In addition to XRD, the samples were characterized through magnetization and magnetoresistance measurements in a Quantum Design SQUID MPMS®. Profilometry measurements were made on several films using a KLA Tencor Alpha-Step IQ® Profilometer to ensure accurate determination of the amount of material on each device.

The heat capacity was measured from 2-300K using the semi-adiabatic relaxation method[30]. The contribution of the membrane, heater, thermometers, and the thermal conduction layer was separately measured and then subtracted from the total heat capacity. The contributions from the Cr seed and capping layers were also subtracted from all the films. The specific heat is taken to be per average atom based on the bulk densities of Fe and Cr, though it should be noted that the molar density of Fe (0.1410 mol/cm^3) and Cr (0.1383 mol/cm^3) are similar to within the $\sim$ 2% error in our technique[98].

4.3 Results

4.3.1 Magnetization and GMR measurements

The coupling in our multilayers was determined by looking at the "squareness" of the magnetization (M-H) loop (M_R/M_S where M_R is the remnant moment at zero field and M_S is the saturation magnetization at high field). A small M_R/M_S value implies a strong antiferromagnetic coupling, while a perfect ferromagnet would have a "squareness" of 1. M_R/M_S has been used previously to model the fraction of sample that is antiferromagnetically coupled, particularly in roughened, sputtered multilayers[114]. The "squareness" of our MML samples are plotted in Figure 4.2a as a function of Cr spacer thickness - note that after the first dip (corresponding to the most strongly antiferromagnetically-coupled
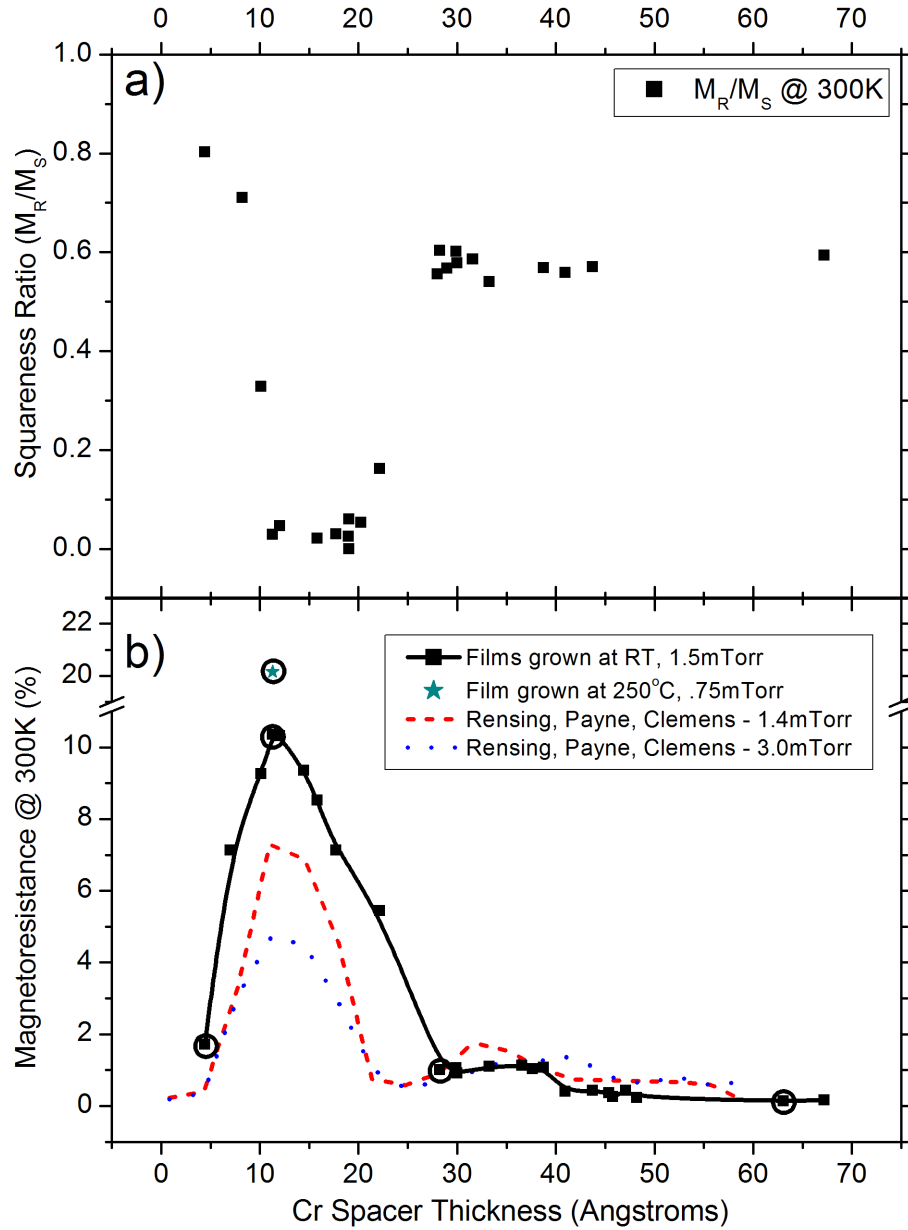
Figure 4.2: (a) The "squareness" of the magnetization (M-H) loop, M_R/M_S, and (b) magnetoresistance (MR) at 300K as a function of Cr layer thickness for a wide variety of MMLs. Data for this work is shown in symbols, with a solid line to guide the eye. Dashed and dotted lines are literature data[95]. An M_R/M_S value of 1 corresponds to a perfect ferromagnet, and 0 implies 100% of the sample is antiferromagnetically coupled. We observe a decaying MR magnitude and small second oscillation, consistent with previous measurements of polycrystalline films[95]. Samples used for specific heat measurements are circled.
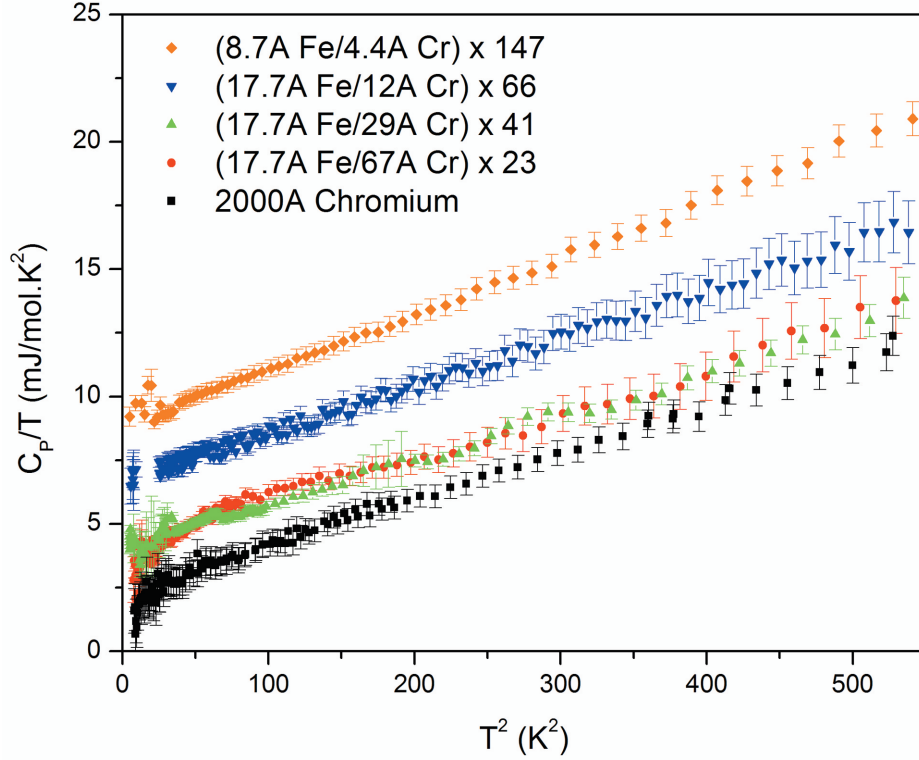
Figure 4.3: Low temperature specific heat data plotted as C_P/T vs. T^2 for a number of thin film multi-layers nominally 2000Å thick. The data was taken using the semi-adiabatic relaxation method on our microcalorimeters.

samples) we see a flattening at approximately 0.6. This is consistent with the literature where disorder in sputtered MMLs is known to result in a fraction of the film remaining ferromagnetically coupled for all thicknesses[114]. Complementary magnetoresistive measurements were taken at both 4K and 300K for a number of films. We show the 300K data to compare to previously measured polycrystalline sputtered films (Figure 4.2b); here we again see behavior consistent with earlier work[95].

4.3.2   Specific heat measurements

Though the specific heat was calculated for the MMLs up to room temperature, of primary interest is the low-temperature data shown in Figure 4.3. The data is plotted as C_P/T vs. T^2 because the specific heat of metals $C_P \approx \gamma T + \beta T^3$ at temperatures $T \ll \Theta_D$ where γ is the Sommerfeld coefficient (proportional to the electronic DOS) and β represents the Debye contribution from phonons (inversely proportional to Θ_D^3). We've included the specific heat data of a Cr film grown at 0.75 mTorr at room temperature as a reference. It should be noted that we've omitted from the metallic C_P model a contribution due to spin-waves in a ferromagnet, i.e. $C_{mag} = \alpha T^{3/2}$, because it is less than our experimental

resolution[83, 98].

4.4 Discussion

The data in Figure 4.3 are roughly parallel, showing that the phonons in all these multilayer systems exhibit approximately the same phonon heat capacity, regardless of the amount of chromium and iron in each film. This is borne out in the inset to Figure 4.4, which shows a nearly flat distribution of Debye temperatures for the films. This is somewhat surprising given the drastically different Debye temperatures of bulk iron and chromium (470K and 585K, respectively[52], but it is similar to what we saw in examining the heat capacity of thin films of iron and chromium previously[97]. One key difference between this result and the previous work on Fe/Cr MMLs is that we see substantially less softening of the phonons, even in the "bulk" Fe and Cr films (compare the current measurements' $\Theta_D(\text{Fe}) = 496 \pm 15$K and $\Theta_D(\text{Cr}) = 460 \pm 15$K to the previous measurements' $\Theta_D(\text{Fe}) = \Theta_D(\text{Cr}) = 415 \pm 13$K), which implies less disorder within the layers themselves. The inset to Figure 4.4 shows almost all films exhibit a Θ_D similar to the bulk value for Fe and a value comparable to what was seen in the polycrystalline Cr films under similar growth conditions previously (shown in Figure4.4 as the 100% Cr sample with a $\Theta_D = 460 \pm 15$K)[22]. The one outlier in the inset to Figure 4.4 is the film with the largest number of interfaces. This suggests that the film is more disordered than the other films, again suggestive of a larger fraction of the film alloyed.

Though the phonon contribution of all the films may be similar, Figure 4.3 shows clearly an increasing trend in the Sommerfeld coefficient γ that is proportional to the electronic DOS. Figure 4.4 shows that this enhancement goes well beyond a simple average of the Fe/Cr values. In this figure, we've drawn a line from measured "bulk" 2000Å thin films of Fe and Cr values of γ signifying the expected average value. The inset shows the difference of the measured γ values and this average.

The first point of interest regarding this enhancement is that though the films exhibit drastically different GMR values, the enhanced γ values do not correlate to these differences. However, γ does depend strongly and monotonically on the number of interfaces, signifying that it is related to an interfacial effect. In order to examine the effect of this interface, we look at two extreme cases. The first sample, Fe(8.9Å)/Cr(3.9Å), was grown at nominally the same ratio of Fe:Cr as the maximum GMR sample, Fe(17.9Å)/Cr(11.3Å), but each layer was cut in half, thus doubling the number of interfaces. This film shows a much reduced GMR, as indicated in Figure 4.2b. In Figure 4.4, we see that this Fe(8.9Å)/Cr(3.9Å) MML exhibits the greatest enhancement. It also shows a slightly greater softening of the phonons, as expected for a more disordered system. In contrast, the Fe(17.9Å)/Cr(11.3Å) MML grown at elevated temperature and exhibiting stronger order shows a sharply reduced γ much closer to the value expected for a linear combination of Fe and Cr. This strongly suggests that the enhancement in γ is simply an Fe-Cr alloy with a large γ.

The average intermetallic thickness of an Fe/Cr bi-layer can be as little as 2Å on an atomically smooth substrate[92], with 4-7Å more typical for a sputtered Fe/Cr MML[27]. By fitting the excess γ to a line proportional to N, the number of bilayers in the films, we can estimate what the contribution of the alloy would need to be to yield the large observed
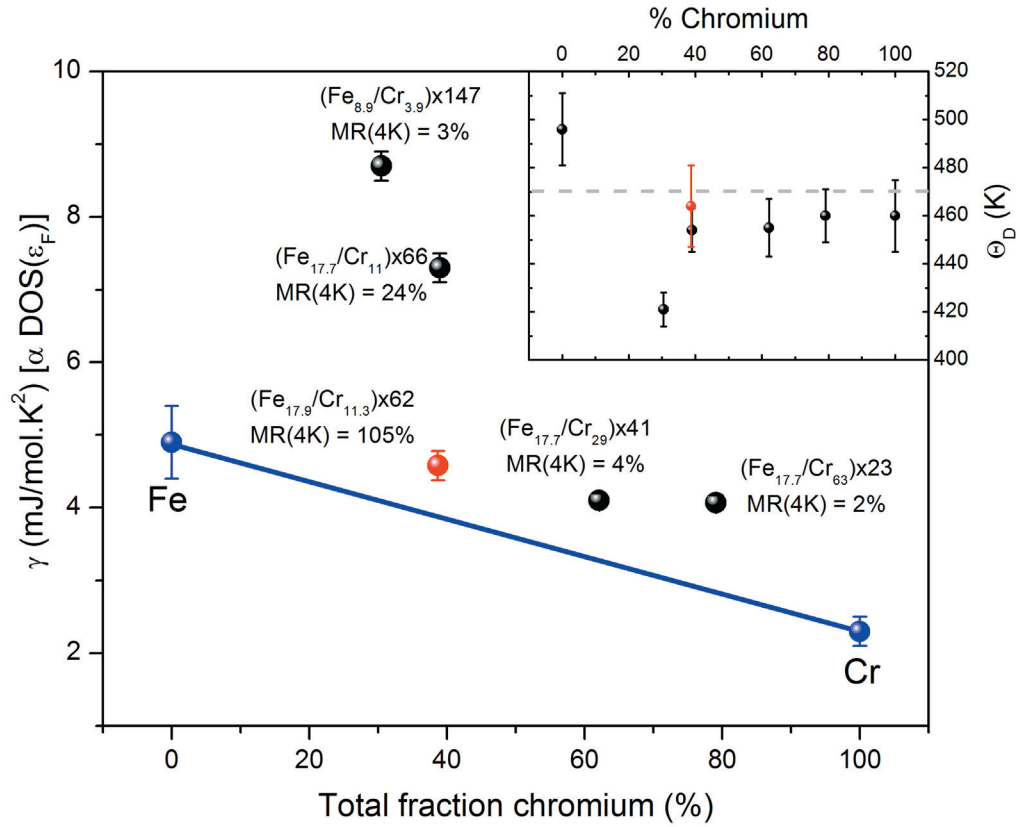
Figure 4.4: Sommerfeld coefficient γ and Debye temperature Θ_D (inset) vs. percentage chromium for a number of Fe/Cr multilayer films and for both Fe and Cr films grown under similar conditions. Each film is labeled with the thickness of the respective Fe and Cr layers and the number of repetitions of the bilayer. The blue line represents the value of γ expected for an average of Fe and Cr based on thin film measurements (though thin film Fe matches bulk values, there is a small enhancement in γ for thin film Cr[22]). The dotted gray line on the inset is the bulk value for iron. The red data points represent the film grown at elevated temperature on our IBAD MgO calorimeter and show stronger ordering and less interfacial disorder. All other data points represent films grown at room temperature.

enhancement. This slope is proportional to $t_{alloy}/1920\text{Å} \times (2\gamma_{alloy} - \gamma_{Cr} - \gamma_{Fe})$[a]. If we take the intermetallic thickness to be 5Å, the alloy would need to have a Sommerfeld coefficient $\gamma \approx 14$ J/mol/K^2. This is well within the realm seen in bulk heat capacity measurements of Fe-Cr alloys (3-26.8mJ/mol/K^2)[52]. Transmission electron microscopy (TEM) measurements suggest that the sample exhibiting the largest enhancement, Fe(8.9Å)/Cr(3.9Å), is predominantly comprised of Fe and an interfacial alloy, consistent with this picture. Thus, we believe that all enhancement of the density of states is due to the formation of an interfacial alloy.

While it is theorized that an interfacial alloy should enhance the GMR behavior[27], our own GMR measurements do not bear this out. Comparing the two samples with the maximum GMR (MMLs with $t_{Cr} = 11$Å grown at room temperature and 250°C), we see a large increase in GMR behavior for the film that has the lesser amount of interfacial alloying. However, this does does not mean that the interface does not play a key role in the GMR behavior. Building off the theoretical model of Zahn, et al., we suggest instead that the spin-dependent scattering at the interface is more dependent on the preservation of long-range order through the multi-layer structure (and thus enhancement in GMR due to resonant scattering of the quantum well structure) than the local DOS at the interface.

4.5   Conclusions

A series of Fe/Cr multilayer films of various Cr thicknesses were sputtered at room temperature. The films were characterized through magnetometry, magnetoresistance, X-ray diffraction, and TEM. Using relaxation microcalorimetry, an enhanced electronic DOS was measured for all the films. We've shown that this correlates not to the GMR but instead to the formation of an alloy at the interface. Because the largest GMR observed was for the film with the least amount of interfacial alloying, this indicates that the enhanced DOS at the interface due to long-range quantum well scattering is a stronger effect on the spin-dependent scattering than a local enhancement due to the formation of an alloy.

---

[a]1920Å is the thickness of the multilayer stack minus the Cr capping and seed layers

Chapter 5

Calorimetry of epitaxial thin films

5.1 Introduction

Calorimetry is a useful technique for observing a host of physical phenomena from the thermodynamics of a phase transition or a novel two-state system to magnons and spin density waves or the symmetry of high-Tc superconductors. As thin film technology has emerged as a way to manipulate materials on the microscopic scale, producing novel and often useful properties, it's become even more crucial to understand the way in which these novel properties emerge. However, traditional bulk calorimetric techniques have far too large an addenda to be used on thin films[107].

Over the past 15 years, there has been an emergence of novel "thin film" calorimeters fabricated with MEMS processes[4, 30, 43, 53, 58, 75, 101, 118]. These microcalorimeters use a thin membrane in order to reduce the background addenda and thermal link to an appropriate level for thin films. A common technique is to suspend the sample of interest on a thin membrane (most commonly amorphous silicon nitride, or a-SiN$_x$), which acts both as support and a weak thermal link to the sample stage. While the low thermal conductivity of the membrane provides for good thermal isolation, its amorphous structure does not provide a platform to grow high-quality, ordered thin film structures. Thus far, the calorimeters have primarily been used for measuring small bulk samples ($< 100\mu$g) and amorphous or polycrystalline films. However, this excludes many of the novel thin film systems one would be interested in studying such as dilute magnetic semiconductors or high-T_C superconductors.

To overcome this obstacle, we turn to the high-T_C superconductivity community for an answer. They have been using ion beam assisted deposition (IBAD) to grow high quality YBa$_2$Cu$_3$O$_{7-\delta}$ (YBCO) films onto long metallic tapes as way of scaling up ordered high-T_C superconductors for industrial applications[8, 48]. We used IBAD to grow biaxially-oriented MgO onto our a-SiN$_x$-based microcalorimeters, providing a template for epitaxial thin films. An Fe-Rh film epitaxially grown onto this device has been characterized and measured as a proof of functionality.

5.2 Experimental setup

5.2.1 Calorimeter fabrication

To create these microcalorimeters, we start from a 100-oriented double-polished Si wafer. On this, we deposit via chemical vapor deposition (CVD) a high-temperature "wet" (steam + O_2) silicon oxide, yielding a smooth buffer layer of 300nm; this oxide layer reduces capacitive links between thermometers and heaters. A 200nm low-stress (off-stoichiometry) silicon nitride layer is then deposited via low-pressure CVD (LPCVD) to provide the sample platform and act as our weakly thermally conductive link, as described above. We then use DC magnetron sputtering Pt to deposit electrical leads, thermometers, and the sample heater. The Si is then etched away in the central area, leaving a Si frame around the outside and a thin a-SiN$_x$ membrane with heaters and thermometers in the center. The next step in processing of our devices is the sputtering of a-Nb$_x$Si$_{1-x}$ ($x \approx 0.1$) for use as sensitive low-temperature thermometers. A more detailed description of most of this processing technique may be found in earlier work[30, 94].

5.2.2 IBAD MgO growth

The IBAD MgO layer was deposited on the back side of the device (i.e. the side of the membrane opposite the thermometer and heaters). All depositions were conducted in a high vacuum chamber with base pressure better than 5×10^{-8} torr. A 5nm nucleation layer of polycrystalline Si_3N_4 was first deposited on the surface via electron beam deposition at room temperature. The IBAD MgO layer was then deposited with concurrent 750eV Ar$^+$ and MgO fluences. A two-grid collimated Kaufman ion source at an incidence angle of $45°$ relative to the substrate normal provided the Ar$^+$ ion flux. The ion-to-atom ratio was kept constant at ≈ 0.8. Deposition was monitored throughout the process in situ using RHEED. After the 10nm IBAD MgO layer was deposited, the substrate temperature was raised to $300°$C, and a 15nm homo-epitaxial MgO layer was deposited via e-beam. This final layer acts to "heal" the surface and create a better-oriented substrate[8].

Because the MgO layer is grown on the backside of the device, the silicon frame acts to shadow a small fraction of the surface from the ion beam, resulting in a small fraction of the outer membrane area with a slightly thicker polycrystalline MgO region (a 150μm-wide band running the length of the window). However, because this is on the outer edge of the membrane adjacent to the Si frame, it does not affect areas of the membrane where any film will be deposited, nor does it significantly alter the thermal contours or behavior of our device[98].

5.2.3 Relaxation calorimetry

Once the film of interest (e.g. Fe$_{.49}$Rh$_{.51}$) has been deposited onto the IBAD MgO template, we thermally evaporate a 200nm Cu or Au film on top of it to create an isothermal sample region[98]. Because this sample area is weakly linked to the Si frame, we employ the semi-adiabatic relaxation method of calorimetry.

The relaxation technique consists first of applying a constant power P to the sample via the Pt heater, allowing it to reach a steady state. The equilibrium temperature difference

ΔT, measured by one of three thermometers in the central sample area (depending on temperature range), yields the value of the thermal conductance, $\kappa = P/\Delta T$, of the device. Once obtaining κ, we turn off the power to the system and monitor the temperature decay. In the limit $\Delta T \ll T_0$, this decay is exponential with a single time constant, τ, assuming a good thermal link between the sample and the thermometers, with $\tau = C/\kappa$ where C is the total heat capacity. This heat capacity C includes that of the sample and addenda (membrane, thermometers, and heater). The addenda is separately measured (without sample) and subtracted to obtain the heat capacity of the sample. Further description of our methodology as well as determination of membrane and lead contributions and systematic absolute errors is available elsewhere[30, 98].

5.3 Results

After fabricating a number of these IBAD MgO calorimeters, we began the process of analyzing key parameters of the device design: 1) crystalline quality of the IBAD MgO template, 2) crystalline quality of a film grown on this template, 3) the contribution of the IBAD MgO layer to the addenda heat capacity, and 4) representative specific heat data of an epitaxial film grown on these devices.

5.3.1 X-ray diffraction data

In order to characterize the quality of the IBAD MgO layer, we used X-ray diffraction measurements at the Stanford Synchrotron Radiation Lightsource (SSRL), carried out at beamlines 7-2 and 10-2 with 12 keV X-ray radiation. All measurements were carried out on conventional substrates (a-SiO$_x$ on Si) to act as a surrogate for the devices because they have been shown to have comparable surface roughness to the membrane[93]. Structural characterization was performed by grazing incidence X-ray diffraction to reduce scattering from the substrate. We then performed reciprocal space maps in H-K around several lattice points in order to quantify the crystallinity of the IBAD MgO film (Figure 5.1). The off-center peaks in the H-K planes indicate a small out-of-plane tilt ($\lesssim 5°$) and strain in the MgO. Combining this data with the L scans, we see that the MgO is biaxially-textured, as desired, with a small tetragonal distortion along the beam in-plane[79], leading to two in-plane lattice constants, $a = 4.228$Å along (020) and $b = 4.202$Å along (200) (for reference, the ion beam was directed in the (202) direction during growth). The out-of-plane lattice constant matches the bulk value, $c = 4.212$Å.

We then sputtered Fe$_{.49}$Rh$_{.51}$ onto the IBAD MgO substrate and devices and onto an MgO substrate for comparison. Fe-Rh alloys form the CsCl structure at this composition[106] and undergo a metamagnetic antiferromagnetic-to-ferromagnetic phase transition that is very sensitive to structural disorder[78]. The Fe-Rh films grow (001) out-of-plane, but because the lattice constant is approximately $\sqrt{2}$ smaller, the films are rotated 45° in plane relative to the MgO. To characterize the ordering of the films grown on IBAD MgO, we measured out-of-plane X-ray diffraction along the (001) axis and in-plane diffraction at a 45° tilt to examine the (110) peaks. A $\theta - 2\theta$ scan at that tilt was used to obtain the location of the (110) peak and, thus, extract the lattice parameters for the films.
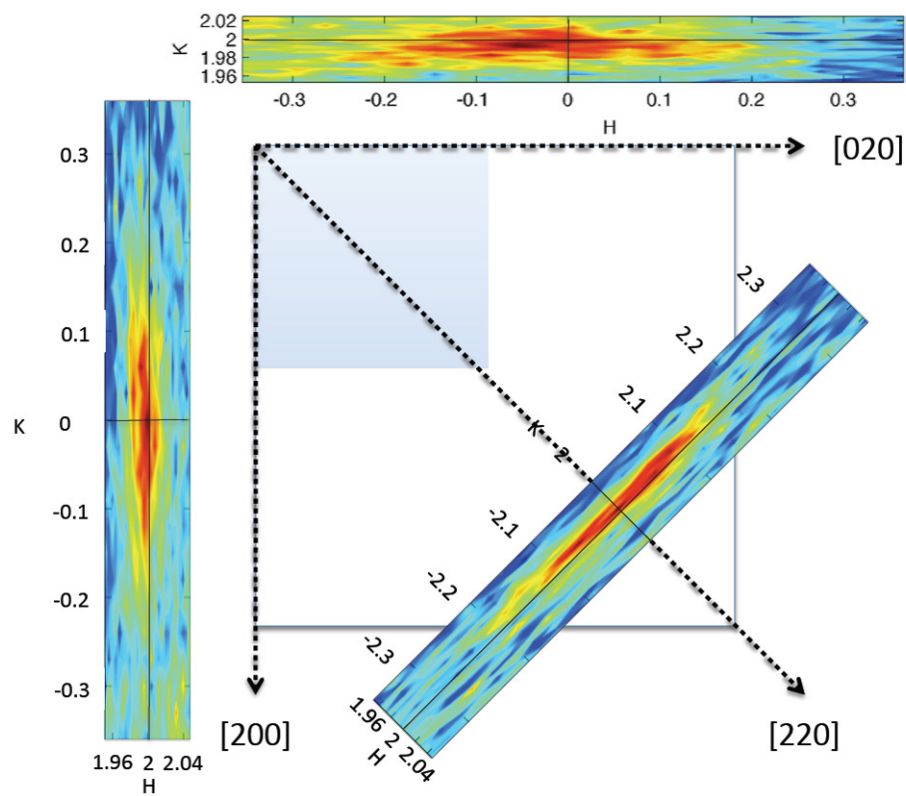
Figure 5.1: Reciprocal space map in H-K of the IBAD MgO films. The data was taken via X-ray diffraction measurements at the Stanford Synchrotron Radiation Lightsource.
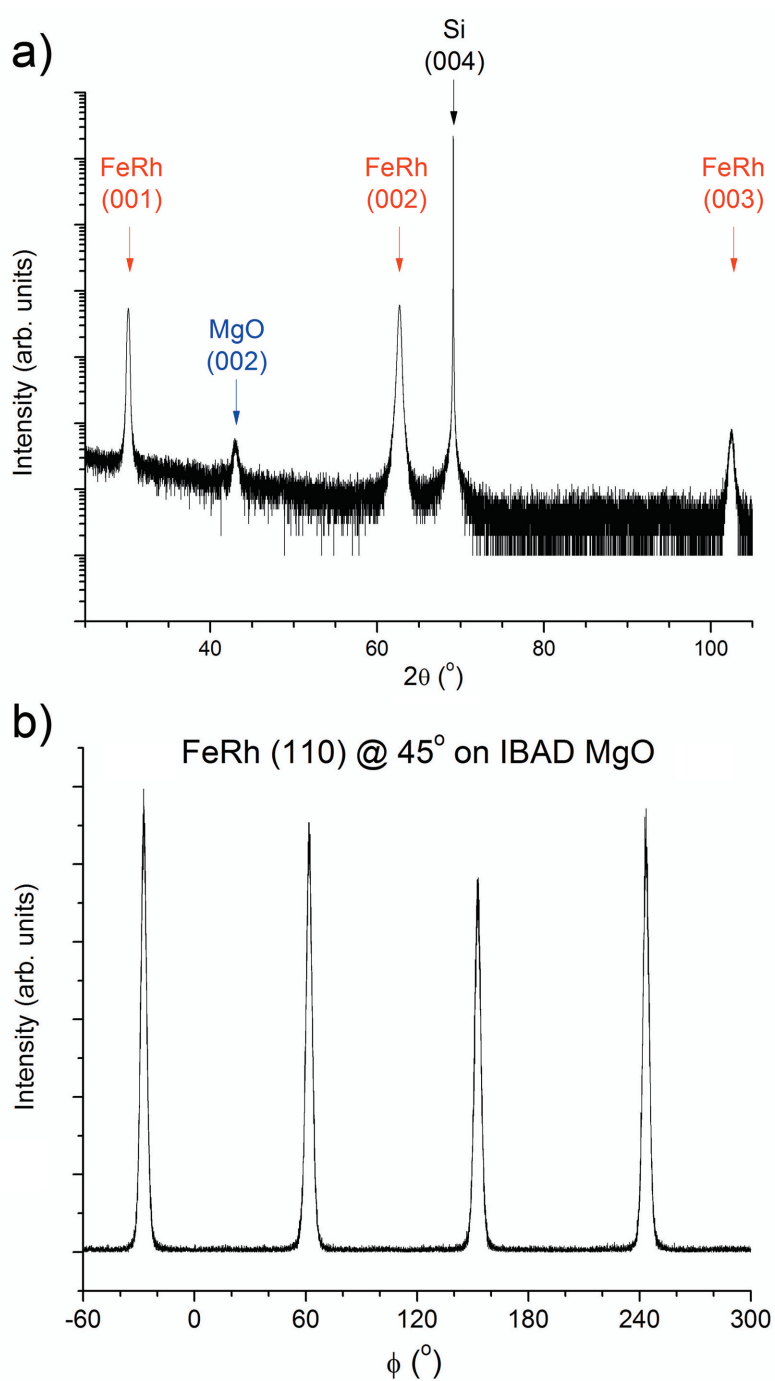
Figure 5.2: (a) Out-of-plane and (b) in-plane X-ray diffraction measurements of a 200nm $Fe_{.49}Rh_{.51}$ film grown on IBAD MgO. Note the four-fold in-plane symmetry indicating epitaxy.

Figure 5.2 shows the out-of-plane and in-plane X-ray diffraction data taken on the film grown on IBAD MgO. In-plane data shows the four-fold symmetry expected for an epitaxial film with the body-centered-cubic structure, while out-of-plane XRD shows shows the clear, highly-ordered CsCl superlattice peaks. The IBAD MgO substrate shows orthorhombic structure ($a \neq b \neq c$), which could lead to monoclinic ordering in the $Fe_{.49}Rh_{.51}$ film - however, within the resolution of the detector, the four (110) peaks were exactly 90° apart and showed no asymmetry, indicating a tetragonal structure ($a = b \neq c$).

The lattice constants for the films grown on the MgO and IBAD MgO films show a small difference in film structure - the films grown on IBAD MgO do not exhibit the compressive strain seen in those grown on MgO. This is due to the different in-plane lattice constant for IBAD MgO, as noted above. In the films grown on IBAD MgO, this change in strain leads to a more bulk-like behavior, evidenced by a lower critical temperature ($T_{crit} = 330K$, as compared to 380K for the film grown on MgO and $328 \pm 2K$ for a bulk crystal[99]) for the sharp first-order metamagnetic transition. The IBAD MgO thus forms a useful substrate.

5.3.2   Calorimetry data

We now characterize the effect of the IBAD MgO layer on our measurement technique. Figure 5.3b shows the additional heat capacity of the device. At high temperatures, there is a net ~ 700nJ/K increase from the device without the MgO layer, or only about 6.5% of the total addenda measurement. At low temperatures, the specific heat of the MgO layer falls off as T^3, much faster than the $C \propto T$ contribution of both the a-SiN$_x$ layer[94] and the metallic thermal conduction layer, so this fraction decreases at low temperature.

Figure 5.3 shows that the contribution of the IBAD MgO layer can be modeled very well by the bulk MgO. Though this contribution is small (as shown in Figure 5.3b), it could be further reduced by a factor of two by eliminating the MgO outside the sample area (we note that the fractional contribution from the MgO outside the sample area is only 24%[98]). Though it matches well to the bulk value at high temperature, the low temperature data (Figure 5.3a) indicates a softening of phonons with a much lower Debye temperature, $440 \pm 130K$ as compared to $743 \pm 8K$[11]. We suspect this has to do with either the strain in the film mentioned earlier or the bombarding process itself which is known to create damage and lower the Debye temperature in thin films[59].

Given this near-negligible heat capacity contribution of IBAD MgO to the device, we next measured the specific heat of an $Fe_{.49}Rh_{.51}$ film grown epitaxially onto an IBAD MgO microcalorimeter, shown in Figure 5.4. The data matches that of the bulk well. There is very good agreement with the results of Richardson et al. from 100K to 300K[99], and at low temperatures, the results of the Sommerfeld coefficient, $\gamma = 22 \pm 2\mu J/g/K^2$, is well within the range of data seen in the literature[66, 112] ($\gamma = 16 - 24\mu J/K^2$). However, we do observe a softening in the lattice, evidenced by a lower $\Theta_D = 340 \pm 13K$ as compared to $\Theta_D = 390 - 410K$. We attribute this difference to the increased mosaicity of the Fe-Rh film grown on the IBAD MgO as compared to the bulk, as evidenced by the larger FWHM of the XRD peaks.
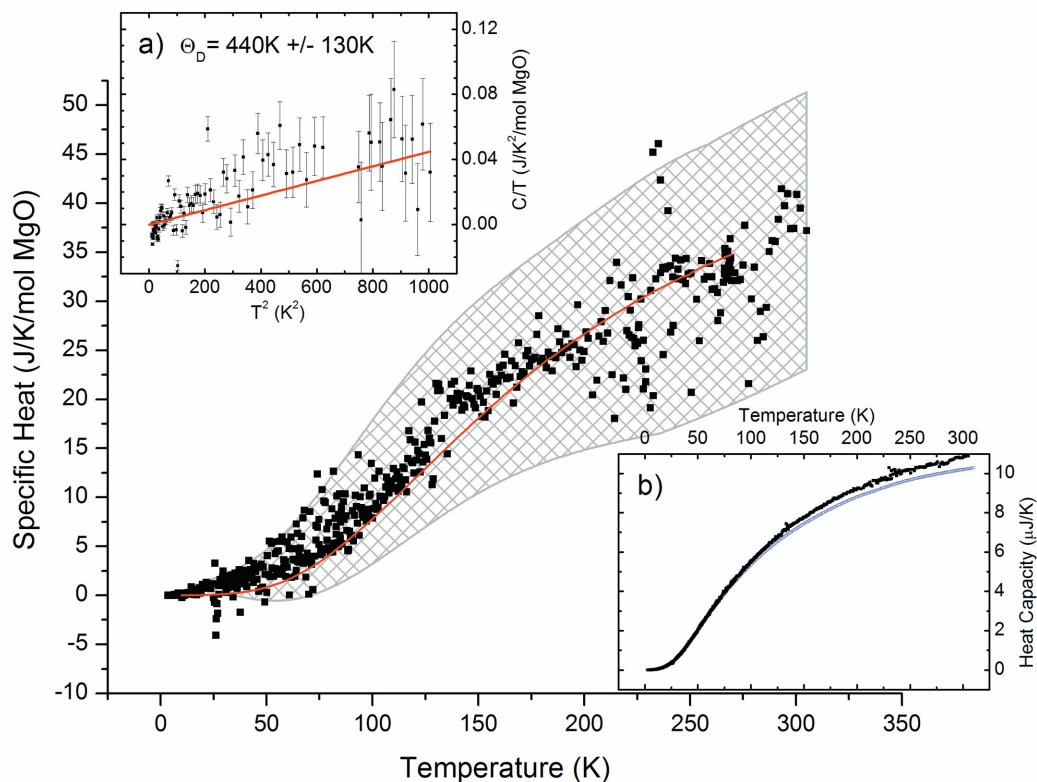
Figure 5.3: The black squares are the specific heat contribution of the IBAD MgO layer. Shading represents the average error. A representative error bar is shown at 300K. The large scatter in the data is due to the fact that the IBAD is a mere 6.5% of the total addenda, as indicated in inset b), where the total heat capacities are shown for a device with (black squares) and without (blue open circles) the IBAD layer. The red curve through the data is the value of bulk MgO[10]. Inset a) is the low temperature data shown as C/T vs. T^2, with the red line being a fit to the data yielding a Debye temperature of 440 ± 130K.
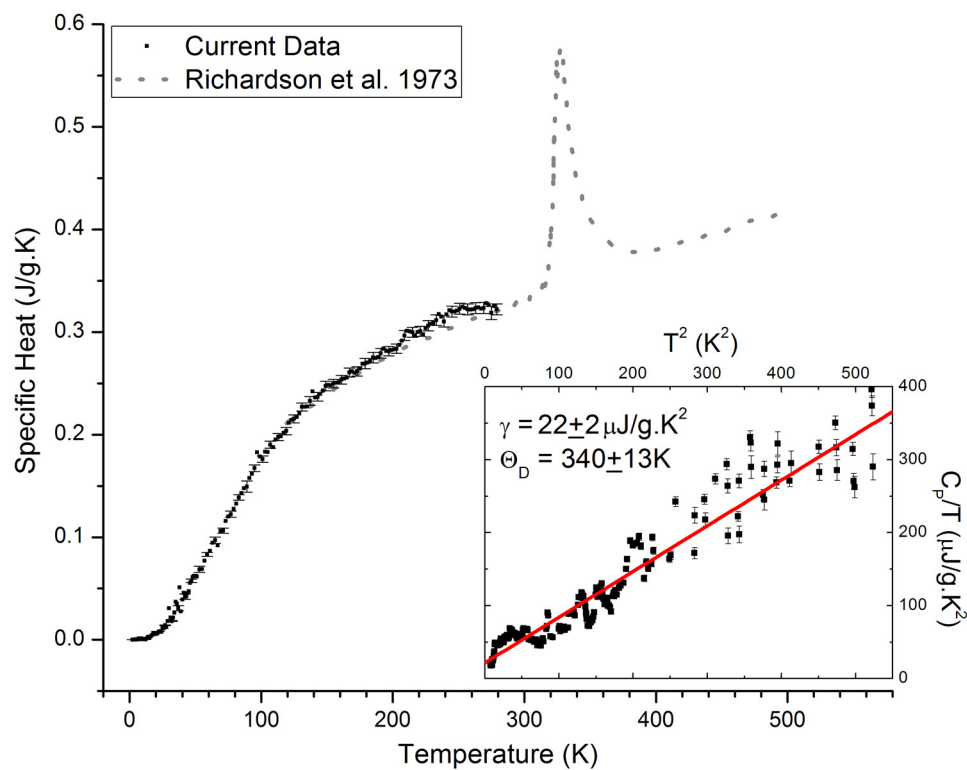
Figure 5.4: Specific heat data for an epitaxial FeRh film grown on an IBAD MgO calorimeter (black squares) compared with data for the bulk[99] (dashed gray line). The inset shows the low temperature data C/T v. T^2, as is characteristic for a metal. Drawn through the data is a linear fit wherein the intercept ($\gamma = 22 \pm 2 \mu J/g/K^2$) compares compare favorably to the values in the literature[66, 112]. The Debye temperature corresponds to a slight reduction, from 390-410K to $\Theta_D = 340 \pm 13$K.

5.4   Conclusions

In order to measure the specific heat of epitaxial thin films, we have used ion-beam-assisted deposition to grow a biaxially-oriented MgO substrate on the amorphous SiN_x membrane of our thin film calorimeters. X-ray diffraction confirmed the biaxial nature of the IBAD MgO substrate and the highly ordered epitaxial structure of the subsequent $Fe_{.49}Rh_{.51}$ film grown on that substrate. The heat capacity of this thin MgO layer compares well with the bulk and adds only a small ($\approx 6\%$) contribution to the addenda of our devices. We used these new calorimeters to measure the specific heat of an epitaxial $Fe_{.49}Rh_{.51}$ film and showed that it compares favorably to bulk sample values in the literature. The successful fabrication of these new devices offers a wealth of possibilities for new thermodynamic studies of high-quality nanostructures such as multiferroics, dilute magnetic semiconductors, high-Tc superconductors, and a range of other thin films that can be grown epitaxially onto an MgO substrate.

Chapter 6

Thermodynamic measurements of Fe-Rh alloys

6.1   Introduction

In the past few decades, we have undergone what many call an "information revolution", the next wave of economic and social growth beyond the industrial revolution. From a technological perspective, the driving forces behind much of this rapid advancement has been the continued developments in semiconductor electronics and complementary work in information storage dominated by magnetic recording. Much like Moore's Law drives the semiconductor industry for smaller and faster, so too does it push the media giants for denser data and rapid read/write mechanisms. However, as the bit size becomes smaller and smaller, traditional media begins to run into the superparamagnetic limit as the anisotropy energy becomes comparable to $k_B T$, leading to thermal instability of bits and/or the difficulty of writing bits in accessible magnetic fields.

Beyond simply better read/write head technology, denser storage also mandates more radical approaches such as perpendicular media and thermally-assisted magnetic recording (TAMR). One novel approach to TAMR involves an FePt/FeRh bilayer[110]. FePt is a highly anisotropic ferromagnet, making it useful for overcoming the superparamagnetic limit. However, this anistropy also means that it requires a lot of energy to magnetically write a bit. Equiatomic iron-rhodium alloys undergo an antiferromagnetic to ferromagnetic (AF>FM) transition at slightly elevated temperatures ($\approx 100\,^\circ$C). In its AFM state, the FeRh does not have much of an effect and the stability is provided by the highly-anisotropic FePt layer, while in its FM state it couples to the FePt via a spring exchange mechanism, helping to flip the bit for writing.

While the AF>FM transition shows clear technological application, there remain basic questions as to the driving force of this unusual transition. Early low-temperature specific heat measurements on binary and ternary alloys around the equiatomic FeRh composition showed a substantial reduction in the Sommerfeld coefficient γ (which is proportional to the electronic density of states (DOS)) for alloys with an antiferromagnetic ground state as opposed to those with a ferromagnetic ground state. Based on this data, Tu et al. suggested that it was this electronic entropy difference driving the transition[112], and first

principle calculations later agreed with the large ground state electronic DOS difference[64]. However, this model assumes no change in $N(\epsilon_F)$ (and therefore no change in γ) as a function of temperature, which contradicts what is seen in other antiferromagnetic materials with a spin density wave (SDW) where the gap in the Fermi surface decreases with increasing temperature[45, 85]. Two other models focus on magnetic fluctuations driving the transition. Gruner et al. evaluate FeRh in an extended Heisenberg picture, explaining the transition through the co-existence of two magnetic states of the Rh atom. Spin flips between the 0 and ± 1 state of the Rh atom cause a competition between the AFM phase (controlled by AFM Fe-Fe interactions) and the FM phase (connected to FM Fe-Rh interactions)[50]. This model yields a Schottky-like anomaly at ~ 200K in the FM state due to the two Rh states (either no moment or parallel to the local Fe moments). The second fluctuation model by Gu and Antropov focuses instead on a strong Fe-Rh interaction mediated by magnons[51] to drive the theory. It, too, predicts a peak in the heat capacity of the FM phase at moderate temperatures (~ 300K), here due to magnon excitations.

Though low-temperature specific heat measurements have been made on bulk alloys[66, 112] and high temperature measurements around the transition itself[99], to date no one has examined the moderate temperature range where the two-state anomaly in the proposed thermal fluctuation models is predicted to occur. We've used our ion-beam-assist-deposited (IBAD) MgO microcalorimeters[23] to measure the specific heat of two Fe-Rh alloys, one with an antiferromagnetic ground state ($Fe_{.49}Rh_{.51}$) and one with a ferromagnetic ground state ($Fe_{.52}Rh_{.48}$) in order to study these models. We've complemented this work with photoemission measurements above and below the transition to examine the change in electronic DOS at the transition. From the photoemission data, we find that there is no more than a 10% change in $N(\epsilon_F)$ at the transition and therefore less than a 10% change in electronic entropy and enthalpy. We further observe a two-state-like anomaly in specific heat at moderate temperatures, suggesting that the thermal fluctuation models are correct, although the error bars are too large to distinguish between these models.

6.2   Experimental details

Thermal relaxation calorimetry is a widely used technique for measuring heat capacity of small samples. In Bachmann's pioneering design, the sample is thermally and physically bound to a silicon bolometer consisting of heater, thermometer, and sample platform. Thin gold wires form a weak thermal link between this bolometer and a frame which is strongly coupled to a sample block held at temperature T_0[9]. This is considered a semiadiabatic calorimeter because it is impossible to completely thermally isolate the sample due to the need for electrical leads and bolometer support structure (the gold wires). By using thin gold wires, the thermal conductance between the bolometer and the environment is less but not infinitely less than that between the sample and the bolometer.

Our microcalorimeters modify this design by using an amorphous silicon nitride membrane to support and isolate the sample from the silicon frame. Amorphous NbSi and Pt thermometers are located on the silicon frame and sample area and connected to a differential bridge to measure ΔT, and they are connected by platinum leads.

Since its inception, the basic design of our microcalorimeter has not changed

significantly[30], though we have recently produced a nanocalorimeter in order to measure even thinner films ($\lesssim$ 30nm)[94]. In order to study epitaxial films, we have recently developed an IBAD MgO calorimeter wherein a biaxially-ordered MgO template is deposited in the sample area[23]. Because the transition in Fe-Rh alloys is so sensitive to disorder[a], and any broadening in the transition would likely obscure the two-state anomaly, we used this IBAD MgO calorimeter for both Fe-Rh alloy films.

The Fe-Rh alloy films were grown by Stephanie Moyerman and Eric Fullerton using magnetron sputtering. The $Fe_{.49}Rh_{.51}$ film was deposited from an equiatomic FeRh target, while the ferromagnetic film was co-sputtered from this Fe-Rh target and a partially masked Fe target (to decrease the Fe rate substantially). Both films were grown at the elevated temperature of 300°C before being annealed for 2 hours at 600°C. The composition of the films was determined via Rutherford back-scattering measurements on adjacent substrates; this is also how we determined the total amount of material on the devices. The films' epitaxy was confirmed via four-circle X-ray diffraction for samples grown on IBAD MgO and neighboring MgO substrates. The Fe-Rh films grow (001) out-of-plane, but because the lattice constant is approximately $\sqrt{2}$ smaller, the films are rotated 45° in plane relative to the MgO. We characterized the in-plane order by setting the polar angle $\psi = 45°$ and measuring the (110) peaks. Data for the $Fe_{.49}Rh_{.51}$ film is shown in Figure 5.2. The film grown on sapphire is polycrystalline, exhibiting grains with both (111) and (012) out-of-plane orientation.

Photoemission measurements were carried out at the National Institute for Materials Science (NIMS) endstation BL15XU at SPring-8. $Fe_{.49}Rh_{.51}$ films grown on IBAD MgO(001), MgO(001), and Al_2O_3(0001) substrates were measured both at room temperature and 360K. Magnetization measurements as a function of temperature were made on a Quantum Design SQUID MPMS$^\circledR$ while applying a 0.2T field in order to sufficiently magnetically saturate the sample without lowering the critical temperature significantly ($\lesssim$ 2K[78]).

6.3   Results

Figure 6.1 shows magnetization data and its temperature derivative for 200nm $Fe_{.49}Rh_{.51}$ films grown on IBAD MgO(001), MgO(001), and Al_2O_3(0001). We define $T_{AF>FM}$ as the point of inflection seen clearly in Figures 6.1d and e. Note the 35-40 degree decrease in $T_{AF>FM}$ under the 8T applied field (Figure 6.1a); this is less than the 60K change observed previously for films grown on MgO[78]. We also see an asymmetry between warming (AF>FM) and cooling (FM>AF) in the film grown on MgO which was not observed previously, evidenced by the different slope at the right edge of Figure 6.1e. Of primary interest for the photoemission data is the location of $T_{AF>FM}$ without an applied field - it lies above 360K for the film grown on MgO, below 360K for the film grown on IBAD MgO, and near 360K for the film grown on sapphire. We do not show a cooling portion of the 0.2T hysteresis loop in Figure 6.1b because the maximum measurement temperature, 400K, is below the $T_{AF>FM}$ for this film.

---

[a]Personal communication with Eric Fullerton
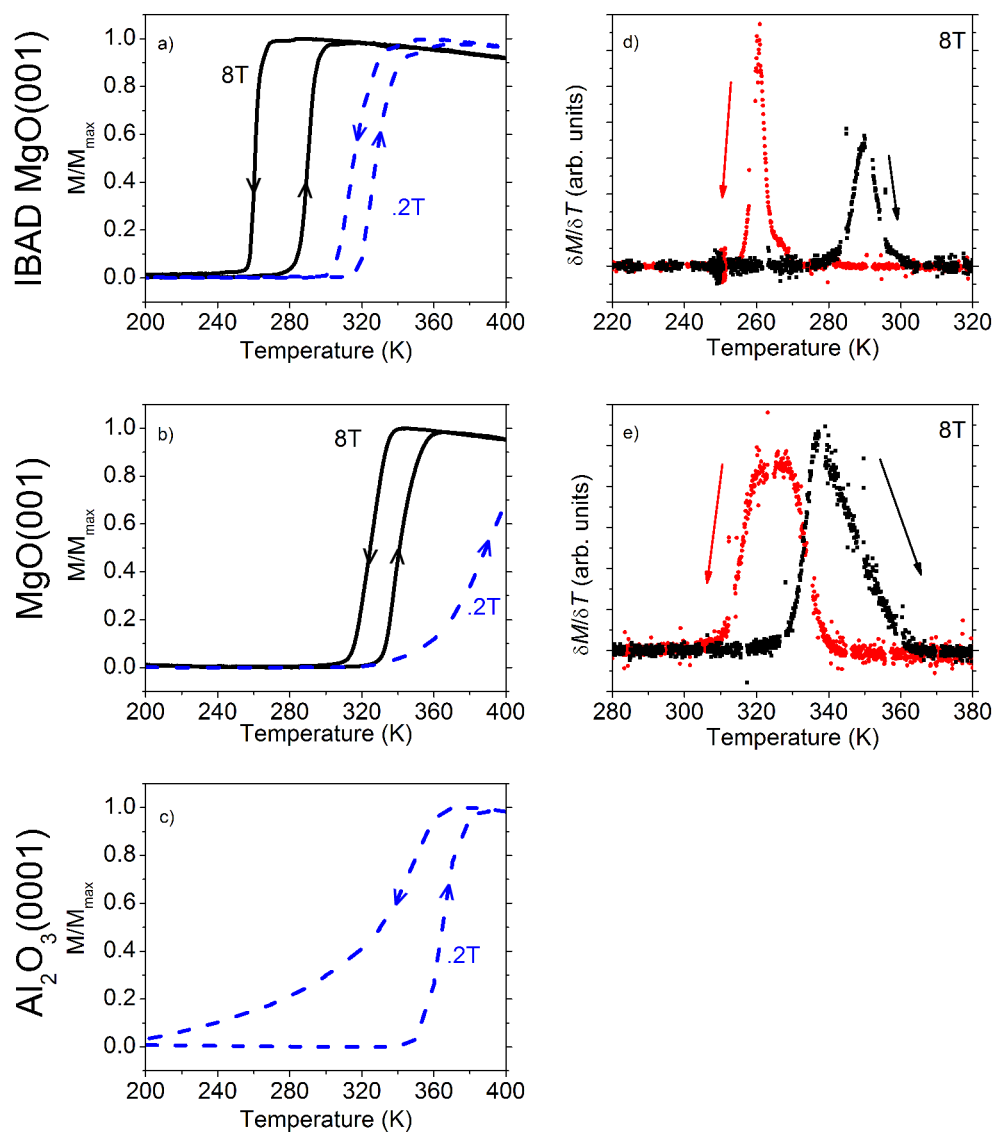
Figure 6.1: Magnetization data at 8T (black solid lines) and 0.2T (blue dashed lines) as a function of temperature for $Fe_{.49}Rh_{.51}$ films grown on IBAD MgO(001) (a), MgO(001) (b), and Al_2O_3(0001) (c). (d) and (e) are the derivative with respect to temperature of the 8T data in (a) and (b), respectively, with the black (red) lines representing the warming (cooling) curves.
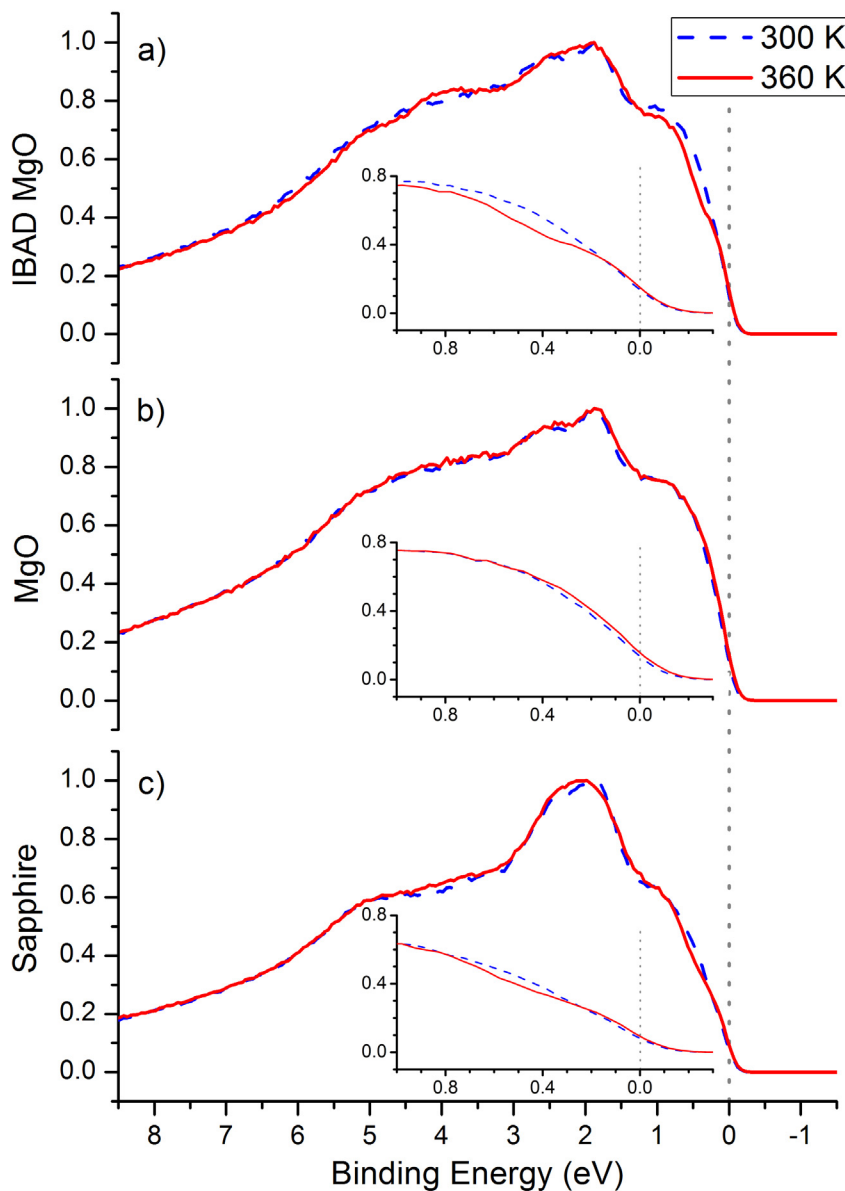
Figure 6.2: Photoemission data at the edge of the valence band for 200nm Fe$_{.49}$Rh$_{.51}$ films grown on a) IBAD MgO(001), b) MgO(001), and c) Al$_2$O$_3$(0001) ($0 = \epsilon_F$). The blue dashed lines are room temperature data, and the red solid lines are taken at 360K. The three insets show the valence band edge to highlight the difference between 300K and 360K in a) and c) in the feature at ~ 0.6eV.

Figure 6.2 shows photoemission data taken on $Fe_{.49}Rh_{.51}$ films grown on (a) IBAD MgO(001), (b) MgO(001), and (c) Al_2O_3(0001) substrates. One can see from Figure 6.2a that there is a noticeable change in the Fe-Rh DOS from its AFM state to its FM state, as indicated in the $Fe_{.49}Rh_{.51}$ film grown on IBAD MgO. We observe very little change in the valence band of the film grown on MgO (Figure 6.2b) because the measurement temperature is below the film's $T_{AF>FM}$. Finally, we observe a small change in the film grown on sapphire (Figure 6.2c), but the degree of FM in the film is unclear based on the magnetization measurements; 360K is not high enough to fully pass through the AF>FM transition. The precise portions of the band affected by the AF>FM transition in Figure 6.2a are impossible to ascertain without a fully-developed numerical model, but we estimate that there is no more than a 10% shift in $N(\epsilon_F)$ through the AF>FM transition, which is consistent with recent ARPES results[74].

Figure 6.3 depicts the specific heat data for the ferromagnetic ($Fe_{.52}Rh_{.48}$) and antiferromagnetic ($Fe_{.49}Rh_{.51}$) Fe-Rh films grown on our IBAD MgO microcalorimeters. Notice that the AFM alloy matches the data from the literature. Note, too, that there is a noticeable (albeit small) excess heat capacity in the FM alloy at approximately 100K - this will be discussed in further detail in Section 6.4. The low temperature data in the inset to Figure 6.3 shows a marked difference between the two films. While the FM alloy exhibits a Debye temperature similar to that seen previously for Fe-Rh alloys near the equiatomic composition[66], the AFM alloy shows a marked softening from the bulk value of $390 - 410$K. We also see a slight decrease in the value of γ for the FM alloy, 8.3 ± 0.5mJ/mol/$K^2 = 53 \pm 3\mu$J/g/K^2, which is slightly smaller than the previously reported range of 59-66μJ/g/K^2[38, 112]. The value of γ for the AFM alloy is well within the range seen for AFM alloys near the equiatomic composition, with $\gamma = 3.5 \pm 0.4$mJ/mol/$K^2 = 22 \pm 2\mu$J/g/K^2 comparing favorably to the range of 10-32μJ/mol/K^2[38, 112].

6.4   Discussion

Magnetism data in Figure 6.1 shows some distinct differences between the films grown on the different substrates. Strain is known to play a large role in the magnetic behavior of the Fe-Rh alloy system - earlier work on thin films indicated that altering the substrate can significantly change how the AFM and FM phases nucleate around the AF>FM transition[78]. X-ray diffraction of the films grown on IBAD MgO and MgO substrates revealed a difference in lattice parameters between the two films. In the case of the IBAD MgO substrate, the film exhibited a compressive tetragonal distortion: $a = 3.005$Å and $c = 2.959$Å as compared to the bulk value of $c = 2.987$Å. In the case of the film grown on MgO, we see an elongation in c and compression of a: $a = 2.980$Å and $c = 3.004$Å. The $a = 2.980$Å is very close to the diagonal of the MgO lattice $a_{MgO}\sqrt{2} = 2.978$Å, meaning it is likely this film is not fully relaxed (for Poisson's ratio 0.30-0.32[90], we calculate a critical thickness of 2026-2062Å). Because the Fe-Rh film is pinned to the substrate, the $\sim 1\%$ δV that accompanies the first order transition must take place entirely in a δc. In the case of the film grown on IBAD MgO, a 1% expansion along c results in a nearly cubic structure, which is the ground state in the bulk. In the case of the film on MgO, it requires a further elongation along c which requires more energy. This is why not only does the film on IBAD
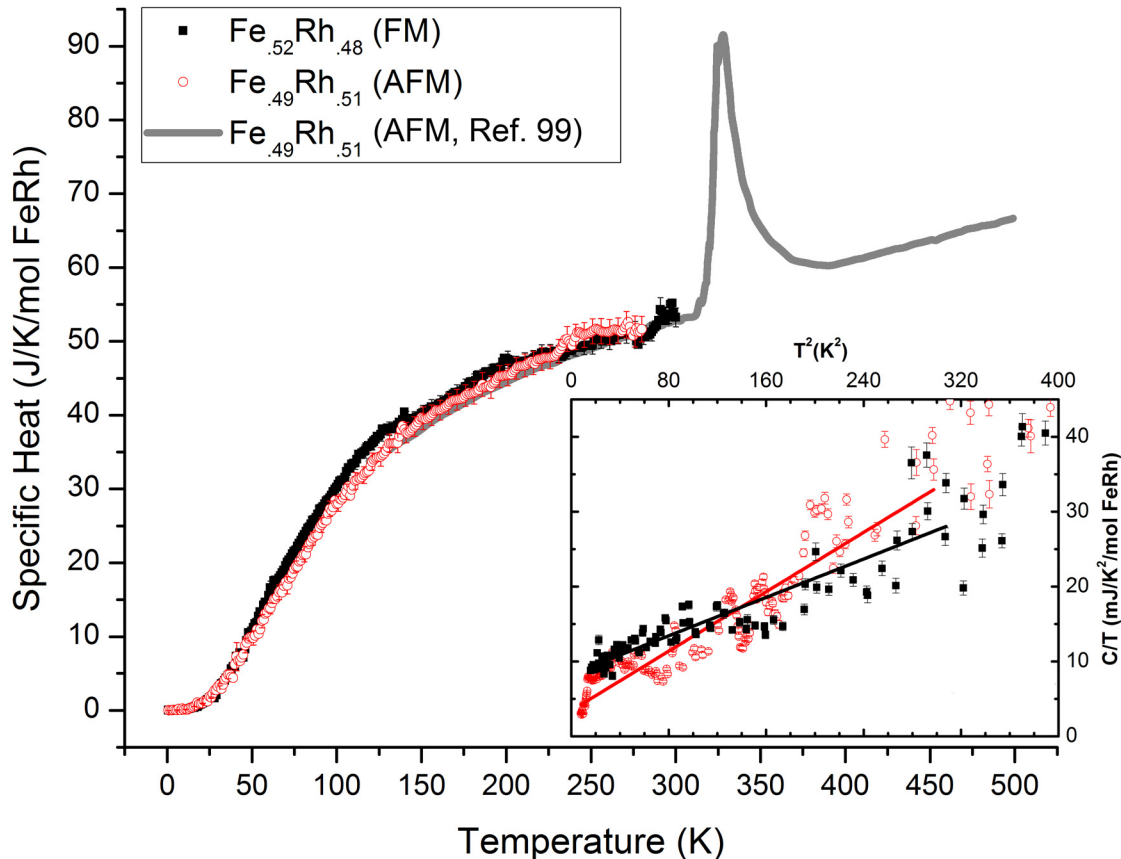
Figure 6.3: Specific heat data for $Fe_{.52}Rh_{.48}$ (filled black squares) and $Fe_{.49}Rh_{.51}$ (open red circles) overlaid with data on $Fe_{.49}Rh_{.51}$ from the literature from 100-500K (gray line)[99]. The inset shows the data for the two Fe-Rh alloys as a function of C/T v. T^2. The solid black line in the inset is a fit to the $Fe_{.52}Rh_{.48}$ (FM) data with $\gamma = 8.3 \pm 0.5\mathrm{mJ/mol/K^2}$ and $\Theta_D = 393 \pm 20$K. The solid red line in the inset is a fit to the $Fe_{.49}Rh_{.51}$ (AFM) data with $\gamma = 3.5 \pm 0.4\mathrm{mJ/mol/K^2}$ and $\Theta_D = 340 \pm 13$K.

MgO have a lower $T_{AF>FM}$, but it also has a sharper transition, as indicated by the narrow peaks in the derivative in Figure 6.1d.

The asymmetry between warming and cooling of the films reflects differences in the nucleation of the AF and FM domains, an ongoing area of research. In both the films grown on IBAD MgO and MgO we see a broadening of the transition region with a reduction of field from 8T to 0.2T - this is in contrast to what was previously observed[78]. This may be due to pinning effects in our films when cooling from the FM phase to the AFM phase. In the case of the IBAD MgO film, this may be a result of the slight increase in disorder of the biaxial template, though at high field we see a sharper transition as mentioned above. Preliminary analysis of Mossbauer spectra on this film shows an out-of-plane orientation of the Fe moments in the AFM phase, so it may be instead that this broadening is related to the demagnetization field and simply a consequence of applying the field in-plane. In the case of the film grown on sapphire film, the extremely broad FM>AF transition is particularly noticeable - such behavior was exhibited for polycrystalline films grown on SiO_2[84] as well as nanoparticles, where there is large disorder[63]. We attribute the breadth in this polycrystalline film to a pinned FM moment at the grain boundary preserving and stabilizing the FM phase. More careful study of the intrinsic mechanisms responsible for the nucleation of the two phases is warranted.

Preliminary analysis of the photoemission shows changes in the valence band spectra as well as dramatic changes with T of the Fe 2p states. We are in the process of doing density functional calculations to model the core level spectra and obtain values for the hopping strengths in order to analyze the photoemission data. However, the fact that the difference in the spectra above and below the transition is so small means that contrary to the theory first suggested by Kouvel et al., the electronic DOS difference between the two phases does not have enough entropy or enthalpy to account for the transition. This is consistent with previous work examining the dielectric function around $T_{AF>FM}$[18] and recently published ARPES results[74]. We suggest instead that the transition is likely activated by magnetic fluctuations, which are different for the FM and AFM states.

In the thermal fluctuation model put forth by Gruner et al., the predicted Schottky-like anomaly comes from a competition between the non-magnetic ground state of the Rh atom and the ferromagnetic alignment of the Rh moment, or in other words, a competition between the anistropic energy D_{Rh} responsible for $S_{Rh} = 0$ ground state and the exchange interaction J_{Fe-Rh}. This two-state system only occurs in the FM alloy because J_{Fe-Rh} cancels at the Rh site in the AFM state due to the anti-parallel alignment of the Fe spins. The additional entropy and enthalpy of this two-state system lowers the Gibbs free energy of the FM, finally matching that of the AFM phase at $T_{AF>FM}$, thus driving the transition. In this model the Schottky-like anomaly peaks at just above 200K - this would correspond to an energy splitting of about 3.3mRyd for a fixed $\Delta E(T)$.

Another thermally-driven model was put forth by Gu and Antropov[51], this time linking the transition to the excitation of magnons. The magnon DOS in the FM state is much larger than that of the AFM state. Therefore, as temperature is increased, there is a much larger gain in free energy from magnon excitations in the FM state. However, the magnitude of this difference is highly affected by the coupling between Fe and Rh moments. They note that the gain in free energy of the FM state is significantly reduced without
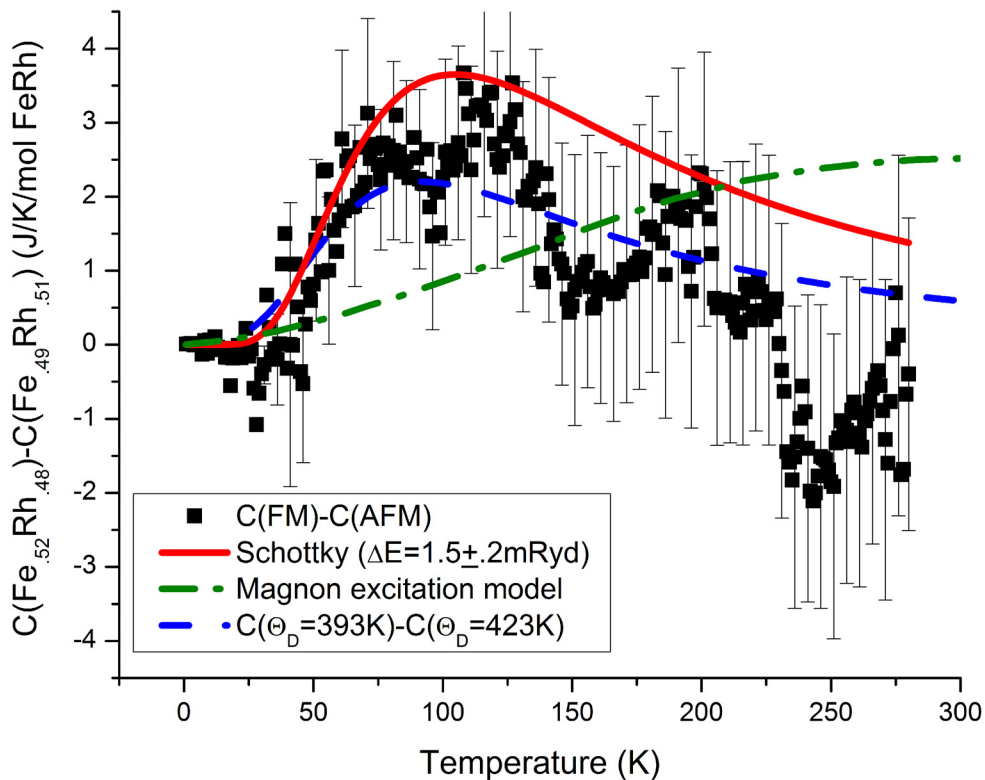
Figure 6.4: Difference in specific heat data between $Fe_{.52}Rh_{.48}$ and $Fe_{.49}Rh_{.51}$. The data is fit a Schottky two-state anomaly, resulting in an energy splitting of $1.5 \pm .2$mRyd (solid red line). The excess heat capacity predicted by Gu and Antropov's magnon fluctuation model[51] is shown for reference (green dashed-dotted line). The data has also been fit as a subtraction between two Debye models, one with the fixed value measured for the FM at low temperature, 393K, and the other allowed to vary, yielding a best fit at $\Theta_D = 423 \pm 1$K (dashed blue line).

strong coupling between the Fe and Rh magnetic states - this is counter to the model by Gruner et al. where they treat the Fe and Rh moments independently. The resultant heat capacity of this magnon-driven model shows a peak difference between the two phases at about 300K (see Figure 6.4).

As noted in Section 6.3, we do observe a difference in heat capacity between the AFM and FM alloys. The difference between the two is plotted in Figure 6.4. Though the error bars are substantial, we observe a distinct peak in ΔC, albeit at a reduced temperature from either of the thermal fluctuation models. We can fit this to a Schottky model with a single fitting parameter, the energy splitting ΔE, which gives a value of 1.5 ± 0.2mRyd. In this fit, we take the multiplicity of the two states to be equal; either the Rh moment is zero, or it is aligned with the local Fe moments ($\uparrow$) - the anti-aligned state ($\downarrow$) has a much higher energy than either. In a crude version of Gruner's model, $\Delta E = 1.5 \pm .2$mRyd would correspond to the energy splitting for a Rh atom with 7 $\uparrow$ and 1 $\downarrow$ Fe neighbors ($2.1 \times (7-1) - 11.1 = 1.5$). However, at a temperature so far below the Curie temperature of the FM phase ($T_C \approx 600$K), this is an extremely unlikely state and far too naïve a picture, most likely simply coincidental. The observed peak is rather far from $T_{AF>FM}$, so it does not appear to be consistent with the magnon-driven fluctuation model where the maximum ΔC is observed at ~ 300K (Figure 6.4), but the error bars are large enough that it is difficult to say anything too conclusive.

As an illustration of how small the observed anomaly is and how careful one must be to analyze the data, Figure 6.4 depicts a model of the difference in heat capacity if it were to entirely come from a difference in the phonons between the FM and AFM phase. While the value of Θ_D for the AFM phase in this case would be within expectations of previous measurements, this model necessitates a much stiffer lattice in the AFM phase than observed in the low-temperature specific heat (423 ± 1K v. 340 ± 13K). It is possible for the short-range phonon modes to be preserved in these films and thus the lattice contribution to the heat capacity at high temperatures to more closely match that of the bulk, but we see no a priori reason to suggest that there is such a significant difference at room temperature between the two films. Consequently, we use the model here simply for illustrative purposes only. In order to eliminate any differences in lattice entropy, one would ideally have inelastic neutron scattering measurements, but short of that it is not clear how to eliminate any subtle differences. In our analysis, we make the assumption that there is no difference at high temperature between the two based upon the close agreement with AFM and FM alloys previously.

As a further check on the results, one can calculate the entropy difference between the two phases and compare with that measured previously at the transition. Because above $T_{AF>FM}$ we expect the ferromagnetic phases to be identical, by integrating $\Delta C/T$ from 0K to $T_{AF>FM}$ we should obtain the same change in entropy, ΔS, as that measured through the AF>FM transition on a single film. The integration of $\Delta C/T$ yields 17 ± 3 J/kg/K, within the range of 12.6-18.3 J/kg/K measured previously[6, 65, 99, 100].

6.5 Conclusions

We showed via magnetization and X-ray diffraction measurements that $Fe_{.49}Rh_{.51}$ films grown on IBAD MgO show a reduced transition temperature compared to those grown on MgO. We also observed a sharper transition in the films grown on IBAD MgO and plan further studies to examine at the microscopic level domain nucleation in the AFM and FM phases as a function of strain.

Photoemission measurements above and below $T_{AF>FM}$ show a change in the valence band structure. However, our estimate of no more than a 10% change in $N(\epsilon_F)$ is far short of the fourfold increase proposed by Tu et al. to explain the Fe-Rh AF>FM transition with ground state electronic entropy differences.

We observed a Schottky anomaly in specific heat measurements of ferromagnetic $Fe_{.52}Rh_{.48}$ and antiferromagnetic $Fe_{.49}Rh_{.51}$ thin films corresponding to an energy splitting of 1.5 ± 0.2mRyd. Though the feature is consistent with magnetic fluctuations of the Rh moment, the peak is at a lower temperature, hence lower energy splitting, than theoretically predicted. We obtained an entropy difference $\Delta S_{FM-AFM} = 17 \pm 3$ J/kg/K, consistent with literature values.

Chapter 7

Conclusions

Microcalorimetry provides a platform for measuring thermodynamics of metastable materials and thin films, yielding information about the energetics of these novel systems. The development of small sample calorimetry allowed for the direct measurement of the entropic difference in γ-Fe$_2$SiO$_4$ compared to α-Fe$_2$SiO$_4$ by integrating $C(T)/T$, yielding -16 ± 5 J/mol/K, confirming the previous indirect calculation and helping to shed light on the phase diagram of a key component of the earth's mantle. Following this, we turned our eyes to the Fe/Cr multilayer system that fueled the data revolution of the mid-1990's, first by showing how disorder plays a dominant role in the density of states of chromium and later by learning that though we saw evidence of an interfacial enhancement in sputtered Fe/Cr MMLs, the spin-dependent scattering responsible for GMR is more strongly coupled to having a well-defined interface. Finally, we looked at the energetics of the AF>FM transition in Fe-Rh alloys, a material proposed for thermally assisted magnetic recording. We conclusively showed through specific heat measurements and complementary photoemission results above and below the transition that the model of the AF>FM transition based on the ground state electronic density of state difference in the two phases is incorrect. Furthermore, we measured a Schottky anomaly in the FM Fe$_{.52}$Rh$_{.48}$ alloy corresponding to an energy difference of 1.5 ± 0.2mRyd, consistent with a magnetic fluctuation model.

In order to measure the specific heat of the Fe-Rh alloys, we successfully developed a microcalorimeter centered around IBAD MgO capable of measuring the specific heat of epitaxial thin films. This opens up the door to a host of other thin film systems such as high-T_C superconductors, multiferroics, and dilute magnetic semiconductors where order is crucial and strain can be used to stabilize non-equilibrium films. Future work includes measurements of (Ga,Mn)As, further developing the IBAD MgO for use on our nanocalorimeters, density functional calculations on Fe-Rh binary and ternary alloys, and photoemission electron microscopic (PEEM) measurements on FeRh above and below the transition on different substrates to study domain nucleation.

Bibliography

[1] E. Noel Abarra. *Heat Capacity Measurements of Magnetic Thin Films*. Ph.D. thesis, University of California, San Diego, 1996.

[2] K. Allen and F. Hellman. Specific heat of C_{60} and K_3C_{60} thin films for $T = 1.5 - -400K$. *Physical Review B*, 60(16):11765–11772, 1999.

[3] K. Allen and F. Hellman. Specific heat of endohedral and higher fullerene thin films. *The Journal of Chemical Physics*, 111(12):5291–5294, 1999.

[4] L.H. Allen and S.L. Lai. MEMS-based scanning calorimeter for thermodynamic properties of nanostructures. *Microscale Thermophysical Engineering*, 2(1):11–19, 1998.

[5] Philip B. Allen. Empirical electron-phonon lambda values from resistivity of cubic metallic elements. *Physical Review B*, 36(5):2920 LP – 2923, 1987.

[6] M.P. Annaorazov, S.A. Nikitin, A.L. Tyurin, K.A. Asatryan, and A.Kh. Dovletov. Anomalously high entropy change in FeRh alloy. *Journal of Applied Physics*, 79(3):1689–1695, 1996.

[7] P.N. Arendt, S.R. Foltyn, L. Civale, R.F. DePaula, P.C. Dowden, J.R. Groves, T.G. Holesinger, Q.X. Jia, S. Kreiskott, L. Stan, I. Usov, H. Wang, and J.Y. Coulter. High critical current YBCO coated conductors based on IBAD MgO. *Physica C: Superconductivity Proceedings of the 16th International Symposium on Superconductivity (ISS 2003). Advances in Superconductivity XVI. Part II*, 412-414(Part 2):795–800, 2004.

[8] Paul N. Arendt and Stephen R. Foltyn. Biaxially textured IBAD-MgO templates for YBCO-coated conductors. *MRS Bulletin*, 29(8):543–550, 2004.

[9] R. Bachmann, Jr. F.J. DiSalvo, T.H. Geballe, R.L. Greene, R.E. Howard, C.N. King, H.C. Kirsch, K.N. Lee, R.E. Schwall, H.-U. Thomas, and R.B. Zubeck. Heat capacity measurements on small samples at low temperatures. *Review of Scientific Instruments*, 43(2):205–214, 1972.

[10] T.H.K. Barron, W.T. Berg, and J.A. Morrison. On the heat capacity of crystalline magnesium oxide. *Proceedings of the Royal Society of London. Series A. Mathematical and Physical Sciences*, 250(1260):70–83, 1959.

[11] M.M. Beg. Debye temperature of MgO powder by elastic neutron scattering. *Acta Crystallographica Section A*, 32(1):154–156, 1976.

[12] Z. Boekelheide, David W. Cooke, and F. Hellman. Anomalous electrical resistivity of polycrystalline Cr films. *Physical Review B*, 80:133426, 2009.

[13] Z. Boekelheide, E. Helgren, and F. Hellman. Spin-density wave in polycrystalline Cr films from infrared reflectivity. *Physical Review B*, 76(22):224429–8, 2007.

[14] J. Boerio-Goates, G. Li, L. Li, T.F. Walker, T. Parry, and B.F. Woodfield. Surface water and the origin of the positive excess specific heat for 7 nm rutile and anatase nanoparticles. *Nano Letters*, 6(4):750–754, 2006.

[15] S.D. Brorson, A. Kazeroonian, J.S. Moodera, D.W. Face, T.K. Cheng, E.P. Ippen, M.S. Dresselhaus, and G. Dresselhaus. Femtosecond room-temperature measurement of the electron-phonon coupling constant gamma in metallic superconductors. *Physical Review Letters*, 64(18):2172 LP – 2175, 1990.

[16] P. Bruno. Theory of interlayer magnetic coupling. *Physical Review B*, 52(1):411 LP – 439, 1995.

[17] Ching-Hao Chang and Tzay-Ming Hong. Interlayer coupling enhanced by the interface roughness: A perturbative method. *Physical Review B*, 79(5):054415, 2009.

[18] Liang-Yao Chen and David W. Lynch. Ellipsometric studies of magnetic phase transitions of Fe-Rh alloys. *Physical Review B*, 37(18):10503 LP – 10509, 1988.

[19] Y.Y. Chen, Y.D. Yao, S.S. Hsiao, S.U. Jen, B.T. Lin, H.M. Lin, and C.Y. Tung. Specific-heat study of nanocrystalline palladium. *Physical Review B*, 52(13):9364 LP – 9369, 1995.

[20] C.H. Cheng, C.T Wei, and P.A. Beck. Low-temperature specific heat of body-centered cubic alloys of 3d transition elements. *Physical Review*, 120(2):426–436, 1960.

[21] M.M. Collver and R.H. Hammond. Superconductivity in "amorphous" transition-metal alloy films. *Physical Review Letters*, 30(3):92 LP – 95, 1973.

[22] David W. Cooke, Z. Boekelheide, D.R. Queen, and F. Hellman. The role of the spin-density wave and disorder in the density of states of sputtered Cr films. *Journal of Applied Physics*, Volume 105, pages 07C314–3, Austin, Texas (USA), 2009. AIP.

[23] David W. Cooke, J.R. Groves, Frances H. Hellman, and B.M. Clemens. Specific heat of epitaxial thin films. *Review of Scientific Instruments*, In preparation, 2010.

[24] David W. Cooke, K.J. Michel, and F. Hellman. Thermodynamic measurements of submilligram bulk samples using a membrane-based "calorimeter on a chip". *Review of Scientific Instruments*, 79(5):053902–10, 2008.

[25] David W. Cooke, D.R. Queen, and F. Hellman. Enhanced density of states in Fe/Cr multi-layers. *Journal of Magnetism and Magnetic Materials*, In Preparation.

[26] J.E. Crow, M. Strongin, R.S. Thompson, and O.F. Kammerer. The superconducting transition temperatures of disordered Nb, W, and Mo films. *Physics Letters A*, 30(3):161–162, 1969.

[27] M.C. Cyrille, S. Kim, M.E. Gómez, J. Santamaria, C. Leighton, K.M. Krishnan, and I.K. Schuller. Effect of sputtering pressure-induced roughness on the microstructure and the perpendicular giant magnetoresistance of Fe/Cr superlattices. *Physical Review B*, 62(22):15079 LP – 15083, 2000.

[28] A.LeR. Dawson and D.H. Ryan. Heat capacity of silver paint. *Review of Scientific Instruments*, 67(7):2648–2649, 1996.

[29] S.O. Demokritov, C. Bayer, S. Poppe, M. Rickart, J. Fassbender, B. Hillebrands, D.I. Kholin, N.M. Kreines, and O.M. Liedke. Control of interlayer exchange coupling in Fe/Cr/Fe trilayers by ion beam irradiation. *Physical Review Letters*, 90(9):097201, 2003.

[30] D.W. Denlinger, E.N. Abarra, K. Allen, P.W. Rooney, M.T. Messer, S.K. Watson, and F. Hellman. Thin film microcalorimeter for heat capacity measurements from 1.5 to 800 k. *Review of Scientific Instruments*, 65(4):946–959, 1994.

[31] S.G. Doettinger-Zech, M. Uhl, D.L. Sisson, and A. Kapitulnik. Simple microcalorimeter for measuring microgram samples at low temperatures. *Review of Scientific Instruments*, 72(5):2398–2406, 2001.

[32] R.C. Dynes. McMillan's equation and the T_C of superconductors. *Solid State Communications*, 10(7):615–618, 1972.

[33] R.C. Dynes and C.M. Varma. Superconductivity and electronic density of states. *Journal of Physics F: Metal Physics*, 6(7):L215–L219, 1976.

[34] Stephen Radford Early. *Small Sample Calorimetry at Low Temperatures*. Ph.D. thesis, Stanford University, 1981.

[35] R.S. Eccleston, M. Hagen, Ll. Manosa, G.A. Saunders, and H.L. Alberts. Calorimetric and neutron diffraction studies of the commensurate - incommensurate spin-density-wave phase transition of Cr+0.3 at.% Ru alloy. *Journal of Physics: Condensed Matter*, 8(42):7837–7846, 1996.

[36] Eric Fawcett. Spin-density-wave antiferromagnetism in chromium. *Reviews of Modern Physics*, 60(1):209 LP – 283, 1988.

[37] J.L. Feldman. Lattice-vibrational properties of chromium in the harmonic approximation on the basis of the tensor model. *Physical Review B*, 1(2):448–454, 1970.

[38] B. Fogarassy, T. Kemény, L. Pál, and J. Tóth. Electronic specific heat of iron-rhodium and iron-rhodium-iridium alloys. *Physical Review Letters*, 29(5):288 LP – 291, 1972.

[39] F. Fominaya, J. Villain, P. Gandit, J. Chaussy, and A. Caneschi. Heat capacity anomalies induced by magnetization quantum tunneling in a $Mn_{12}O_{12}$-acetate single crystal. *Physical Review Letters*, 79(6):1126–1129, 1997.

[40] E.E. Fullerton, S.D. Bader, and J.L. Robertson. Spin-density-wave antiferromagnetism of Cr in Fe/Cr(001) superlattices. *Physical Review Letters*, 77(7):1382 LP – 1385, 1996.

[41] E.E. Fullerton, M.J. Conover, J.E. Mattson, C.H. Sowers, and S.D. Bader. Oscillatory interlayer coupling and giant magnetoresistance in epitaxial Fe/Cr(211) and (100) superlattices. *Physical Review B*, 48(21):15755 LP – 15763, 1993.

[42] E.E. Fullerton, D.M. Kelly, J. Guimpel, I.K. Schuller, and Y. Bruynseraede. Roughness and giant magnetoresistance in Fe/Cr superlattices. *Physical Review Letters*, 68(6):859 LP – 862, 1992.

[43] J.-L. Garden, H. Guillou, A.F. Lopeandia, J. Richard, J.-S. Heron, G.M. Souche, F.R. Ong, B. Vianay, and O. Bourgeois. Thermodynamics of small systems by nanocalorimetry: From physical to biological nano-objects. *Thermochimica Acta*, 492(1-2):16–28, 2009.

[44] M.E. Gómez, J. Santamaria, S. Kim, K.M. Krishnan, and I.K. Schuller. Detailed structural analysis of epitaxial MBE-grown Fe/Cr superlattices by X-ray diffraction and transmission-electron spectroscopy. *Physical Review B*, 71(12):125410, 2005.

[45] J.F. Goff. Multiband model for the electronic heat capacity of chromium. *Physical Review B*, 4(4):1121 LP – 1128, 1971.

[46] S. Yu. Grachev, F.D. Tichelaar, and G.C.A.M. Janssen. Stress in sputter-deposited Cr films: Influence of Ar pressure. *Journal of Applied Physics*, 97(7):073508–4, 2005.

[47] G. Grimvall. The electron-phonon interaction in normal metals. *Physica Scripta*, 14(1-2):63–78, 1976.

[48] J.R. Groves, P.N. Arendt, T.G. Holesinger, R.F. DePaula, L. Stan, I.O. Usov, and R.H. Hammond. Dual ion assist beam processing of magnesium oxide template layers for 2nd generation coated conductors. *IEEE Transactions on Applied Superconductivity*, 17(2):3402–3405, 2007.

[49] P. Grünberg, R. Schreiber, Y. Pang, M.B. Brodsky, and H. Sowers. Layered magnetic structures: Evidence for antiferromagnetic coupling of Fe layers across Cr interlayers. *Physical Review Letters*, 57(19):2442 LP – 2445, 1986.

[50] M.E. Gruner, E. Hoffmann, and P. Entel. Instability of the rhodium magnetic moment as the origin of the metamagnetic phase transition in α-FeRh. *Physical Review B*, 67(6):064415, 2003.

[51] R.Y. Gu and V.P. Antropov. Dominance of the spin-wave contribution to the magnetic phase transition in FeRh. *Physical Review B*, 72(1):012403, 2005.

[52] F. Heiniger, E. Bucher, and J. Muller. Low temperature specific heat of transition metals and alloys. *Phys. kondens. Materie*, 5:243–184, 1966.

[53] H. Huth, A.A. Minakov, and C. Schick. Differential AC-chip calorimeter for glass transition measurements in ultrathin films. *Journal of Polymer Science Part B: Polymer Physics*, 44(20):2996–3005, 2006.

[54] Z. Jia, J.W. Harrell, and R.D.K. Misra. Synthesis and magnetic properties of self-assembled FeRh nanoparticles. *Applied Physics Letters*, 93(2):022504–3, 2008.

[55] N.M. Jisrawi, M.W. Ruckman, T.R. Thurston, G. Reisfeld, M. Weinert, M. Strongin, and M. Gurvitch. Reversible depression in the T_C of thin Nb films due to enhanced hydrogen adsorption. *Physical Review B*, 58(10):6585 LP – 6590, 1998.

[56] W.L. Johnson, S.J. Poon, J. Durand, and P. Duwez. Superconductivity, magnetic susceptibility, and electronic properties of amorphous $(Mo_{1-x}Ru_x)_{80}P20$ alloys obtained by liquid quenching. *Physical Review B*, 18(1):206 LP – 217, 1978.

[57] J.F. Jurado, E. Ortiz, and R.A. Vargas. An AC calorimeter probe for a closed-cycle cryogenic station. *Measurement Science and Technology*, 8(10):1151–1155, 1997.

[58] R. Karmouch, J.-F. Mercure, and F. Schiettekatte. Nanocalorimeter fabrication procedure and data analysis for investigations on implantation damage annealing. *Thermochimica Acta*, 432(2):186–191, 2005.

[59] G. Kastle, T. Muller, H.-G. Boyen, A. Klimmer, and P. Ziemann. Resistivity and phonon softening in ion-irradiated epitaxial gold films. *Journal of Applied Physics*, 96(12):7272–7277, 2004.

[60] R.K. Kawakami, E. Rotenberg, E.J. Escorcia-Aparicio, H.J. Choi, J.H. Wolfe, N.V. Smith, and Z.Q. Qiu. Determination of the magnetic coupling in the Co/Cu/Co(100) system with momentum-resolved quantum well states. *Physical Review Letters*, 82(20):4098 LP – 4101, 1999.

[61] D. Kim, B. Revaz, B.L. Zink, F. Hellman, J.J. Rhyne, and J.F. Mitchell. Tricritical point and the doping dependence of the order of the ferromagnetic phase transition of $La_{1-x}Ca_xMnO_3$. *Physical Review Letters*, 89(22):227202, 2002.

[62] C. Kittel. Model of exchange-inversion magnetization. *Physical Review*, 120(2):335 LP – 342, 1960.

[63] Hnin Yu Yu Ko, Takao Suzuki, Nguyen N. Phuoc, and Jiangwei Cao. Fabrication and characterization of FeRh nanoparticles. *Journal of Applied Physics*, 103(7):07D508–3, 2008.

[64] C. Koenig. Self-consistent band structure of paramagnetic, ferromagnetic and antiferromagnetic ordered FeRh. *Journal of Physics F: Metal Physics*, 12(6):1123, 1982.

[65] J.S. Kouvel. Unusual nature of the abrupt magnetic transition in FeRh and its pseudobinary variants. *Journal of Applied Physics*, 37(3):1257–1258, 1966.

[66] K. Kreiner, H. Michor, G. Hilscher, N.V. Baranov, and S.V. Zemlyanski. Evolution of the electronic specific heat and magnetic order in $(Fe_{1-x}Ni_x)$rh. *Journal of Magnetism and Magnetic Materials*, 177-181(Part 1):581–582, 1998.

[67] M.M. Kreitman, T. Ashworth, and M. Rechowicz. A correlation between thermal conductance and specific heat anomalies and the glass temperature of Apiezon N and T greases. *Cryogenics*, 12(1):32–34, 1972.

[68] O. Krupin, Eli Rotenberg, and S.D. Kevan. Controlling the magnetic ground state in $Cr_{1-x}V_x$ films. *Physical Review Letters*, 99(14):147208–4, 2007.

[69] A.T. Kwan, M. Yu. Efremov, E.A. Olson, F. Schiettekatte, M. Zhang, P.H. Geil, and L.H. Allen. Nanoscale calorimetry of isolated polyethylene single crystals. *Journal of Polymer Science Part B: Polymer Physics*, 39(11):1237–1245, 2001.

[70] J.C. Lashley. Personal communication, 2001.

[71] J.C. Lashley, M.F. Hundley, A. Migliori, J.L. Sarrao, P.G. Pagliuso, T.W. Darling, M. Jaime, J.C. Cooley, W.L. Hults, and L. Morales. Critical examination of heat capacity measurements made on a quantum design physical property measurement system. *Cryogenics*, 43(6):369–378, 2003.

[72] D.G. Laurent, J. Callaway, J.L. Fry, and N.E. Brener. Band structure, fermi surface, compton profile, and optical conductivity of paramagnetic chromium. *Physical Review B*, 23(10):4977 LP – 4987, 1981.

[73] M. Yu. Lavrentiev, R. Drautz, D. Nguyen-Manh, T.P.C. Klaver, and S.L. Dudarev. Monte carlo study of thermodynamic properties and clustering in the bcc Fe-Cr system. *Physical Review B*, 75(1):014208, 2007.

[74] J.-S. Lee, E. Vescovo, L. Plucinski, C.M. Schneider, and C.-C. Kao. Electronic structure and magnetic properties of epitaxial FeRh(001) ultrathin films on W(100). *Physical Review B*, 82(22):224410, 2010.

[75] A.F. Lopeanda, L.l. Cerd, M.T. Clavaguera-Mora, Leonel R. Arana, K.F. Jensen, F.J. Muoz, and J. Rodrguez-Viejo. Sensitive power compensated scanning calorimeter for analysis of phase transformations in small samples. *Review of Scientific Instruments*, 76(6):065104–5, 2005.

[76] Rolf Lortz, Satoko Abe, Yuxing Wang, Frederic Bouquet, Ulrich Tutsch, and Alain Junod. Modulated-bath AC calorimetry using modified commercial peltier elements. *Review of Scientific Instruments*, 76(10):103902–8, 2005.

[77] Victor F. Los and Andrei V. Los. Theory of interlayer magnetic coupling in nanostructures with disordered interfaces. *Physical Review B*, 77(2):024410, 2008.

[78] S. Maat, J.-U. Thiele, and E.E. Fullerton. Temperature and field hysteresis of the antiferromagnetic-to-ferromagnetic phase transition in epitaxial FeRh films. *Physical Review B*, 72(21):214432, 2005.

[79] V. Matias, M. Hoek, J. Hanisch, and A.T. Findikoglu. Texture evolution in ion-beam-assist deposited MgO. *Material Research Society Symposium Proceedings*, 1150:RR04–03, 2009.

[80] W.L. McMillan. Transition temperature of strong-coupled superconductors. *Physical Review*, 167(2):331 LP – 344, 1968.

[81] D.B. McWhan and T.M. Rice. Pressure dependence of itinerant antiferromagnetism in chromium. *Physical Review Letters*, 19(15):846 LP – 849, 1967.

[82] A.A. Minakov, S.B. Roy, Y.V. Bugoslavsky, and L.F. Cohen. Thin-film alternating current nanocalorimeter for low temperatures and high magnetic fields. *Review of Scientific Instruments*, 76(4):043906–9, 2005.

[83] R. Mélin and F. Fominaya. A theoretical investigation of the specific heat of superlattices in a magnetic field. *Journal of Magnetism and Magnetic Materials*, 172(1-2):97–109, 1997.

[84] S. Moyerman. Personal communication, 2009.

[85] K. Nakada and H. Yamada. Fermi surface and antiferromagnetism of FeRh. *Journal of Magnetism and Magnetic Materials*, 310:1046–1047, 2007.

[86] Alexandra Navrotsky. High pressure transitions in silicates. *Progress in Solid State Chemistry*, 17(2):53–86, 1987.

[87] Alexandra Navrotsky. Progress and new directions in high temperature calorimetry revisited. *Physics and Chemistry of Minerals*, 24(3):222–241, 1997.

[88] Alexandra Navrotsky, Maria Dorogova, Frances Hellman, David W. Cooke, Barry L. Zink, Charles E. Lesher, Juliana Boerio-Goates, Brian F. Woodfield, and Brian Lang. High-pressure geoscience special feature: Application of calorimetry on a chip to high-pressure materials. *Proc. Nat. Acad. Sci.*, 104(22):9187–9191, 2007.

[89] A.W. Overhauser. Spin density waves in an electron gas. *Physical Review*, 128(3):1437 LP – 1452, 1962.

[90] S.B. Palmer, P. Dentschuk, and D. Melville. Elastic properties of an iron-rhodium alloy. *Physica Status Solidi (A)*, 32(2):503–508, 1975.

[91] J.S. Parker, L. Wang, K.A. Steiner, P.A. Crowell, and C. Leighton. Exchange bias as a probe of the incommensurate spin-density wave in epitaxial Fe/Cr(001). *Physical Review Letters*, 97(22):227206–4, 2006.

[92] D.T. Pierce, J. Unguris, R.J. Celotta, and M.D. Stiles. Effect of roughness, frustration, and antiferromagnetic order on magnetic coupling of fe/Cr multilayers. *Journal of Magnetism and Magnetic Materials*, 200(1-3):290–321, 1999.

[93] D.R. Queen. Preliminary analysis of substrate and membrane roughness. *Unpublished*, 2006.

[94] D.R. Queen and F. Hellman. Thin film nanocalorimeter for heat capacity measurements of 30 nm films. *Review of Scientific Instruments*, 80(6):063901–7, 2009.

[95] N.M. Rensing, A.P. Payne, and B.M. Clemens. The effect of roughness on the magnetoresistance of Fe/Cr multilayers. *Journal of Magnetism and Magnetic Materials Proceedings of the International Symposium on Magnetic Ultrathin Films, Multilayers and Surfaces*, 121(1-3):436–439, 1993.

[96] N.M. Rensing, A.P. Payne, and B.M. Clemens. The effect of roughness on the magnetoresistance of Fe/Cr multilayers. *Journal of Magnetism and Magnetic Materials*, 121(1-3):436–439, 1993.

[97] B. Revaz, M.-C. Cyrille, B.L. Zink, I.K. Schuller, and F. Hellman. Enhancement of the electronic contribution to the low-temperature specific heat of an Fe/Cr magnetic multilayer. *Physical Review B*, 65(9):094417, 2002.

[98] B. Revaz, B.L. Zink, D. O'Neil, L. Hull, and F. Hellman. Numerical simulation of the heat transfer in amorphous silicon nitride membrane-based microcalorimeters. *Review of Scientific Instruments*, 74(10):4389–4403, 2003.

[99] M.J. Richardson, D. Melville, and J.A. Ricodeau. Specific heat measurements on an Fe-Rh alloy. *Physics Letters A*, 46(2):153–154, 1973.

[100] J. A. Ricodeau and D. Melville. Model of the antiferromagnetic-ferromagnetic transition in FeRh alloys. *Journal of Physics F: Metal Physics*, 2(2):337, 1972.

[101] O. Riou, P. Gandit, M. Charalambous, and J. Chaussy. A very sensitive microcalorimetry technique for measuring specific heat of μg single crystals. *Review of Scientific Instruments*, 68(3):1501–1509, 1997.

[102] Richard A. Robie, Cabell B. Finch, and Bruce S. Hemingway. Heat capacity and entropy of fayalite (Fe_2SiO_4) between 5.1 and 383 k; comparison of calorimetric and equilibrium values for the QFM buffer reaction. *American Mineralogist*, 67(5-6):463–469, 1982.

[103] Eli Rotenberg, Oleg Krupin, and S Kevan. Surface states and spin density wave periodicity in Cr(110) films. *New Journal of Physics*, 10(2):023003, 2008.

[104] W. Schnelle, J. Engelhardt, and E. Gmelin. Specific heat capacity of Apiezon N high vacuum grease and of duran borosilicate glass. *Cryogenics*, 39(3):271–275, 1999.

[105] John P. Shepherd. Analysis of the lumped τ_2 effect in relaxation calorimetry. *Review of Scientific Instruments*, 56(2):273–277, 1985.

[106] G. Shirane, R. Nathans, and C. W. Chen. Magnetic moments and unpaired spin densities in the Fe-Rh alloys. *Physical Review*, 134(6A):A1547 LP – A1553, 1964.

[107] G.R. Stewart. Measurement of low-temperature specific heat. *Review of Scientific Instruments*, 54(1):1–11, 1983.

[108] M.D. Stiles. Exchange coupling in magnetic heterostructures. *Physical Review B*, 48(10):7238 – 7258, 1993.

[109] K. Suito, Y. Tsutsui, S. Nasu, A. Onodera, and F.E. Fujita. Moessbauer effect study of the gamma-form of fe_2sio_4. In *Materials Research Society Symposia Proceedings*, volume 22, pages 295–298, 1984.

[110] J.-U. Thiele, S. Maat, and E.E. Fullerton. FeRh/FePt exchange spring films for thermally assisted magnetic recording media. *Applied Physics Letters*, 82(17):2859–2861, 2003.

[111] Y.S. Touloukian. *Specific Heat: Metallic Elements and Alloys*, Volume 4 of *Thermophysical Properties of Matter*. 1970.

[112] P. Tu, A.J. Heeger, J.S. Kouvel, and J.B. Comly. Mechanism for the first-order magnetic transition in the FeRh system. *Journal of Applied Physics*, 40(3):1368–1369, 1969.

[113] R. van den Berg, H. von Lohneysen, and H.J. Schink. Calorimetric investigation of a-Si and a-Ge in high magnetic fields. *Journal of Non-Crystalline Solids*, 77-78(2):1339–42, 1985.

[114] M. Velez and I.K. Schuller. Sputtering pressure effect on the giant magnetoresistance of Fe/Cr superlattices. *Journal of Magnetism and Magnetic Materials*, 184(3):275–280, 1998.

[115] Y. Wang, P.M. Levy, and J.L. Fry. Interlayer magnetic coupling in Fe/Cr multilayered structures. *Physical Review Letters*, 65(21):2732 – 2735, 1990.

[116] Chun-Yeol You, C.H. Sowers, A. Inomata, J.S. Jiang, S.D. Bader, and D.D. Koelling. Oscillation period of the interlayer coupling for epitaxial $Fe/Cr_{1-x}V_x$(100) and (211) superlattices. *Journal of Applied Physics*, 85(8):5889–5891, 1999.

[117] P. Zahn, J. Binder, I. Mertig, R. Zeller, and P.H. Dederichs. Origin of giant magnetoresistance: Bulk or interface scattering. *Physical Review Letters*, 80(19):4309 LP – 4312, 1998.

[118] Shu Zhang, Y. Rabin, Yizhang Yang, and M. Asheghi. Nanoscale calorimetry using a suspended bridge configuration. *Journal of Microelectromechanical Systems*, 16(4):861–871, 2007.

[119] B.L. Zink and F. Hellman. Specific heat and thermal conductivity of low-stress amorphous SiN membranes. *Solid State Communications*, 129(3):199–204, 2004.